The Henryk Niewodniczański Institute of Nuclear Physics
Polish Academy of Sciences

$PtRhNi/SnO_2$ 3D catalyst for electrochemical oxidation of ethanol: synthesis and physicochemical characterization

Grzegorz Gruzeł

Thesis submitted for the Degree of Doctor of Philosophy in Physics
Prepared under the supervision of

dr hab. inż. **Magdalena Parlińska-Wojtan**

Kraków 2019

Acknowledgements

First of all, I would like to express my deepest gratitude to my thesis supervisor dr hab. inż. Magdalena Parlińska-Wojtan for leading me through all this years and teaching me everything I know about electron microscopy. I am also grateful for supporting me and my ideas and, especially, for giving me the freedom in making my own scientific decisions.

Special thanks also go to dr Andrzej Kowal who introduced me into nanotechnology and who proposed the idea, which is the basis of this thesis.

I would also like to thank to people who helped me in my research, especially dr hab. Mirosława Pawlyta, dr hab. Przemysław Piekarz, dr Alexey Maximenko, dr Andrzej Budziak, dr Magdalena Oćwieja, dr Anna Pajor-Świerzy, prof. dr hab. Mikołaj Donten, dr Sebastian Arabasz.

My deepest thanks to all my colleagues from the Division of Condensed Matter Physics (IFJ PAN) headed by Prof. Maria Massalska-Arodź and from the Department for Functional Nanomaterials, particularly Ela Drzymała, for support and good advices.

Special thanks to my family and all my friends for their cheering presence and unconditional support.

And finally, I would like to thank my wife Joanna, who always believes in me and inspires me. Everything is better with You.

Abstract

Direct ethanol fuel cells (DEFC) are considered as efficient, environmentally friendly sources of renewable energy. Unfortunately, the catalysts used at the DEFC anode are still not efficient enough, as they catalyze ethanol oxidation to by-products instead of the desired final product CO_2. Therefore, in the present study novel nanoframes-based catalysts for ethanol oxidation are proposed. The main aim of the study was to determine the physical processes leading to the formation of PtNi and PtRhNi hollow nanoframes-based catalysts. First, growth thermodynamics and growth kinetics of the solid PtNi and PtRhNi nanoparticle templates, precursors for the nanoframes, were studied. It was found that during the nanoparticles growth, diffusion of platinum and rhodium occurs from the nanoparticles core to their edges, resulting in the formation of phase-segregated $PtNi_3$ or PtRhNi nanoparticles. To understand the process of Pt and Rh surface segregation phenomena occurring during the growth of PtRhNi nanopolyhedra, DFT calculations were performed. This confirmed that the system with Pt and Rh atoms on the surface is more energetically favorable than the system with these atoms in the core. Next, two approaches to obtain hollow nanoframes-based catalysts were applied. In the first approach, hollow Pt_3Ni and PtRhNi nanoframes were obtained by acidic etching of the Ni from the solid templates. The etching process was described thermodynamically by calculation of the cohesive energy for Ni system and PtRhNi alloy. According to the calculations, lower energy is needed to remove nickel from the Ni-core of the PtRhNi nanoparticles than from the PtRhNi-edges, which is consistent with the microscopic observations. Subsequently, based on opposite zeta potential values and electrostatic interactions, it was possible to successfully assembly the Pt_3Ni and PtRhNi nanoframes with SnO_2 NPs to obtain SnO_2@nanoframes catalysts. In the second approach, the nanoframes-based catalysts were obtained by galvanic replacement reaction (GRR). During this process the Ni atoms from the solid $PtNi_3$ and PtRhNi nanoparticles were removed, and simultaneously the tin originating from $SnCl_4$ was deposited on the resulting nanoframes. It was experimentally proven that the GRR takes place by two mechanisms. In the first one, the exchange of nickel and tin happens simultaneously, while in the second mechanism, initially oxidation and dissolution of nickel occurs and is then followed by tin deposition. Finally, all the obtained nanoframes-based catalysts were electrochemically tested towards ethanol oxidation reaction. Based on the obtained results, it can be seen that all of them have several times better catalytic performance in EOR, compared to commercially used Pt nanoparticles.

Streszczenie

Ogniwa paliwowe zasilane etanolem (DEFC) są wydajnym i przyjaznym środowisku źródłem energii elektrycznej. Niestety, katalizatory anodowe stosowane w DEFC nie są wystarczająco wydajne, zamiast głównego produktu utleniania etanolu, jakim jest CO_2, wytwarzają głównie produkty uboczne. W niniejszej pracy, przedstawiono nowe, oparte na strukturze tzw. nanoramek, katalizatory do utleniania etanolu. Głównym celem badań było zbadanie procesów fizycznych prowadzących do wytworzenia pustych, bazujących na nanoramkach katalizatorów PtNi i PtRhNi. Najpierw zbadano termodynamikę i kinetykę wzrostu litych nanocząstek $PtNi_3$ i PtRhNi, które stanowiły prekursory dla nanoramek. Na podstawie obserwacji mikroskopowych stwierdzono, że podczas wzrostu nanocząstek następuje dyfuzja atomów Pt lub Pt i Rh z rdzenia nanocząstek do ich krawędzi, co skutkuje powstaniem nanocząstek $PtNi_3$ i PtRhNi z segregacją faz. W celu zrozumienia tego procesu wykonano obliczenia DFT, które potwierdziły że układ z atomami Pt i Rh na powierzchni jest korzystniejszy energetycznie niż układ z tymi atomami pod powierzchnią. Następnie, zastosowano dwa podejścia w celu otrzymania katalizatorów bazujących na nanoramkach. W pierwszym podejściu otrzymano puste nanoramki z litych nanocząstek $PtNi_3$ i PtRhNi poprzez wytrawienie niklu z ich rdzenia. Proces trawienia został opisany termodynamicznie poprzez obliczenie energii kohezji dla układu zawierającego wyłącznie atomy Ni i układu zawierającego stop PtRhNi. Zgodnie z obliczeniami, niższa energia jest potrzebna do usunięcia atomu Ni z rdzenia niklowego litej nanocząstki PtRhNi, niż z krawędzi składającej się ze stopu PtRhNi, co jest zgodne z obserwacjami mikroskopowymi. Następnie, w oparciu o przeciwne potencjały zeta i oddziaływania elektrostatyczne, dokonano połączenia nanoramek PtNi i PtRhNi z nanocząstakmi SnO_2. Drugie podejście polegało na otrzymaniu katalizatorów opartych na nanoramkach za pomocą reakcji wymiany galwanicznej (GRR). Podczas tego procesu atomy niklu z litych nanocząstek $PtNi_3$ i PtRhNi zostały usunięte, z równoczesną depozycją atomów Sn pochodzących z $SnCl_4$ na otrzymanych nanoramkach. Eksperymentalnie dowiedziono, że reakcja wymiany galwanicznej zachodzi z udziałem dwóch procesów. W pierwszym dochodzi do równoczesnego usunięcia niklu i depozycji cyny, natomiast w drugim najpierw zachodzi usunięcie atomów niklu, a dopiero potem następuje depozycja cyny. Wszystkie otrzymane nanokatalizatory bazujące na nanoramkach zostały przetestowane w reakcji utleniania etanolu, wykazując kilkukrotnie większą wydajność niż komercyjnie stosowane nanocząstki Pt.

Table of contents

List of abbreviations

BF – bright field

CA – chronoamperometry

CCD – charged coupled device

CV – cyclic voltammetry

DFT – density functional theory

ECSA – electrochemically active surface areas

EDS – energy-dispersive X-ray spectroscopy

EG – ethylene glycol

EOR – ethanol oxidation reaction

fcc – face centered cubic

FEG – field emission gun

GGA – generalized gradient approximations

GRR – galvanic replacement reaction

HAADF – high-angle annular dark-field

HR – high resolution

ICP-OES – inductively coupled plasma optical emission spectrometry

LDA – local-density approximations

NFs – nanoframes

NPs – nanoparticles

RHE – reversible hydrogen electrode

SAED – selected area electron diffraction

SHE – standard hydrogen electrode

SSA – specific surface area

(S)TEM – (scanning) transmission electron microscope

XRD – X-ray diffraction

Introduction and motivation

Due to the world increasing energy demand, it is necessary to look for new ways of generating electricity, which will be independent on fossil fuels, due to their limited occurrence on Earth. Moreover, large emission of greenhouse gases, forces to develop electricity generation methods, which will not pollute the atmosphere. Therefore fuel cells, which allow to convert chemical energy into electricity, have received growing attention [1]. Currently, the most popular fuels for fuel cells are hydrogen [2] and methanol [3]. However, hydrogen production is expensive and additionally it is flammable, making its transport and storage troublesome [4,5]. Methanol as a liquid fuel is free of these disadvantages. Nevertheless, due to toxicity and common technical problems, such as methanol crossover or slow reaction at the anode, methanol is also not an ideal fuel [6]. Because of these disadvantages, it is required to search for new types of fuels. One of the most promising fuel is ethanol, which is non-toxic, causes no problems with transportation and storage, and has a high energy density in comparison with methanol (6.1 kWh/kg for methanol versus 8.0 kWh/kg for ethanol). Moreover, it is a renewable fuel produced from biomass or even agricultural waste [7]. Furthermore, it is potentially a carbon-neutral renewable, as the CO_2 released by use of the fuel cell can be re-absorbed by the crops used as an ethanol source in a closed cycle [8]. Therefore, the direct ethanol fuel cells (DEFC) are very promising sources of electric energy.

Direct ethanol fuel cells consist of an anode and a cathode, which are separated by an electrolyte. The working principle of DEFC is as follows. A mixture of ethanol and water is supplied to the anode, where due to the presence of catalytic nanoparticles, the ethanol oxidation reaction (EOR) takes place. During this reaction, protons, electrons and ideally CO_2 are generated. The protons pass through the membrane to the cathode, where they react with oxygen from air to produce water. At the same time, the electrons flow through an electrical circuit. In the ideal case ethanol is completely oxidized to CO_2, yielding 12 electrons. This course of reaction provides the maximum efficiency of energy conversion [9–11]. In this ideal case reactions occurring at the electrodes are as follows:

Anode: $C_2H_5OH + 3H_2O \rightarrow 12H^+ + 12e^- + 2CO_2$ (1)

Cathode: $3O_2 + 12H^+ + 12e^- \rightarrow 6H_2O$ (2)

Overall reaction: $C_2H_5OH + 3O_2 \rightarrow 3H_2O + 2CO_2$ (3)

Despite their advantages, DEFC are not yet commercialized, because of some technical difficulties mainly with catalysts used in reactions that occur in devices. Firstly,

due to the high price of platinum, which is used as a catalyst for both the anode and the cathode, the cost of DEFC production is too high [12]. Secondly, the currently used catalysts have low selectivity for the complete oxidation of ethanol to CO_2, which results in low efficiency of conversion of chemical energy to electrical energy [13]. Thirdly, due to the low selectivity of the ethanol oxidation reaction, by-products like acetic acid and acetaldehyde are formed [14]. These compounds can cause poisoning of the anode catalyst, which reduces its catalytic activity. These problems were attempted to be solved by improving the currently used catalysts by adding to platinum a second metallic element or combining it with oxide nanoparticles such as SnO_x. A major breakthrough in designing catalysts for ethanol oxidation was made in 2009 by Kowal *et al.* [15]. They obtained highly effective, ternary nanocatalysts, by deposition of Pt and Rh atoms on the SnO_2 nanoparticles. In the proposed catalytic systems, on the Pt sites dehydrogenation of ethanol occurs, Rh is responsible for the C-C bond breaking, while SnO_2 provides OH species to oxidize CO resulting from dehydrogenation of ethanol on platinum and breaking of C-C bonds on rhodium sites. In 2010 the same group improved these nanocatalysts, by deposition of small PtRh nanoparticles on larger SnO_2 nanoparticles and adjusting the Pt:Rh:Sn atomic ratio [16], to obtain consequently one of the most efficient nanocatalysts for EOR to this day.

On the other hand, in 2014 Stamenkovic *et al.* [17] proposed new catalysts for oxygen reduction reaction (ORR), which takes place at the cathode of fuel cell. First, they synthesized solid rhombic dodecahedral $PtNi_3$ nanoparticles with Ni-core and PtNi edges. Then, by etching the Ni atoms from the center of the nanoparticles they obtained so-called nanoframes with hollow interior. These catalysts show a 36 and 22-fold enhancement in mass and specific activities in ORR versus commercially used Pt catalysts. The higher catalytic performance of the nanoframes can be explained by their hollow structure, which enables access of reactants (in this case oxygen) to both the internal and external surfaces. Moreover, nanoframes provide a large number of edges and corners and high index crystallographic planes on the nanoparticle surface, which are the most catalytically active sites.

Herein, by combining these two approaches, i.e. using the appropriate chemical composition and designing catalysts with hollow, nanoframes-based morphology, novel nanocatalysts for EOR are proposed. Due to the fact, that this is the first attempt of obtaining such hollow, nanoframes-based catalysts for EOR, the physical fundamentals of nanoframes fabrication is highlighted in order to understand and, in future, optimize their synthesis procedure.

In brief, Chapter 1 gives a general introduction to direct ethanol fuel cells, as well as to the synthesis and catalytic application of the nanoframes. At the end of chapter the aim and the theses of the study are presented. Chapter 2 describes the physical fundamentals of the experimental methods and measuring procedures. Chapter 3 presents the results of the study with the discussion. This chapter is divided into four main subsections describing the physical aspects of: i) obtaining solid rhombic dodecahedral nanoparticles with phase segregation; ii) their transformation into nanoframes and deposition of SnO_2 nanoparticles (NPs) onto their surfaces; iii) conversion of solid, phase segregated, rhombic dodecahedral nanoparticles into nanoframes covered by SnO_2 layer by galvanic replacement reaction; iv) electrochemical tests of all the obtained nanocatalysts. Chapter 4 summarizes the performed studies and presents the conclusions.

Chapter 1: Fundamentals and state of the art

1.1. Introduction to direct ethanol fuel cells

1.1.1. Working principles of the direct ethanol fuel cell

The direct ethanol fuel cell contains three main elements (Figure 1): the anode, the cathode and electrolyte, which is an ionic conductor such as a proton exchange membrane. On the anode (negative electrode) and the cathode (positive electrode) of the DEFC, catalysts are deposited, which are nowadays, in most cases, Pt-based nanoparticles. Electrons originating from oxidized ethanol molecules are transferred from the anode, through an external circuit, to the cathode, where they reduce the oxygen from air. Simultaneously, the protons resulting from ethanol oxidation on the anode are transferred to the cathode, but unlike electrons, they pass through a membrane and not through an external circuit. Both, the electrons and the protons, recombine with oxygen forming water [9–11].

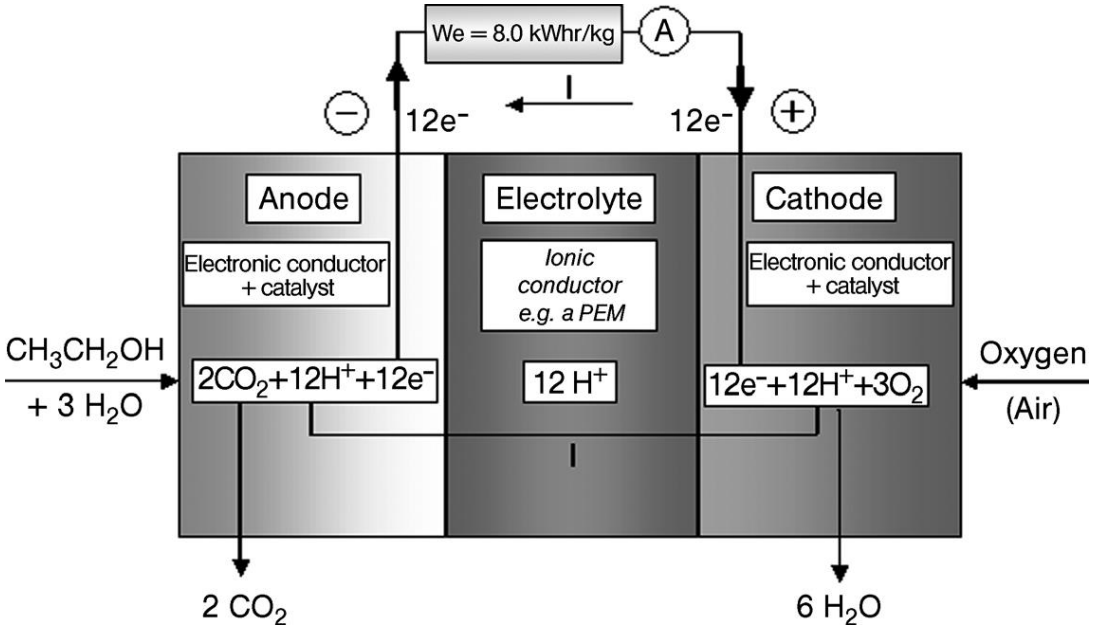

Figure 1. Schematic diagram of DEFC. Reprinted with permission from [9]. Copyright (2009) Wiley.

The total oxidation of ethanol at the anode (equation 1) results in generating two CO_2 molecules and 12 electrons [18]. However, in most cases, instead to CO_2, ethanol is oxidized to acetaldehyde (CH_3CHO) or acetic acid (CH_3COOH) (Figure 2), due to difficulties with the activation of the C-C bond in the ethanol molecule. This course of reaction with the

generation of 2 or 4 electrons for acetaldehyde and acetic acid, respectively, does not ensure a maximum efficiency in terms of electricity generation. Moreover, the acetaldehyde and acetic acid poison the surface of the platinum catalysts by being adsorbed on its surface [12]. This prevents further ethanol adsorption and decreases the efficiency of the ethanol oxidation reaction. However, the use of suitable catalysts can minimalize the effect of poisoning by increasing the selectivity of EOR towards CO_2, instead of acetaldehyde or acetic acid.

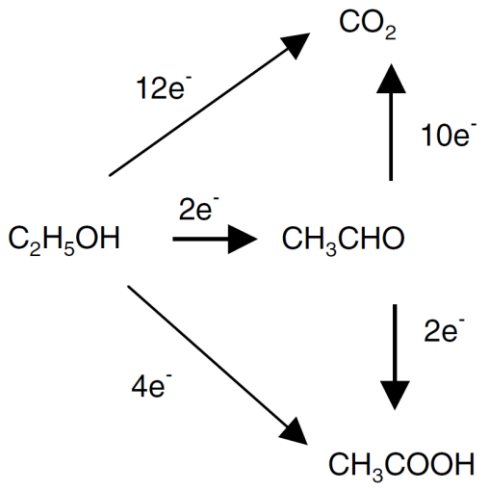

Figure 2. Schematic representation of the parallel pathways for ethanol oxidation. Reprinted with permission from [18]. Copyright (2005) Elsevier.

1.1.2. Currently used catalysts for ethanol oxidation reaction

Nowadays, the anodic catalysts used in DEFC for ethanol oxidation consist of nanoparticles: in acetic DEFC these are typically Pt-based, while in alkaline DEFC these catalysts are based on Pd [11]. However, this thesis deals with catalysts for EOR in acidic DEFC, therefore the catalysts for alkaline DEFC will not be discussed further. Because the EOR is a surface process, the catalysts need to have the highest possible surface area, therefore the catalytic nanoparticles are deposited on a carbon-support material to achieve better dispersion. In the first operating models of DEFC, pure platinum nanoparticles were used as catalysts. However due to Pt susceptibility to poisoning and its low catalytic performance towards complete oxidation of ethanol, scientists investigate the possibility of mixing it with other metals [14]. The next generation of the EOR catalysts were binary Pt-based nanoparticles. Typically, platinum nanoparticles were alloyed with tin (PtSn nanoparticles) or with ruthenium (PtRu nanoparticles). The addition of tin improves the catalytic performance of the catalysts, because Sn can enhance the oxidation of the by-products of ethanol oxidation on Pt surface by promoting H_2O dissociation. Also, tin weakens

the Pt by-products bonding, which facilitates the removal of the by-products from Pt surface and prevents the poisoning [19,20]. The addition of ruthenium also affects the catalytic performance during EOR. For example, Schmidt *et al.* reported that for PtRu catalysts the formation of chemisorbed species originating from ethanol oxidation is partially inhibited, which prevents poisoning [21]. Enhancing the effect of ruthenium was also reported by Fujiwara *et al.* [22], according to which, Ru increases the oxidation rate of the intermediates adsorbed on the catalysts surface. Besides the Sn and Ru metals, platinum is also mixed with other metals to obtain binary catalysts, such as W, Pd, Rh, Re, Mo and others, however these catalysts are not as efficient as PtSn and PtRu nanoparticles.

The third generation of Pt-based catalysts for EOR are ternary systems, among which the subject of increasing interest were PtRuSn, PtRhSn, PtIrSn, PtIrMo and PtRuMo nanoparticles [12]. Generally, the addition of the third element enhances the EOR performance, mostly due to the modification of the electronic states of the alloys. Among other ternary systems, the especially interesting catalysts are those, which contain Pt-based binary nanoparticles deposited on larger oxide nanoparticles. An example of this type of catalysts is PtRh/SnO_2, which is currently considered as the most efficient catalysts for the EOR [15,16,23]. The crucial role in these catalysts is played by platinum, because the adsorption of ethanol, which undergoes dehydrogenation, occurs on its surface. On the other hand, these catalysts have a high selectivity towards CO_2 due to the presence of rhodium, which favors the cleavage of the C-C bond in the ethanol molecule. The role of SnO_2 is the adsorption and dissociation of H_2O on its surface to provide OH groups to oxidize CO and possibly to reduce the PtOH and RhOH formation (making Pt and Rh available to react with ethanol). The adsorption and dissociation of H_2O on SnO_2 have been verified in a number of studies [24,25]. In general, on oxide surfaces, water molecules are adsorbed on the metal ions with the transfer of one of the protons to a neighboring oxygen atom. A ‘carpet’ of OH groups mediates the interaction between the oxide surface and the environment. Oxide surfaces behave as non-polarizable interfaces, in which the electrical state is controlled by the solution’s pH and the effect of the electrode potential is negligible even for conductive oxides [26].

Most of currently used catalysts for ethanol oxidation are in the form of spherical nanoparticles, lacking of specific crystallographic facets [19,27,28], while, there are studies showing that the oxidation of ethanol occurs more or less efficiently depending on the arrangement of atoms on the surface of nanoparticles [29,30]. Several research groups synthesized catalytic nanoparticles for EOR, which were characterized by precisely defined

shapes and showed greater activity than spherical nanoparticles [29,31,32]. An interesting variation of nanoparticles with a well-defined polyhedral shape, are the so-called nanoframes with hollow interior, which increases their catalytically active surface [17,31,33,34]. In addition, they provide a large number of terraces and atomic steps, which are catalytically very active [35,36].

1.2. Synthesis of shape-controlled nanoparticles

Generally, the syntheses of both shape controlled and regular spherical nanoparticles can be dived into two stages: nucleation of seeds and further growth of the seeds into nanoparticles. Both processes strongly depend on kinetic and/or thermodynamic control. By varying the synthesis conditions, nanoparticles differing in shape, size and composition can be obtained. Understanding the impact of changing the reaction parameters on the synthesized products is crucial to obtain nanoparticles suitable for a specific application.

1.2.1. Nucleation of seeds

The first stage of each synthesis is the nucleation of the seeds. Unfortunately, due to the lack of suitable experimental methods it is difficult to observe this process. However, there is a theoretical description of the nucleation. During nucleation, the zero-valence atoms, formed either from ion reduction or bonds breaking of the compounds, collide and produce small clusters of atoms. These clusters, or seeds, are thermodynamically unstable and they can be dissolved before they reach their stable form, or they can overcome the critical free energy barrier and become thermodynamically stable. According to the classical theory, nucleation can be described as follows [37]:

$$\Delta G_r = 4\pi r^2\gamma + \frac{4}{3}\pi r^3 \Delta G_V = 4\pi r^2\gamma - \frac{4}{3}\pi r^3 \frac{RTlnS}{V_m}, \quad (4)$$

where ΔG_r is the total free energy, γ is the surface free energy, ΔG_V is the crystal free energy, R is the ideal gas constant, T is the reaction temperature, V_m is the molar volume and S is the supersaturation of the solution defined as the ratio between the solute concentrations at saturation and the equilibrium conditions. Because the surface free energy is always positive and the crystal free energy is negative, it is possible to find a maximum free energy, which a nucleus will pass through to form a stable nucleus. This is by differentiating ΔG with respect to the radius r and setting it to zero:

$$\frac{\mathrm{d}\Delta G}{\mathrm{d}r} = 0, \tag{5}$$

Which gives a critical free energy [38]:

$$\Delta G_{crit} = \frac{4}{3}\pi\gamma r_{crit}^2 \tag{6}$$

$$r_{crit} = \frac{-2\gamma}{\Delta G_V} \tag{7}$$

The critical free energy is the energy, which must be reached to obtain stable nuclei [39,40]. Similarly, the critical radius is the minimum radius, at which a particle can survive and not be dissolved. Based on the above equations, it can be seen that the nucleation can be accelerated by the high reaction temperature and a large degree of supersaturation.

1.2.2. Growth of nanoparticles

Classical growth of the nanoparticles can be divided into four main stages: i) generation of growth species, ii) diffusion of the growth species from bulk to the growth species, iii) adsorption of the growth species onto the growth surface, iv) surface growth through irreversible incorporation of growth species onto the solid surface. Generally, the above steps can be gathered into two groups: i) diffusion, which comprises generation, diffusion and adsorption of growth species onto the growing surface; ii) surface process, which includes incorporation of growth species adsorbed on growth surface into the solid structure [41]. Due to the fact that growth is a diffusion-dependent process, therefore the Fick's first law can be applied [42]:

$$J = 4\pi x^2 D\frac{dC}{dx}, \tag{8}$$

where J is the total flux of growth species passing through a spherical plane with radius x, D is the diffusion coefficient and C is the concentration at distance x. For spherical nanoparticles in the solution the above equation can be rewritten as [39]:

$$J = \frac{4\pi Dr(r+\delta)}{\delta}(C_b - C_i), \tag{9}$$

where δ is the distance from the particle surface to the bulk concentration of growth species in the solution, C_b is the bulk concentration of growth species in the solution and C_i is the concentration of growth species at the solid-liquid interface. By integration of C(x) from ($r + \delta$) to r, because J is constant irrespective of x, the following equation is obtained:

$$J = 4\pi Dr(C_b - C_i), \quad (10)$$

Analogously this equation can be written for the rate of surface reaction *k*, which is assumed to be independent on the particle size:

$$J = 4\pi r^2 k(C_i - C_r), \quad (11)$$

where C_r is the solubility of the particles. From the two last equations it follows that the growth of nanoparticles could be limited either by diffusion or by the rate of reaction of the species growing on the surface [38,41].

1.2.3. Controlling of shape and chemical composition during synthesis of nanoparticles

Several synthesis parameters strictly affect the shape of the nanoparticles. Among others, using specific, so-called capping agents can result in obtaining nanoparticles with different shapes. Capping agents are ionic species, small molecules, or macromolecules that can selectively bind to different types of facets on a nanocrystal to alter their specific surface free energies and thus their proportions in terms of area [43,44]. Thermodynamically, nanoparticles prefer to take a shape having the lowest total surface free energy, which is a sum of the products of the area and specific surface free energy for all facets on the surface of the nanoparticles. Capping agents bind with specific facets, lower the specific surface free energy and thus maximize the expression of this type of facets. Therefore, due to the presence of capping agents, it is possible to obtain nanoparticles with a shape, which is energetically unfavorable in normal conditions (without capping agents). For example, by varying the capping agent type and concentration, platinum nanoparticles could be synthesized in the shapes of tetrahedra [45], octahedra [46] or cubes [47]. Shape control by using capping agents is an example of thermodynamic control, but the synthesis could proceed under kinetic control. This can be achieved by a number of ways, including variations of reagent concentration and reaction temperature, the choice of a specific type of reductant or precursor [48,49]. Specially, controlling the precursor addition rate is an easy and effective way of manipulating the reaction kinetics. All these parameters affect the rate of atom diffusion during synthesis and the rate of atom deposition on the formed nanoparticles.

It is possible to obtain multimetallic nanoparticles during the synthesis. There are many reports about syntheses of binary [50], ternary [51] and even quaternary [52] nanoparticles. Multimetallic nanoparticles can vary due to the atoms arrangement within the nanoparticles (Figure 3). Among them, alloys and phase-segregated nanoparticles can be

distinguished. Alloy nanoparticles can be synthesized based on co-reduction of two or more metal precursors. As a result, nanoparticles consisting of a mixture of both metals can be obtained. These metals can be mixed randomly or in form of an ordered structure. Mixing of two metals (M and N) will be favored when (i) the M−N bond is stronger than both the N−N and the M−M bonds; (ii) the two metals have similar lattice parameters (e.g., crystal structure and lattice constant); and (iii) the two metals share similar surface energies [53]. However, more interesting are phase segregated multimetallic nanoparticles. They can take the form of simple core-shell NPs [54], core-shell with ultra-thin shell (from one to six atomic monolayers) [55], or even core-frame structure, where one metal forms the core, while the second is deposited on the edges of the core [56]. The synthesis of phase-segregated multimetallic nanoparticles typically involves a seed-mediated approach, in which the core nanocrystals (often referred to as seeds or templates) act as heterogeneous nucleation sites for the metal atoms, generated through the chemical reduction or thermal decomposition of a metal precursor [54]. The phase-segregated multimetallic nanoparticles have some advantages over the monometallic and even alloy nanoparticles. Among others, they exhibit enhanced catalytic performance through electronic coupling and the strain effect. Moreover they can improve the chemical and the thermal stability and tune the optical properties. Finally, they can serve as a critical intermediate in the formation of other types of structures (e.g., boxes, cages, or frames) [57].

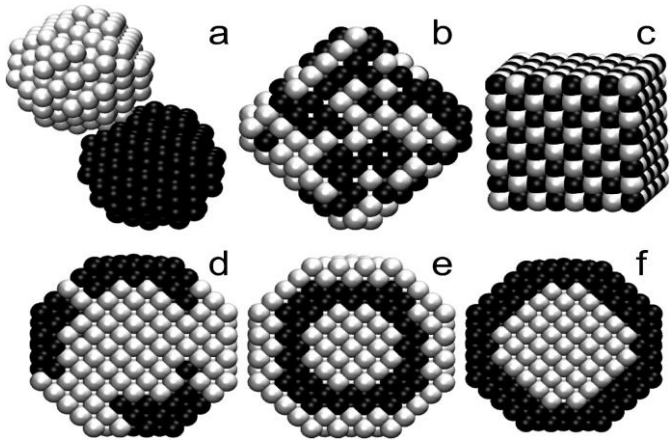

Figure 3. Schematic presentation of possible atom arrangement in bimetallic nanoparticles, a) two separately monometallic nanoparticles; b) random bimetallic alloy; c) ordered intermetallic compound; d) clusters of two different metals in one nanoparticles; e) core-double shell and f) core-shell structures. Reprinted with permission from [58]. Copyright (2015) American Chemical Society.

As mentioned before, the most popular synthesis method to obtain alloy nanoparticles is co-reduction. This method involves simultaneous reduction of two metal precursors to zero-

valent atoms, which then nucleate and grow together to generate alloy nanoparticles. Overall, the final structure of the nanoparticles can be tailored by varying the experimental parameters such as the reduction potentials of the metal ions involved, the strength of the reducing agent, the capping agent, and the reaction temperature. Among these parameters, the reduction potential is especially important. It is a generally accepted rule, that metal ions with higher reduction potentials are reduced faster than those having lower reduction potentials. Only metals with small differences in their reduction potentials can be reduced at the same time and form an alloy. However, the reduction rates of the two precursors can be synchronized by varying the molar ratio of these precursors. For example, there is a large reduction potential difference between gold and silver (+1.5 and +0.8 V, respectively), therefore they cannot be reduced at the same time and obtaining an alloy seems to be impossible. However, Sun and co-workers synthesized AuAg alloy nanoparticles. They found that a higher concentration of Ag ions in the reaction mixture could compensate its slower reduction rate and lead to a simultaneous nucleation and growth with Au. They demonstrated that a molar ratio of 1:10 for Au and Ag led to a final composition of $Au_{60}Ag_{40}$ [59].

Seed mediated growth is a more sophisticated method of synthesizing multimetallic nanoparticles. In this method the reduction of the metal precursors occurs at different times and even in different solutions. First, reduction and homogeneous nucleation of first metal (or alloy) occurs and a seed is formed. Then, seeds are transferred to a solution containing another metal precursor, which is reduced and heterogeneously nucleates on the seeds. Depending on the shape of the seed, nanoparticles with different shape can be obtained [60]. For example, it has been proven that the growth of single crystal seeds could give rise to octahedra, octagonal rods, cubes, rectangular bars, or cuboctahedra; singly twinned seeds would grow into bipyramids; multiply twinned seeds were correlated with decahedra, icosahedra, and pentatwinned nanorods/nanowires; and seeds with stacking faults would result in the formation of triangular or hexagonal nanoplates [61]. These general rules have exceptions, Habas *et al*. [62] show, that if the deposition of metal atoms on seeds is not epitaxial due to the large lattice mismatch, the symmetry of growth is breaking, which results in obtaining of anisotropic nanoparticles.

1.3. Obtaining hollow nanoparticles

A characteristic group of shape-controlled nanoparticles, are so-called hollow nanoparticles, which have unique physicochemical properties, which differ from their solid counterparts. The most studied examples of hollow nanoparticles are nanoboxes [63,64],

nanocages [65,66] and nanoframes [67,68] (Figure 4). Among those, nanoframes have the most open structure, when compared with other types of hollow nanostructures of similar sizes. It is possible to obtain nanoframes with different shapes, recently triangular [69], cubic [34], octahedral [67], and decahedral [70] nanoframes have been prepared using various methods.

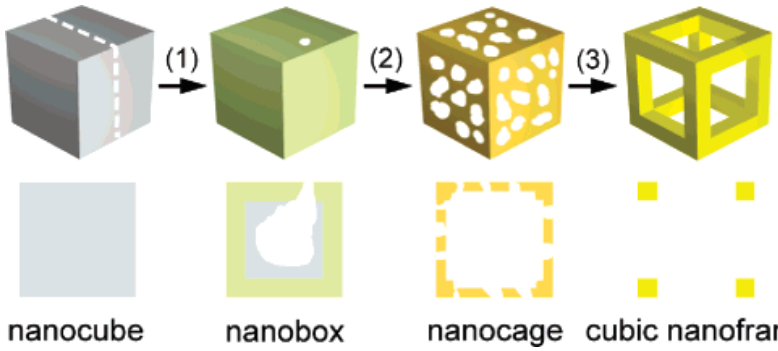

Figure 4. Schematic representation of the differences between a solid cubic nanoparticle, nanobox, nanocage and nanoframes structures. The upper row shows 3d models, while the lower row shows the cross-section along the line drawn on the nanocube. Reprinted with permission from [71]. Copyright (2007) American Chemical Society.

The nanoframes have many advantages, among others, they provide many edges and corners, which are catalytically active due to the low coordination number of atoms on these edges and corners. Another advantage of the nanoframes is the high surface area to volume ratio, due to the removal of the non-functional atoms from the interior of nanoparticles. This operation not only improves the efficiency in catalytic reactions, but also minimizes the usage of precious metals such as platinum, rhodium, gold. There are four basic synthetic routes to obtain nanoframes: chemical etching, galvanic replacement reaction, Kirkendall effect and so-called one-pot synthesis. The first three methods require previously prepared “templates”, from which the nanoframes will be shaped. In the last method a template is not required, nanoframes are formed at the stage of synthesis and do not require further treatment.

a) Chemical etching

The chemical etching method requires the use of appropriate etchant selectively dissolving the less stable elements and/or certain facets of the nanostructures. This approach allows to precisely control the frames edges thickness. For example, Xia and co-workers [71] prepared Au nanoframes from bimetallic AuAg nanoparticles by the chemical etching of Ag. As an etchant, they used the $Fe(NO_3)_3$ solution, to obtain a dealloyed AuAg phase. By controlling the etching conditions, besides nanoframes, they could also obtain nanocages.

Another popular etchant is O_2, Chen *et al*. [17] reported that the presence of oxygen could transform $PtNi_3$ solid nanoparticles to Pt_3Ni nanoframes in two weeks without any other treatment. The transformation of the nanoparticles to nanoframes could be accelerated to 12 hours by increasing the etching temperature to 120°C. In a control experiment, where etching was conducted in inert gas atmosphere, no frames formation was observed. The evolution from $PtNi_3$ solid polyhedrons to Pt_3Ni nanoframes was ascribed to preferential oxidation of Ni on the facets by O_2, and dissolution of the formed nickel oxides in the presence of oleylamine ligands, which were used as a reducing agent in the nanoparticles synthesis [69]. Most recently, an effective two-phase approach has been developed by Li *et al*. [32], in which the $PtNi_{10}$ nanoctahedra were corroded to Pt_4Ni nanoframes. A "synergetic corrosion" mechanism was suggested, in which several species (i.e., O_2, H_2O, H^+, oleylamine and $EDTA^{4-}$) were involved. Oleylamine could play a crucial role in dispersion as well as in etching by coordinating with Ni^{2+} ions. It was observed that depending on the amount of EDTA-2Na and thus by influencing the corrosion rate, $PtNi_4$ porous octahedra or nanoframes were generated. At last, the most significant feature of the two-phase process was controlling the corrosion reaction under mild conditions with an accelerated rate. In this system, an aqueous phase in the presence of $EDTA^-2Na$ caused obvious enhancement in corrosion rate to generate the $PtNi_4$ nanoframes.

b) Galvanic replacement reaction

One of the easiest methods of obtaining hollow nanoparticles are galvanic replacement reactions. This elegant approach is widely employed to transform solid metal nanoparticles into multimetallic hollow NPs [72,73]. The galvanic replacement reaction (GRR) requires sacrificial template nanoparticles and a metal precursor. During the GRR, the template material is oxidized and dissolved, while metal ions from metal precursor are reduced and the resultant atoms are deposited on the surface of the template. The driving force of the galvanic replacement reaction is the difference in redox potential between the two metals [74,75]. Typically for the template a cheap metal is used, for example silver [76,77]. As a representative example of GRR, Xia *et al*. [78] prepared Au-based nanoframes via galvanic replacement reaction between Ag nanocubes (template) and $HAuCl_2$ (metal precursor). The standard reduction potential of the $AuCl^{2-}$/Au pair is 1.11 V (vs. SHE), which is higher than that of AgCl/Ag (0.22 V vs. SHE). Thus, the Ag nanocubes can be oxidized by $AuCl^{2-}$. Simultaneously, deposition of Au on the edges of the oxidized Ag nanocubes occurs, while pinholes are formed on the Ag facets. Over time, the pinhols are growing and finally merge

forming cubic nanoframes structures with Au edges. Also nanoframes with other shapes can be obtained by GRR. Li *et al*. [79] obtained Au-Ag octahedral nanoframes by reduction of $AgNO_3$ by copper chloride and $HAuCl_4$. Of course, nanoframes from other metals, not only Au can be obtained by galvanic replacement reactions. Tsuji *et al*. [80] reported the synthesis of triangular Ag-Pd alloy nanoframes by galvanic replacement reaction between triangular Ag nanoplates and Na_2PdCl_4, with post-treatment using NaCl in an aqueous solution.

c) Kirkendall effect

In the Kirkendall effect, hollow nanoparticles are formed due to the difference in the diffusion rate of the core atoms outwards, balanced by the opposing flow of vacancies, which coalesce into voids [81]. The Kirkendall effect may occur alone [82], or be coupled with the galvanic exchange reaction. For example, González *et al*. [83] performed a series of galvanic replacement and Kirkendall effect reactions at room temperature to obtain multimetallic hollow nanoparticles with very different morphologies and chemical compositions, such as double-walled Au-Ag nanoboxes, trimetallic Pd-Au-Ag nanoboxes and cylindrical hollow nanostructures. After some modifications to the synthetic protocol, they also produce metal nanoframes. Example of the Kirkendall effect occurring without additional processes is the synthesis of Cu_3Pt nanoframes with polyhedral morphology reported by Han *et al*. [84]. The first step in the preparation of nanoframes was to synthesize polyhedral Cu–Pt nanoparticles with a core-shell structure. This could be obtained by anisotropic growth of Pt on multiply twinned Cu seed particles. The next step was a subsequent transformation of core-shell nanoparticles into Cu_3Pt alloy nanoframes due to the Kirkendall effect between the Cu core and Pt shell. After structural evolution, the obtained Cu_3Pt nanoframes possess a rhombic dodecahedral morphology of their core–shell parents.

1.4. Aims and theses of the study

The main aim of the study was to determine the physical processes leading to the formation of PtNi and PtRhNi hollow nanoframes-based catalysts for ethanol oxidation reaction during their synthesis. This goal was realized by two approaches leading to the formation of hollow nanoparticles: either by obtaining Pt_3Ni and PtRhNi nanoframes decorated with small SnO_2 nanoparticles, or by obtaining PtNi and PtRhNi nanoframes covered by a thin, incomplete SnO_2 layer. In order to achieve these objectives, the following goals were defined:

1. Synthesis of phase-segregated solid $PtNi_3$ and PtRhNi rhombic dodecahedral nanoparticles consisting from a nickel core and a PtNi or PtRhNi frame around the core edges (Figure 5a), which serve as a starting material in obtaining hollow nanoframes. At this stage it is crucial to understand the thermodynamic and kinetic aspects, which affect the growth of the polyhedral nanoparticles, due to the fact that even a small change in parameters can lead to obtaining different products.

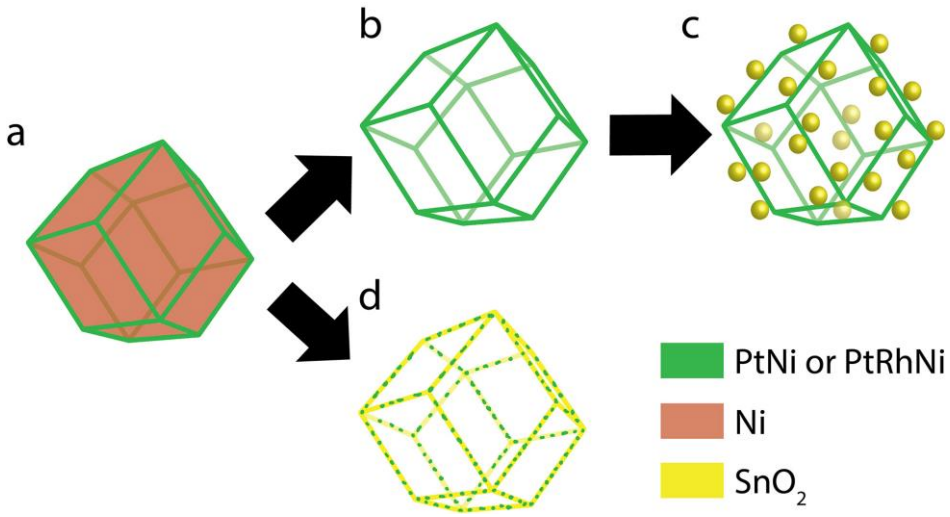

Figure 5. Schematic representation of the route of obtaining nanoframes-based nanocatalysts; a) synthesis of the solid rhombic dodecahedral nanoparticles; b) etching the Ni-core from the solid nanoparticles presented in a); c) decoration of the etched nanoframes with small SnO_2 nanoparticles; d) galvanic replacement of Ni atoms from the core of the nanoparticles presented in a) with Sn ions from the $SnCl_4$ solution.

2. Obtaining hollow Pt_3Ni and PtRhNi nanoframes-based catalysts by:
   a) Etching of the solid $PtNi_3$ and PtRhNi rhombic dodecahedral nanoparticles (Figure 5a) into Pt_3Ni or PtRhNi nanoframes (Figure 5b) and decorating them subsequently with small SnO_2 nanoparticles (Figure 5c). The main issues are the thermodynamic explanation of the etching process and the connecting of the nanoframes with SnO_2 NPs in a controlled manner based on their respective zeta potential values.
   b) Galvanic replacement reaction between the nickel core of the solid $PtNi_3$ and PtRhNi rhombic dodecahedral nanoparticles (Figure 5a) and Sn ions from $SnCl_4$ solution resulting in the formation of PtNiSn or PtRhNiSn nanoframes and after heat-treatment of $PtNiSnO_2$ or $PtRhNiSnO_2$ nanoframes (Figure 5d). The main aim is to understand the mechanism of the exchange between Ni atoms and Sn ions.

3. Electrochemical tests to prove that the obtained nanoframes-based catalysts are efficient towards ethanol oxidation reaction.

On the basis of the above goals, the following theses were determined:

1. The phase segregation of platinum and rhodium at the edges of the solid $PtNi_3$ and PtRhNi rhombic dodecahedral nanoparticles occurs due to the diffusion of these elements from the core, where they initially were, to the edges.
2. It is possible to synthesize PtNi and PtRhNi nanoparticles with different morphologies by manipulating the synthesis parameters affecting the kinetics of the synthesis reaction.
3. The etching of the solid nanopolyhedra to nanoframes can be described thermodynamically and it is dependent on the cohesive energy.
4. It is possible to decorate the nanoframes with small SnO_2 nanoparticles in a controlled manner based on their opposite zeta potentials.
5. The galvanic replacement reaction strongly depends on the concentration of the reagents as well as on the type of the used solvent.

Chapter 2: Materials and methodology

2.1. Reagents

Nickel(II) nitrate hexahydrate, chloroplatinic acid hexahydrate, oleylamine, tin(IV) chloride pentahydrate and 5 wt.% Nafion were purchased from Sigma Aldrich. Acetic acid was purchased from Merck Milipore. Rhodium(III) chloride hydrate was purchased from Acros Organics. Citric acid monohydrate, isopropanol and ethanol were purchased from POCH. Ethylene glycol was purchased from Avantor and Vulcan XC-72R was purchased from Cabot. All reagents were used as received without further purification.

2.2. Experimental methods

2.2.1. Preparation of nanoframes-based catalysts

a) Synthesis of $PtNi_3$ and PtRhNi phase-segregated solid nanopolyhedra

The $PtNi_3$ and PtRhNi rhombic dodecahedral polyhedra were synthesized using a modified protocol previously reported by Chen *et al*. [17]. In a typical synthesis of $PtNi_3$, 50 mg of $H_2PtCl_6 \cdot 6H_2O$ and 43 mg of $Ni(NO_3)_2 \cdot 6H_2O$ were dissolved in 1 mL deionized water and then injected into 25 mL oleylamine in a three-necked flask at 160°C in argon atmosphere. Then the solution was heated to 270°C (with a heating rate of ~3°C/min) until it turned into a black slurry. The temperature was maintained for additional 3 min, after this time the solution was cooled down to room temperature. The synthesis of the PtRhNi nanopolyhedra was performed similarly, however, 10 mg of $H_2PtCl_6 \cdot 6H_2O$ were replaced by 10 mg of $RhCl_3 \cdot H_2O$. The obtained nanoparticles were collected by centrifugation (3000 rpm) and washed three times with a mixture of hexane and ethanol.

b) Control experiments

The syntheses of overgrown PtNi NPs (synthesis 1 and 2) and core-shell nanoparticles (synthesis 3), as well as the synthesis of PtNi nanoparticles in air (synthesis 4) were performed according to the same protocol as the $PtNi_3$ nanopolyhedra, however with parameters changed according to Table 1. Similarly, the syntheses of the RhNi and of the overgrown PtRhNi nanoparticles were conducted according to the previously described protocol with parameters changed according to Table 1.

Table 1. Parameters changed in the syntheses during control experiments.

	Synthesis 1	Synthesis 2	Synthesis 3	Synthesis 4	Synthesis 5	Synthesis 6
Addition temperature [°C]	160	160	40	160	160	160
Method of adding metal precursors to oleylamine	in two portions within 2 minutes	in three portions within 2 minutes	one portion, fast injection	one portion, fast injection	one portion, fast injection	one portion, fast injection
Reaction atmosphere	Inert (argon)	Inert (argon)	Inert (argon)	Air	Inert (argon)	Inert (argon)
Precursor metals	Pt, Ni	Pt, Ni	Pt, Ni	Pt, Ni	Ni, Rh	Pt, Ni, Rh
Heating rate [°C/min]	3	3	3	3	3	8

c) Chemical etching of phase-segregated solid nanopolyhedra into nanoframes

The centrifuged and washed $PtNi_3$ and PtRhNi nanopolyhedra were transferred to a two-necked flask with 20 mL acetic acid. The resulting solution, after being sonicated for 30 min, was kept at 100°C for 10h under stirring in air atmosphere. After this time, the solution was cooled down to room temperature, centrifuged (3000 RPM) and washed 3 times with ethanol.

d) Synthesis of SnO_2 nanoparticles

Sol-gel microwave-assisted synthesis of SnO_2 was performed based on the protocol proposed by Zhu *et al*. [85]. First, 10 mL of 0.1 M $SnCl_4 \cdot 5H_2O$ and 10 mL of 0.1M citric acid solutions were prepared separately. Subsequently, the tin chloride and citric acid solutions were mixed thoroughly and sonicated for 30 min. Afterwards, the obtained 20 mL of the solution was placed in a microwave oven with a maximum power of 280 W and heated for 12.5 min. The final product was washed three times with ethanol.

e) Decorating the Pt_3Ni and PtRhNi nanoframes with SnO_2 nanoparticles

First, the pH of the solutions containing Pt_3Ni or PtRhNi nanoframes obtained by chemical etching, as well as the solution with SnO_2 nanoparticles was adjusted to 4.5 and separately sonicated for 1 hour to disperse the nanoparticles in ethanol. After this time

10 mL of the SnO_2 NPs suspension (approximately 13 mg of SnO_2 NPs) was added dropwise to the Pt_3Ni or PtRhNi nanoframes. The obtained suspension of SnO_2@Pt_3Ni and SnO_2@PtRhNi heteroaggregates was sonicated another 1 hour and washed 3 times with ethanol.

f) Galvanic replacement reaction

The centrifuged and washed nanopolyhedra were dispersed in 5 mL of 1M solution of $SnCl_4$•$5H_2O$ in ethylene glycol. The galvanic replacement reaction proceeded at room temperature with sonication for 30 minutes. Next, the solution was mixed with chloroform, centrifuged (3000 RPM, 30 min) and washed three times with ethanol. The kinetics of the galvanic replacement reaction was studied by quenching the reaction at different stages i.e. after 2, 11, 15 and 30 minutes. The reaction was stopped as follows: to the nanoframes suspension acetone was added and the obtained solution was immediately centrifuged (14000 RPM, 1 min). The obtained nanoframes-containing precipitate was washed with ethanol and deposited on the TEM grid. The time values given above (2 min, 11 min, 15 min and 30 min), are times at which the samples were probed from the solution. To each time the 2 minutes -1 min for centrifugation with acetone and 1 min for dropping the sample on the TEM grid and drying have to be added resulting in times of 4 min, 13 min, 17 min and 32 min.

g) Catalysts preparation

The obtained Pt_3Ni and PtRhNi nanoframes, SnO_2@Pt_3Ni, SnO_2@PtRhNi heteroaggregates as well as PtNiSn and PtRhNiSn nanoframes after galvanic replacement reaction, were deposited on carbon black Vulcan XC 72R (Cabot) with a 20% Pt loading (based on the ICP MS measurement). A proper amount of carbon black was dispersed in ethanol and sonicated for 30 min. After this time, the nanoframes containing solutions were added drop-wise to the carbon suspension and were stirred overnight. The obtained nanocatalysts were centrifuged (3000 RPM, 30 min). The Pt_3Ni/C and PtRhNi/C, SnO_2@Pt_3Ni/C and SnO_2@PtRhNi/C were dried in air at 200°C for 14h to remove surfactants and obtain a Pt-skin surface on the nanoframes, while PtNiSn and PtRhNiSn were dried in air at 200°C for 7h only to remove surfactants without obtaining the Pt-skin surface. The as-prepared catalysts were ready for electrochemical measurement.

2.2.2. Transmission electron microscopy – fundamentals, sample preparation and measurements

2.2.2.1. Basic principles of transmission electron microscopy

The transmission electron microscope (TEM) in transmission mode works on a similar principle as a light microscope, except that instead of light, the sample is illuminated by the electron beam, as the electrons possess a wavelike character. According to Louis de Broglie, the wavelength of the electrons is given by the equation [86]:

$$\lambda = \frac{h}{p} = \frac{h}{m\,v} \tag{12}$$

Where h = 6.626 * 10^{-34} [J s] is the Planck constant, p is the momentum, m is the mass and v represents the speed of the electrons. As the speed of the electrons emitted by the electron source in the TEM depends on the accelerating voltage, by increasing this voltage it is possible to increase the speed of electrons, and in consequence, decrease the electron wavelength. For example, electrons accelerated by 100 kV have a relativistic wavelength equal to 0.00370 nm, while electrons accelerated by 300 kV have a relativistic wavelength equal to 0.00197 nm [87]. The direct relationship between the electron wavelength and the accelerating voltage can be written as:

$$\lambda = \frac{h}{\sqrt{2m_0 eV}} \tag{13}$$

where, m_0 is the electron mass, e is the electron charge and V is the accelerating voltage. However, due to the fact that electrons at energies near 100 keV have velocities greater than ½ of the velocity of light, it is required to modify the above equation to include the relativistic effects [87]:

$$\lambda = \frac{h}{\sqrt{2m_0 eV\,(1+\frac{eV}{2m_0 c^2})}} \tag{14}$$

where c is the velocity of light. The relation between the electron wavelength and the accelerating voltage is important due to the resolution limit proposed by Ernst Abbe expressed by the equation:

$$d = \frac{0.612\lambda}{n\,sin\alpha} \tag{15}$$

where n is the refractive index of the medium between the object and the objective and α is the half the angle of the cone of light from the specimen plane accepted by the objective. As it can be seen, by decreasing the electron wavelength, it is possible to get a better resolution. By using visible light in the optical microscope, it is possible to obtain a resolution of about

250 nm in the best case, however by using electrons accelerated by voltage in the TEM, it is possible to obtain a resolution below 1 nm.

The schematic diagram of the TEM is shown in Figure 6. The electrons are emitted from the electron source, which can be a lanthanum hexaboride (LaB_6) crystal or a field emission gun (FEG), and they are accelerated in the area between the anode and the cathode. The accelerated electrons pass through a system of apertures and electromagnetic lenses, where the electron beam is focused. Next, the focused electron beam penetrates through the sample (which is typically about 100 nm thick) and passes through the projector lenses, which expand the electron beam onto a fluorescent screen, where image is projected. The image can be observed directly on the fluorescent screen or a charged coupled device (CCD) camera can be used to record the images. Some of the TEMs are equipped with a spherical aberration (Cs) or with a chromatic aberration (Cc) corrector, which improves the TEM resolution. The Cs corrector cancels the positive spherical aberration coefficient of the objective and condenser lenses by producing a negative spherical aberration coefficient. Conversely, the Cc corrector produces a negative chromatic aberration making the chromatic aberration of the image-forming lens or the probe-forming lens to be zero [88]. It is worth noticing that all of the electron microscopes operate under vacuum, due to the interactions of electrons with atoms in air.

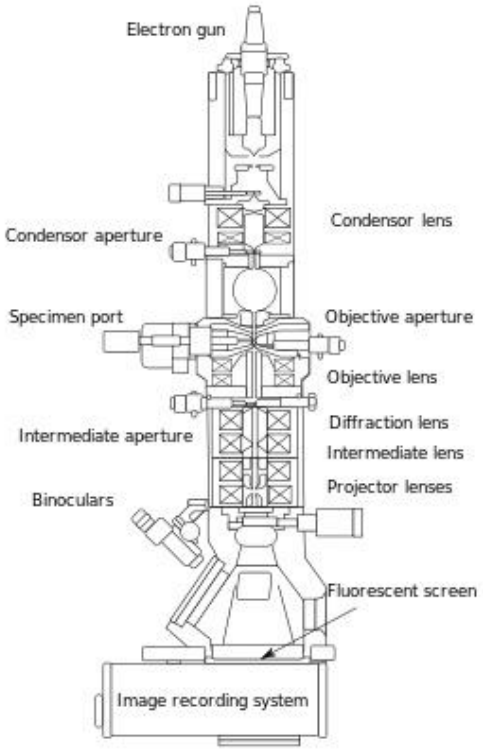

Figure 6. Schematic representation of typical TEM optical components [89].

It is possible to analyze the samples in different modes such as:

a) In the basic TEM mode, the image is formed by the electron beam transmitted through the sample being illuminated by a parallel beam.

b) Scanning transmission electron microscopy (STEM) mode. In this mode the electron beam is focused to small spot (0.2 nm to 10 nm) and scans in transmission over the sample point by point. Due to the electron-sample interaction (Figure 7), diffracted secondary and backscattered electrons are transmitted and collected by dedicated detectors, which are typically the bright field and the dark field detector. The background of the image is bright on the bright field detector, because it includes the transmitted beam, while the dark field detector excludes the transmitted beam, what causes the background to be dark. A specially interesting variation of the dark field detector is the high-angle annular dark-field (HAADF) detector, which allows to obtain so-called Z-contrast images. The HAADF detector collects the inelastically scattered electrons at high angles, so the HAADF image intensity is expressed by:

$$I = Z^{\alpha} \tag{16}$$

where I is the image intensity, Z is the atomic number (Z-number) and α is a number from the range between 1.6-1.9 for most cases [90]. From above relation it is obvious that on the HAADF images atoms with higher Z-number will be brighter than atoms with lower Z-number. This technique is especially useful during the study of the phase-segregated bimetallic materials.

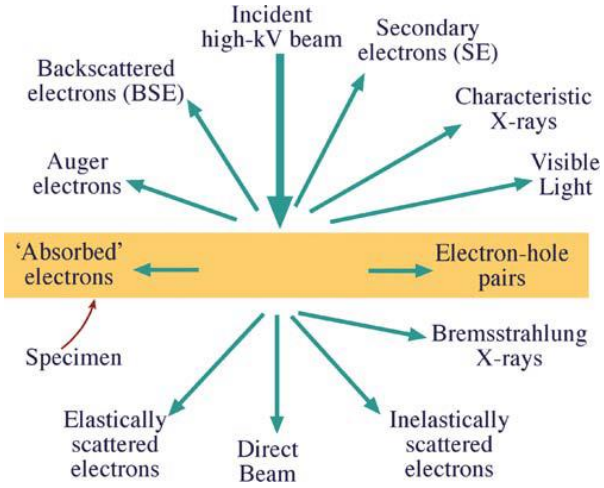

Figure 7. Types of signals generated during electron beam-sample interactions. Reprinted with permission from [87]. Copyright (2009) Springer.

c) Selected area electron diffraction (SAED) mode. This mode allows identifying phases and their orientations, giving the exact crystallographic description of crystal defects

produced by deformation or irradiation. The spacing between atoms in the sample are hundred times larger than the electron wavelength, therefore the atoms act as a diffraction grating for electrons. Some of the electrons are transmitted through the sample, but also some of them are diffracted on the atoms. The transmitted electrons form the central, transmitted spot in the SAED image, while the diffracted electrons form the diffraction patterns allow to identify the crystal structure of the sample [86,87]. Single crystalline samples give SAED patterns formed by spots, while polycrystalline samples, including nanoparticles, give ring patterns. The electron diffraction could be described by the Bragg's law:

$$2d\ sin\theta = n\lambda \quad (17)$$

where d is the interplanar spacing, θ is the angle of beam deflection, n is a positive integer and λ is the wavelength. For small values of θ the following relation takes place [91]:

$$\frac{R}{L} = 2\theta \quad (18)$$

where R is the distance between the transmitted and the diffracted spot in the SAED pattern and L is the camera length. By using the above relation, the Bragg's law can be rewritten as follows [91]:

$$Rd = \lambda L \quad (19)$$

This relation is helpful in identifying the phases of the studied sample. By measuring the R value on the diffraction image, and placing in the above formula the known value of the camera length and wavelength, it is possible to calculate the interplanar spacing and consequently to identify the sample.

d) Energy dispersive X-ray spectroscopy (EDS) mode. This mode allows to perform chemical analyses of the observed samples. The EDS method relies on the detection of the characteristic X-rays, which are produced by the interaction of high-energy electrons with the sample. The high-energy electrons emitted from electron gun strike the atom at the ground state and cause the excitation of the electron in inner shell. Due to this excitation, the electron from the inner shell is ejected, which results in creation of an electron vacancy. To fill this vacancy, the electron from outer, high-energy shell drops to the inner shell. The excess of the energy, resulting from electron transfer from outer higher energy shell to the inner lower energy shell, is lowered by emitting a characteristic X-ray [86,92]. This radiation is detected by one semiconductor EDS

detector or a system of combined EDS detectors, which are able to collect more signal in shorter time than a single EDS detector [87].

2.2.2.2. Transmission electron microscopy sample preparation and measurements

To prepare the samples for transmission electron microscopy the nanoparticles were dispersed in ethanol and sonicated for 30 min. Next, few droplets of the nanoparticles suspension were deposited on a Cu carbon film coated TEM grid (300 mesh, purchased from Agar Scientific) and dried in air at room temperature. The as-prepared samples were cleaned in a plasma cleaner for 3 seconds, and then inserted into the TEM.

The morphology of the obtained nanoparticles was examined by scanning transmission electron microscopy equipped with a HAADF detector. Energy dispersive X-ray spectroscopy was used to analyze the local elemental composition of the samples. SAED patterns and High Resolution (HR) STEM images were performed to confirm the crystallinity of the samples. The TEM measurements were conducted on three microscopes:

- aberration-corrected (Cs-corrected) FEI Titan 80-300 operating at 300 kV equipped with a FEG cathode, located at the Faculty of Mechanical Engineering of the Silesian University of Technology. On this microscope STEM overview and HRSTEM images, as well as SAED patterns and EDS point spectra were acquired.
- Double aberration-corrected (Cs and Cc-corrected) FEI Titan^3 G2 60-300 operating at 300 kV equipped with a X-FEG cathode and high-speed, quad-silicon drift EDS detector (Super-X/Chemi STEM), located at Polish Center for Technology Development. On this microscope EDS mappings were performed.
- FEI Talos F200 operating at 200 kV equipped with a FEG cathode and the Super-X in-column EDS detector, located at the University of Warsaw Biological and Chemical Research Centre. On this microscope STEM overview images and EDS mappings were performed.

The TEM images processing was conducted using FEI TEM Imaging & Analysis (TIA) software for STEM images and Gatan Digital Micrograph software for SAED patterns and nanoparticles size measurements. Bruker Esprit software was used to analyze and quantify the EDS data. The particle size distribution was evaluated based on the HRSTEM images taken from different areas of the TEM grids. For each sample, the diameter of 200 nanoparticles was measured. For spherical SnO_2 nanoparticles the diameter was measured, while for solid rhombic dodecahedral and nanoframes the longer diagonal of the

rhombus forming the facet (D) of the nanoparticles (Figure 8). This allowed measuring the size of the nanoparticles regardless of their orientation.

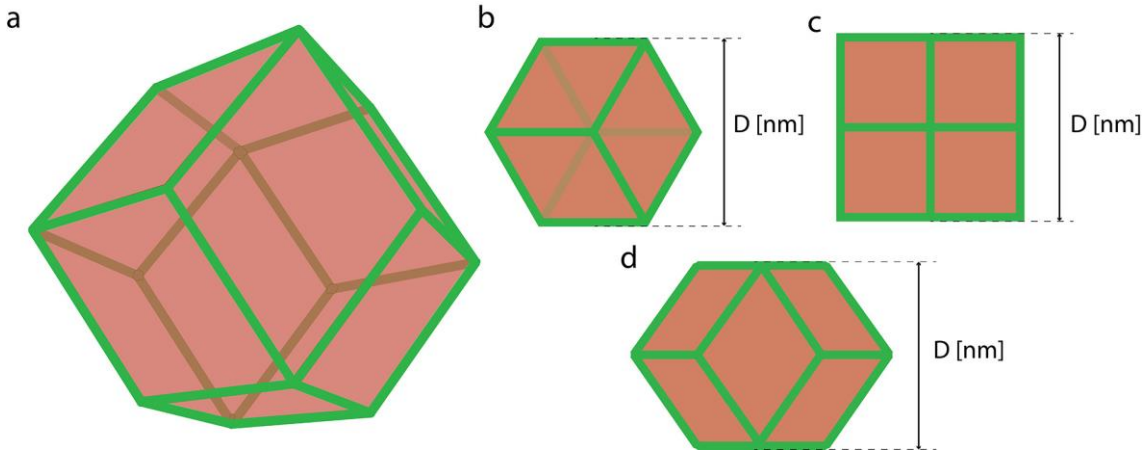

Figure 8. a) Schematic 3D model of the rhombic dodecahedron; b, c, d) three basal 2D projections of the model presented in a) with the longer diagonal of the rhombus forming the facet marked with a line (D).

2.2.3. X-ray diffraction

X-ray diffraction (XRD) is one of the most commonly used non-destructive method to study the structure of the materials. In this technique, monochromatic X-rays are scattered by the crystalline sample [93], which results in the formation of the Bragg peak, when the Bragg's law is fulfilled:

$$2d\ sin\theta = n\lambda \tag{20}$$

where d is the interplanar spacing, θ is the angle of beam deflection, n is a positive integer and λ is the wavelength. The schematic visualization of the Bragg condition is shown in Figure 9.

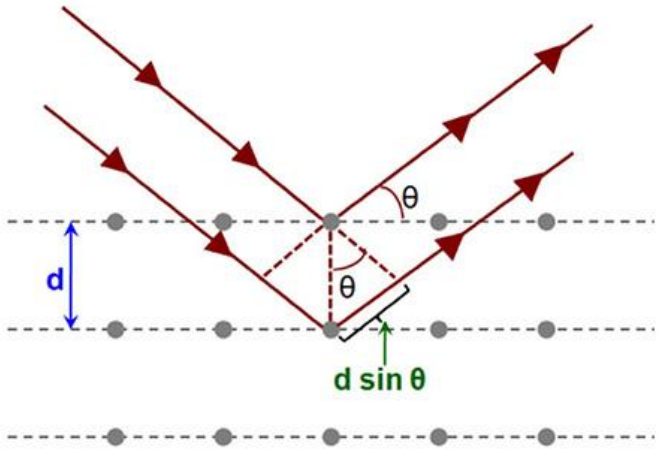

Figure 9. Bragg's Law reflection. The incident X-rays are diffracted on the atoms in crystalline sample [94].

Based on the XRD diffractograms it is possible to obtain information about the crystal structure of the sample, the size of the crystallites, in case of bimetallic samples about the formation of an alloy or phase-segregation and many more [95].

The XRD measurements in the present study were carried out using the X'Pert PRO (Panalytical) diffractometer with Cu Kα (1.5404 Å) radiation, a graphite monochromator and a strip detector (X'Celerator). To preclude any extra diffraction lines, the samples, in form of carbon powder, were placed onto a "zero-background" silicon plate. The experiments were performed at room temperature. The XRD patterns were vector normalized and the base line correction was applied using the Origin software. All reference crystallographic data, such as lattice parameter and the 2θ degree values were taken from the JCPDS files database: JCPDS 87-0646 (Pt), JCPDS 05-0685 (Rh), JCPDS 04-0850 (Ni), JCPDS 88-0287 (SnO_2).

2.2.4. Inductively coupled plasma optical emission spectrometry and inductively coupled plasma mass spectrometry measurements

Inductively coupled plasma optical emission spectrometry (ICP OES) measurements were performed on a Perkin Elmer plasma 40 instrument, to determine the global composition of the nanoparticles. The inductively coupled plasma mass spectrometry (ICP MS) measurements were carried out on a Perkin Elmer NexION 300D instrument in order to prepare catalysts with a 20% Pt loading. The samples were prepared as follows for the measurements: first the sample containing solutions were sonicated for 15 minutes, next 0.5 mL of the respective solutions were collected and evaporated. Subsequently, 2 mL of aqua regia was added to the vial containing the nanoparticles and heated close to 105°C until the precipitate was dissolved (about 40 minutes). After that time the solution was evaporated to a volume of 0.5 mL. The samples prepared in such a way were ready for ICP measurements.

2.2.5. Zeta potential measurements

The zeta potential is calculated based on the electrophoretic mobility of the nanoparticles in the solution. Based on the zeta potential it is possible to define, if the nanoparticles are stable in the solution or do they form aggregates. Also, if we measure the zeta potential of two types of nanoparticles in two solutions, it is possible to verify, if they will connect to each other after mixing both solutions (if they have opposite zeta potentials), or if they will remain separated after mixing the solutions [96,97].

To explain what is the zeta potential, it is necessary to describe the double layer surrounding each nanoparticle in the solution. It consists of an inner region, so-called Stern

layer, at which the ions (cations or anions) are strongly bounded and an outer region, which is called the diffuse layer, where the ions are less firmly connected and can diffuse (Figure 10). An essential part of the diffuse layer is the slipping plane, which is an imaginary boundary, at which the ions and particles form a stable entity. The potential occurring at the slipping plane, is the zeta potential [98,99]. It is worth noting, that the zeta potential strongly depends on the pH: the same nanoparticle suspension can have different zeta potential values at different pH.

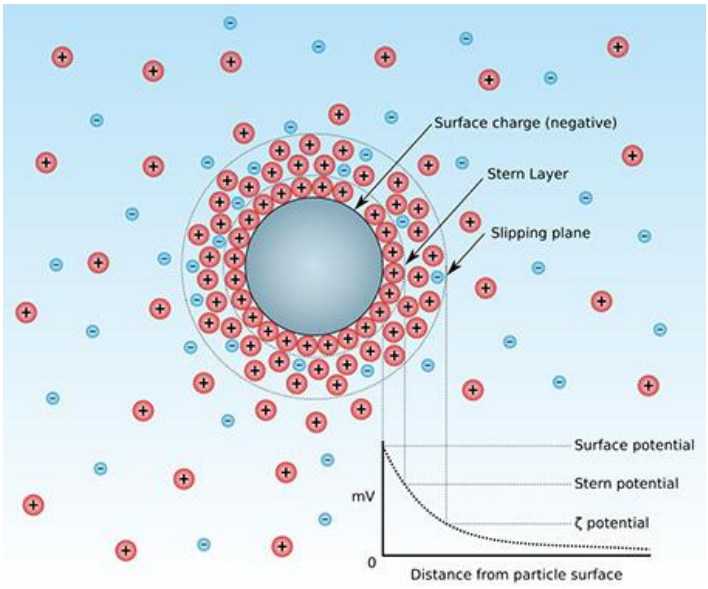

Figure 10. Schematic representation of the double layer surrounding the nanoparticles in the solution [100].

As it was mentioned before, the zeta potential could be calculated from the electrophoretic mobility measurement according to the Henry equation [101]:

$$U_E = \frac{2\varepsilon\zeta f(Ka)}{3\eta} \tag{21}$$

where ζ is the zeta potential, U_E is the electrophoretic mobility, ε is the dielectric constant, η is the viscosity of liquid and *f(Ka)* is the the Henry's function, which generally takes two values, either 1.5 or 1.0, depending on which approximation is used, Smoluchowski or Huckel respectively.

In the present study the zeta potential values as a function of the solution pH of the ethanol suspension containing Pt_3Ni and PtRhNi nanoframes, as well as of the SnO_2 nanoparticles solution were determined by the microelectrophoretic method using a Zetasizer Nano Series from Malvern Instruments. The Smoluchowski model was used in the zeta potential measurements. Each value was obtained as an average of three subsequent runs of

the instrument with at least 20 measurements. All experiments were performed in ethanol at 25°C. Data was analyzed by using the Zetasizer software, the plot was prepared in the Origin Pro 8 software.

2.2.6. Ink preparation and electrochemical measurements

The cyclic voltammetry (CV) is one of the fundamental techniques for the characterization of nanocatalysts. It is based on the linear increasing of the potential vs. time and, after reaching the maximum value of potential, linear decreasing of the potential to the initial value (Figure 11) [102,103]. In each cycle, the first reducing potential is applied (from t_0 to t_1 on Figure 11), next re-oxidation of the analyte occurs (from t_1 to t_2 on Figure 11) [104]. An important parameter of the CV is the scan rate, which is the ratio of changing the potential in time [V s^{-1}]; the lower is the scan rate, the more accurate is the obtained cyclic voltammogram. The CV experiment is performed in a three electrode system composed of a working electrode, a reference electrode and a counter electrode [103,104]. The current is measured between the working and the counter electrode, while the potential is measured between the working and the reference electrode.

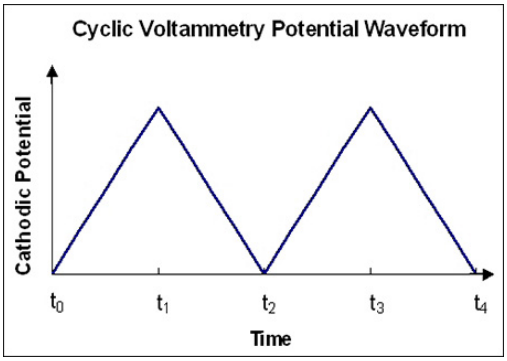

Figure 11. Change of the potential in CV experiments as a function of time [105].

In the present study, for ink preparation 4 mg of the obtained catalysts were dispersed in a previously prepared solution containing 3 ml of ultrapure H_2O, 1 ml of isopropanol, 20 µl of 5 wt.% Nafion. The ink solution was sonicated for 30 min and pipetted (10 µl) onto 5 mm diameter polished glassy carbon discs and dried at room temperature. The so prepared working electrode was ready for electrochemical measurements. The cyclic voltammetry and ethanol oxidation reaction measurements were performed by using a Bio-logic SP-200 potentiostat in a three-electrode electrochemical cell. As a counter and reference electrode, platinum wire and a 3M KCl Ag/AgCl electrode were used, respectively. All the potential values were converted to the reversible hydrogen electrode (RHE) scale. The CV curves were

recorded in previously Ar bubbled 0.1M $HClO_4$ electrolyte, while the EOR measurements were conducted in an electrolyte containing 0.1M $HClO_4$ and 0.5 M ethanol at room temperature. The platinum electrochemically active surface areas (*ECSA*) of the respective catalyst samples, were calculated based on hydrogen desorption peaks on CVs curves measured with 20 mV s^{-1} scan rate according to the equation:

$$ECSA_{Pt}[cm^2] = \frac{Q_H\,[\mu C]}{210\,[\mu C\ cm^{-2}]} \tag{22}$$

where Q_H is the hydrogen desorption charge calculated from the integral of hydrogen desorption peaks in CVs and 210 μC cm^{-2} is a conversion factor, which is associated with the adsorbed hydrogen monolayer [106,107]. The platinum electrochemically active surface areas were converted to specific surface area (*SSA*) according to the formula:

$$SSA_{Pt}[cm^2\ mg^{-1}] = \frac{ECSA_{Pt}[cm^2]}{m_{Pt}\,[mg]} \tag{23}$$

where m_{Pt} [mg] is the mass of Pt on the glassy carbon electrode.

The EOR measurements were conducted with a 10 mV s^{-1} scan rate. The EOR results were normalized by *ECSA* and mass of platinum. As a reference, commercial 50% Pt/C catalyst (Tanaka) was used. The onset potential of all tested catalysts was defined as the intersection of the tangent of the fast rising curve of current density and the tangent of the baseline. The chronoamperometry tests were performed for all catalysts at constant value of potential E= 0.65 V for t = 1.5 h. The data processing was performed with EC-Lab software, plots were prepared with Origin 8 Pro software.

2.2.7. Density functional theory calculations

The density functional theory (DFT) is a computational modeling method based on quantum mechanics. In DFT, the ground state properties of electron systems can be described by electron density, instead of wave functions. DFT is based on the assumption, that ground state and other properties of electron systems can be described by electron density, instead wave functions. According to the Hohenberg-Kohn theorem, the external potential $v_{ext}(\mathbf{r})$ is uniquely determined (up to a constant) by the ground state particle density $n_0(\mathbf{r})$ and the functional of the total energy reaches a minimum value for $n_0(\mathbf{r})$. Thus, it can be seen that the ground state particle density determines the Hamiltonian and all states. Therefore, the ground state particle density defines all properties of the system [108,109]. The relationship between the ground state wave function Ψ and the ground state density $n(\mathbf{r})$ of an N-electron system can be written:

$$n_0(\mathbf{r}) = N \int d\mathbf{r}_2 \dots d\mathbf{r}_N \Psi^*(\mathbf{r}, \mathbf{r}_2, \dots, \mathbf{r}_N)\Psi(\mathbf{r}, \mathbf{r}_2, \dots, \mathbf{r}_N) \quad (24)$$

where the spin coordinates are not shown explicitly [110].

In DFT calculations some approximations are used, which not only reasonably predict properties of many systems, but also reduce computational costs. One of these approximations is the local density approximation (LDA), in which it is assumed that the exchange-correlation energy (E_{xc}) in each point of space, where electron density is $n(\mathbf{r})$, is equal to the exchange–correlation energy of the homogeneous electron gas with the same density, $n = n(\mathbf{r})$ [108]. Another type of approximation, is the generalized gradient approximation (GGA) [111], which includes density gradient corrections and higher spatial derivatives of the electron density. In the GGA, exchange–correlation energy depends on electron density and its gradients. In general form for a spin polarized system it can be written as:

$$E_{xc}[n_\uparrow, n_\downarrow] = \int d\mathbf{r}(n_\uparrow, n_\downarrow, \nabla n_\uparrow, \nabla n_\downarrow) \quad (25)$$

GGA is very accurate in the determination of the binding energy of inhomogeneous systems.

In the present study the DFT calculations were performed using the Vienna ab-initio simulation package (VASP) [112], applying the generalized gradient approximation. In the calculations a Monkhorst-Pack [113] mesh of 2 x 1 x 2 k-points and plane wave energy cutoff of 300 eV were used. Spin polarization with the ferromagnetic ordering was included in the calculation. The DFT calculations were used to study the diffusion of the Pt and Rh atoms during the growth of the PtRhNi rhombic dodecahedral nanoparticles and for calculating the cohesive energy required to remove the Ni atoms from the core of the solid nanoparticles in order to obtain nanoframes.

a) Studying of Pt and Rh diffusion

The initial cell consisted of 90 Ni atoms forming six layers with (110) surfaces and vacuum spaces of 14 Å. This model was subjected to relaxation of the lattice parameters and atomic positions. Next, 30 Ni atoms were substituted by 22 Pt and 8 Rh atoms with different positions. The final atomic ratio of Pt:Rh:Ni was 22:8:60, which is in good agreement with the experimental atomic ratio of the obtained PtRhNi nanopolyhedra.

To study the diffusion of the elements during growth of the nanoparticles the following models were considered (Figure 12):

1) Random alloy model, where the Pt, Rh and Ni atoms were randomly mixed in the cell
2) Cluster model, where platinum and rhodium formed separated clusters
3) PtRh surface model, where the two top layers of the cell consisted only of Pt and Rh atoms

4) PtRh sub-surface model, where the third and fourth layer of the cell consisted only of Pt and Rh atoms
5) PtRhNi surface model, where Pt, Rh and Ni atoms formed the first, second, fifth and sixth layer, while the third and fourth layer consisted only of Ni atoms
6) PtRhNi sub-surface model, where Pt, Rh and Ni atoms formed the second, third, fourth and fifth layer, while the first and sixth layer consisted only of Ni atoms

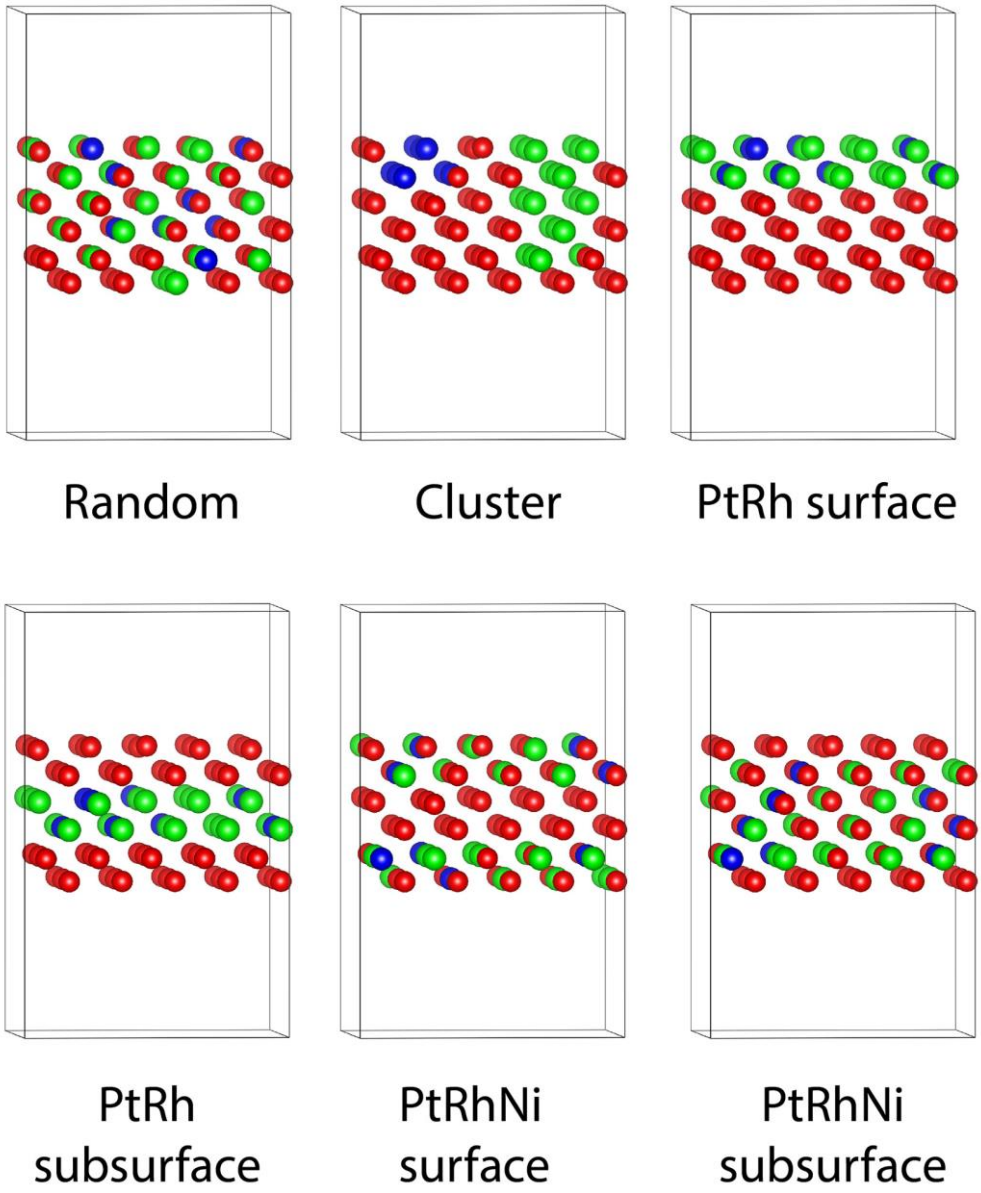

Figure 12. Visualizations of models used in DFT calculations.

To study the diffusion of Pt and Rh atoms in the PtRhNi rhombic dodecahedral nanoparticle, the total energies of the model having Pt and Rh atoms in different positions were calculated. The differences in total energies of the cell containing 90 atoms were compared, the lowest calculated energy was set at 0 eV as a reference.

b) Calculation of the cohesive energy

For the thermodynamic analysis of the etching process of the nanoframes, calculation of the cohesive energy was performed using the equation below:

$$E_{coh} = E_{N-1} + E_M - E_N \quad (26)$$

where E_{coh} is the cohesive energy, E_{N-1} and E_N are the energies of the systems with the number of N-1 and N atoms, respectively, and E_M is the energy of the removed metal atom. To calculate E_N the following models were considered:

1) Ni-model consisting of 90 Ni atoms, which simulates the (110) Ni-face in nanoparticles
2) PtRhNi surface model, where Pt, Rh and Ni atoms formed the first, second, fifth and sixth layer, while the third and fourth layer consisted only of Ni atoms. This model consists of 22 Pt, 8 Rh and 60 Ni atoms and simulates the PtRhNi edges of the nanoparticles

To calculate E_{N-1} the following models were considering:

1) Ni-model consisting 89 Ni atoms – one Ni atom was removed from the surface
2) PtRhNi surface model with removed:
   - One Pt atom from the surface
   - One Rh atom from the surface
   - One Ni atom from the surface

All the calculations parameters were the same as during the simulation of diffusion of the Pt and Rh atoms.

The visualizations of the all above models, as well as the schematic nanoparticle models were generated in the VESTA ver. 3.3.9 software [114].

Chapter 3: Results and discussion

3.1. Thermodynamic and kinetic aspects of solid $PtNi_3$ and PtRhNi rhombic dodecahedral nanoparticles growth

3.1.1. Synthesis of solid $PtNi_3$ and PtRhNi rhombic dodecahedral nanoparticles

Parental phase-segregated solid $PtNi_3$ and PtRhNi nanopolyhedra were synthesized by hot-injection method adapted from the work of the Stamenkovic group [17]. This synthesis method is based on a quick injection of the "cold" metal precursors solution into a hot solvent. Reaching the injection temperature, rapid nucleation occurs and is limited by the injection of "cold" metal precursors, which causes a drop of the solution temperature preventing further nucleation. As a result, the solution contains small amount of nuclei and reduced Pt and Ni or Pt, Rh and Ni floating free atoms. By increasing the temperature, growth of these nuclei to $PtNi_3$ or PtRhNi polyhedra occurs with no additional nucleation [115]. In the series of syntheses performed in this study, oleylamine was used as both, reducing agent and stabilizer [116]. Based on the three different projections of STEM images and comparing them with the 3D models (Figure 13), the shape of the obtained nanoparticles could be identified as rhombic dodecahedral being enclosed by 12 {110} planes. This is due to the fact that oleylamine also acts as a capping agent, which facilitates the growth of the {110} facets of Pt-based alloys [32]. This results in obtaining rhombic dodecahedral $PtNi_3$ nanoparticles, which expose twelve {110} facets.

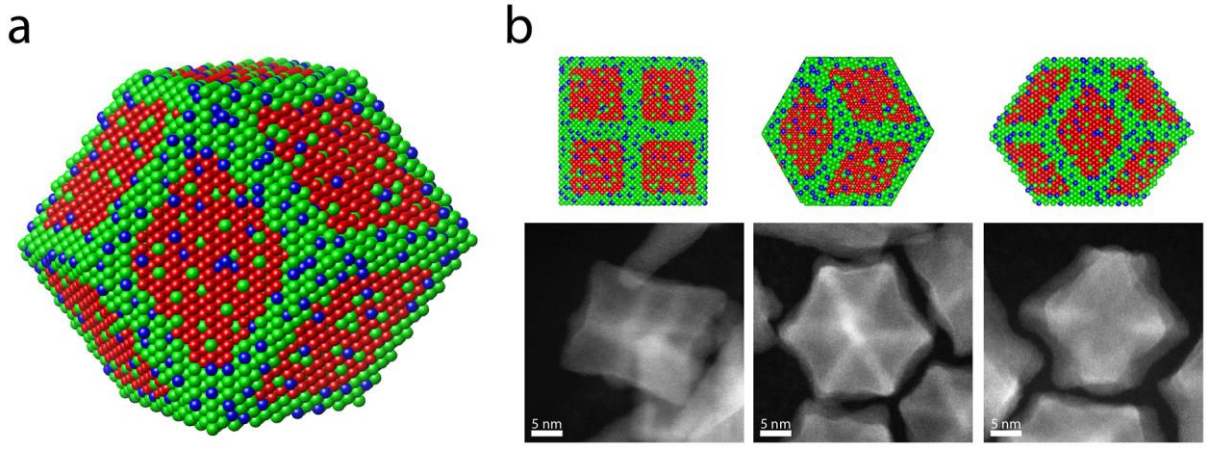

Figure 13. a) Schematic illustration of the PtRhNi solid rhombic dodecahedral nanopolyhedra after synthesis - Pt atoms are depicted in green, Rh in blue, Ni in red; b) models of the three basal projections from three different positions with the corresponding HAADF STEM images. Note that models are not in scale.

As it can be seen on the HAADF STEM overview images, the $PtNi_3$ nanopolyhedra are uniform in shape and size (Figure 14a), while in the PtRhNi nanopolyhedra sample two shapes can be distinguished, i.e. rhombic dodecahedral and more elongated consisting of two pyramids connected by their hexagonal base. However the latter ones constitute only 15% of the total (Figure 14b). This shape deformation is probably caused by presence of rhodium, which has a high surface energy of {110} [49], thus in order to reduce the surface energy, the nanoparticles become elongated in one or two directions. Still, generally the nanoparticles poses a rhombic dodecahedra shape with the PtRhNi phase segregated at the edges and the Ni phase concentrated in the core of nanoparticles.

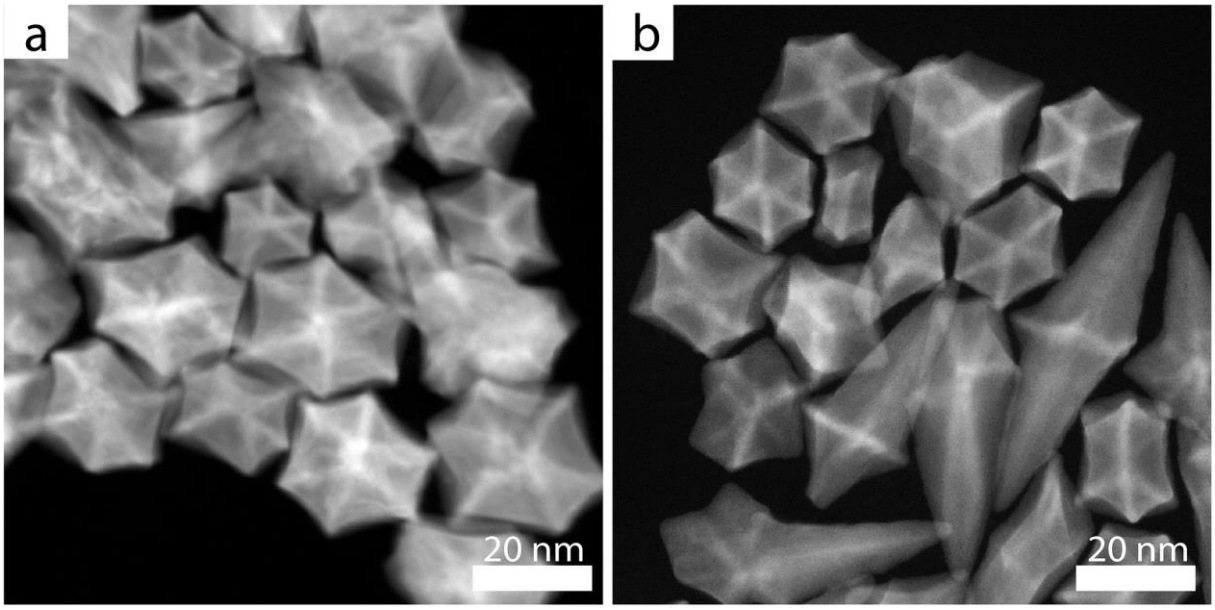

Figure 14. HAADF STEM overview images of a) $PtNi_3$ and b) PtRhNi rhombic dodecahedral nanopolyhedra.

Already on the HAADF STEM overview images (Figure 14) it also can be seen that both $PtNi_3$ and PtRhNi nanopolyhedra exhibit a phase-segregation. Indeed, the HAADF STEM detector allows for a qualitative distinction between elements with various Z-numbers, when the sample thickness is uniform. The higher Z-number areas exhibit a more intensive contrast (bright), compared to areas with lower atomic number. Therefore, the Pt-rich and PtRh-rich edges of the nanopolyhedra are brighter on the STEM images than the Ni-core of the polyhedra. The size of the solid $PtNi_3$ nanopolyhedra, measured on the basis of the STEM images, is between 16 nm – 26 nm, with an average of 20.5±2.3 nm (Figure 15a), while the size of the PtRhNi nanopolyhedra is between 13 – 23 nm with an average of 17.7±2.6 nm (Figure 15b).

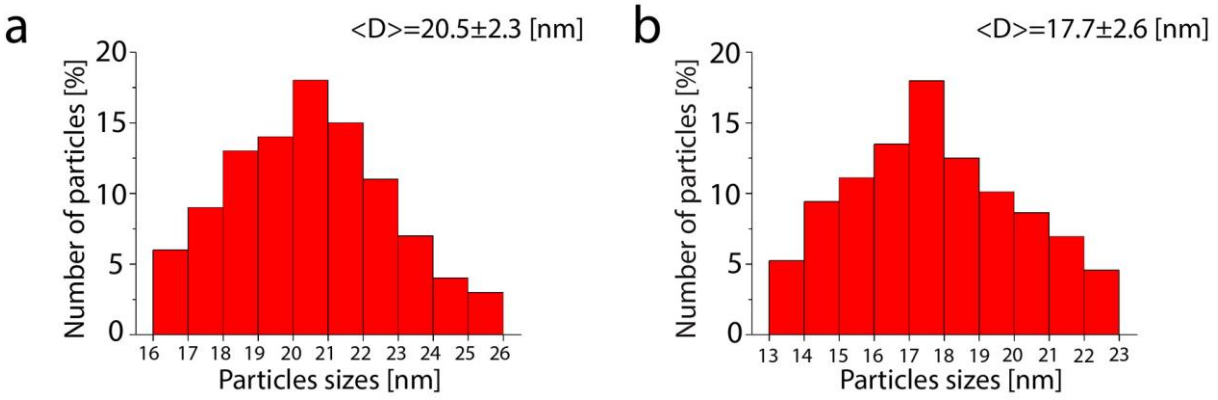

Figure 15. Size distribution of the a) $PtNi_3$ and b) PtRhNi rhombic dodecahedral nanopolyhedra.

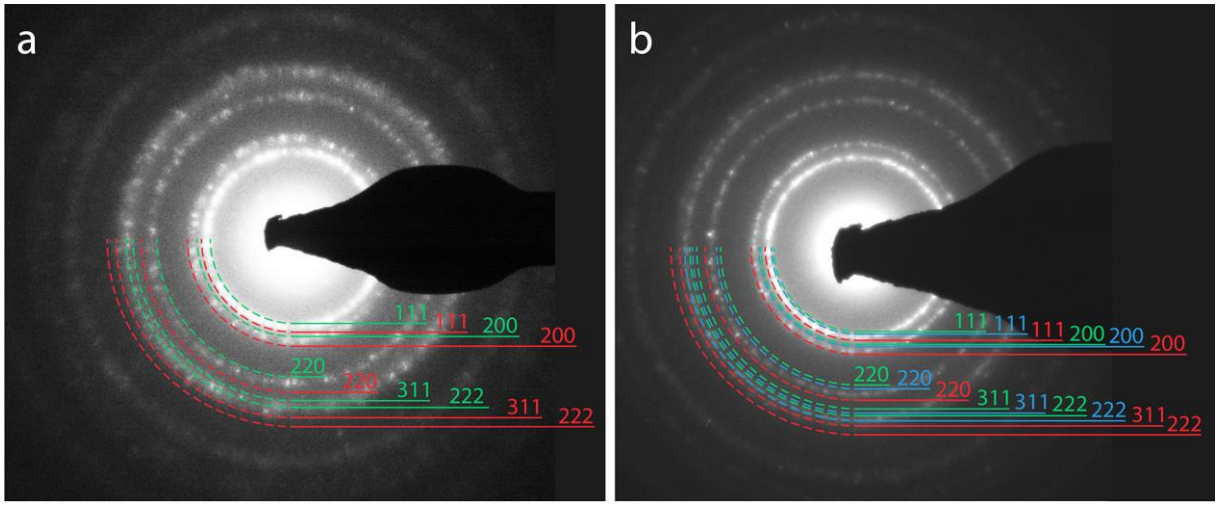

Figure 16. Selected area electron diffraction patterns of a) $PtNi_3$ and b) PtRhNi rhombic dodecahedral nanopolyhedra. Pt planes are indexed with green lines, Rh with blue lines and Ni with red lines.

The selected area electron diffraction patterns (Figure 16) confirm the crystalline structure of the nanoparticles. The diffraction rings, were indexed with the {111}, {200}, {220}, {222} and {311} planes of Pt and Ni for $PtNi_3$ nanopolyhedra (Figure 16a) and {111}, {200}, {220}, {222} and {311} planes of Pt, Rh and Ni for PtRhNi nanopolyhedra (Figure 16b). Indeed, the observed rings are located between the indexed arcs, therefore it is assumed that Pt and Ni in $PtNi_3$ and Pt, Rh and Ni in PtRhNi form an alloy phase in the nanoparticles. It is similar in the case of XRD diffractograms (Figure 17), where the diffraction peaks are located between peaks identified as {111}, {200}, {220} face-centered cubic (fcc) platinum and fcc nickel for the $PtNi_3$ sample, and fcc platinum, fcc rhodium and fcc nickel in PtRhNi samples. This suggests the formation of a nanoalloy phase of these metals in the nanopolyhedra. However, the slight asymmetry of peaks suggests a simultaneous occurrence of phase segregation in the PtNi and PtRhNi alloys [117], which results from presence of two phases: Ni-core and PtNi-edges or Ni-core and PtRhNi-edges.

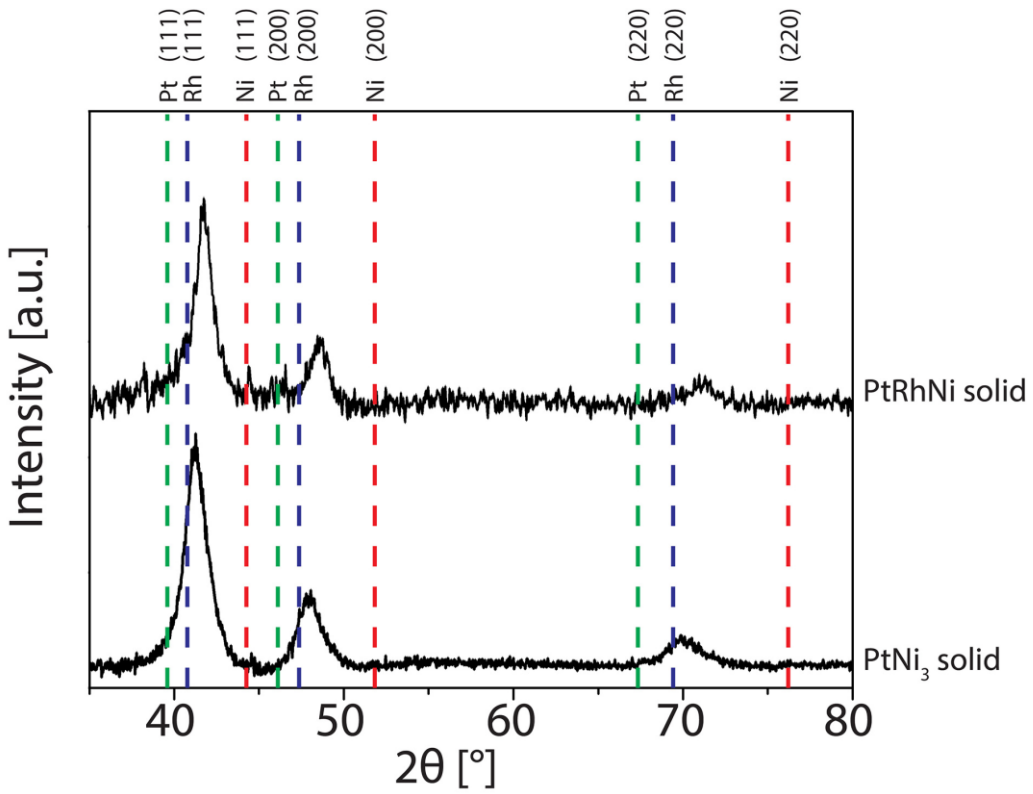

Figure 17. XRD diffractograms of $PtNi_3$ (lower pattern) and PtRhNi nanopolyhedra (upper pattern). The standard reflexes for pure Pt – green, Rh - blue and Ni – red are marked for comparison.

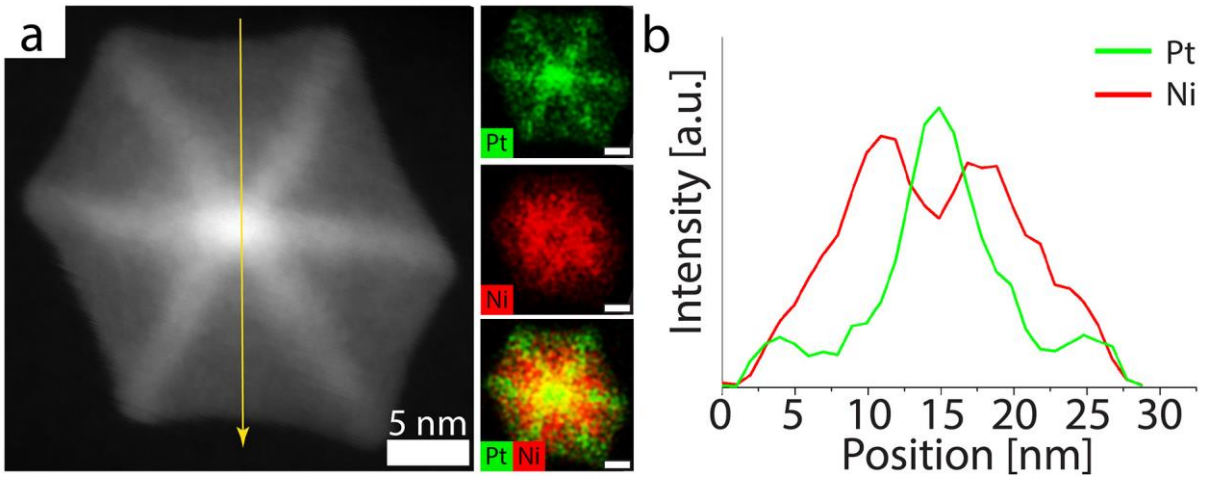

Figure 18. a) HAADF STEM image of a single $PtNi_3$ nanopolyhedron with corresponding EDS maps; b) EDS line-scan taken along the line marked in a).

EDS elemental mapping and EDS line-scan through the nanopolyhedra confirm the previous observation that the $PtNi_3$ rhombic dodecahedral nanoparticles consist of a Ni-core and PtNi-edges (Figure 18), while PtRhNi nanopolyhedra are composed of a Ni-core and PtRhNi-edges (Figure 19). In particular, EDS line-scans show that the signal from Ni is strong in the entire nanoparticle, while the signal from Pt and Rh is concentrated at the edges of the nanopolyhedra.

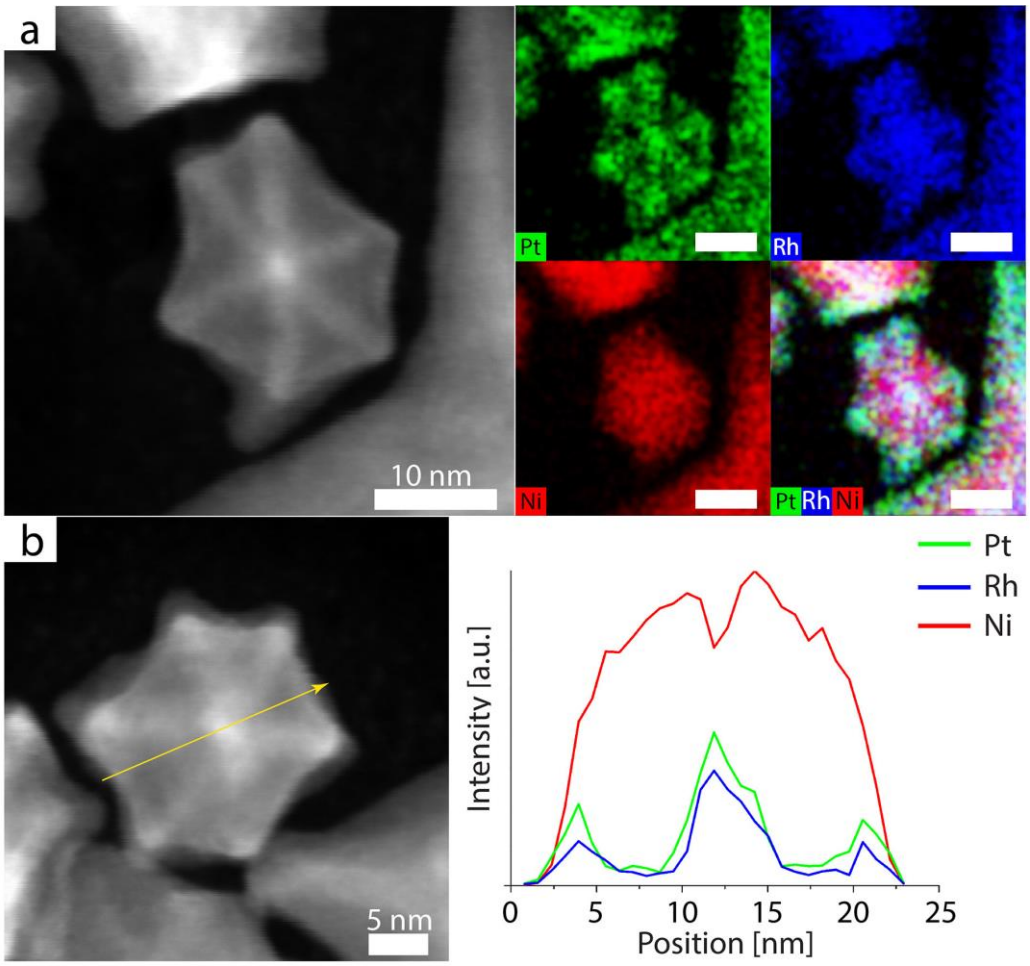

Figure 19. a) HAADF STEM image of a single PtRhNi nanopolyhedron with the corresponding EDS maps; b) HAADF STEM image with the corresponding EDS line-scan through the nanoparticle.

The EDS maps were semi-quantitatively analyzed to obtain the atomic ratio of the elements in both samples, and the results were compared with the atomic ratio obtained by the ICP-OES measurements (Table 2). Based on these results, the Pt:Ni and Pt:Rh:Ni atomic ratio can be estimated to 1:3 and 3:1:7, respectively. This ratio corresponds to $PtNi_3$ and $Pt_3Rh_1Ni_6$, however to simplify, the $Pt_3Rh_1Ni_6$ will be referred as PtRhNi in further text.

Table 2. Comparison of atomic composition of $PtNi_3$ and PtRhNi nanopolyhedra obtained by quantified EDS maps and ICP-OES measurements.

	Atomic %			
	EDS		**ICP-OES**	
	$PtNi_3$	**PtRhNi**	**$PtNi_3$**	**PtRhNi**
Pt	26	30	28	28
Rh	-	9	-	9
Ni	74	61	72	62

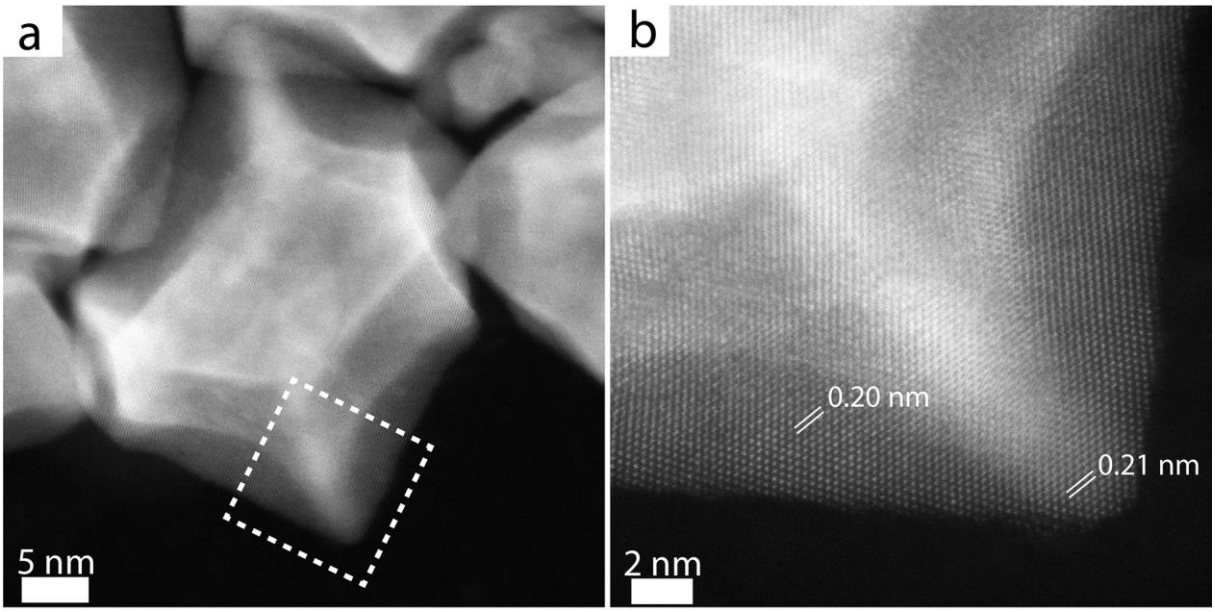

Figure 20. a) High-resolution HAADF STEM image of the $PtNi_3$ nanopolyhedron; b) magnified area marked in a) with the measured lattice distances on the edge of a nanoparticle and on the facet.

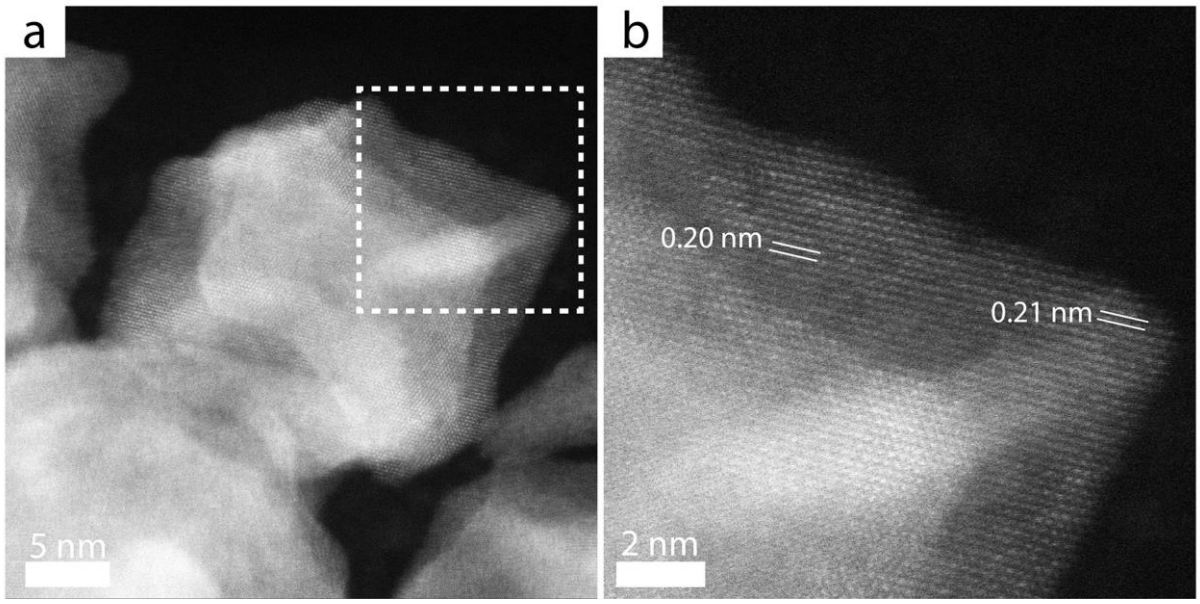

Figure 21. a) High-resolution HAADF STEM image of the PtRhNi nanopolyhedron; b) magnified area marked in a) with measured lattice distances on the edge and on the facet of a nanoparticle.

High-resolution HAADF STEM images of $PtNi_3$ (Figure 20) and PtRhNi (Figure 21) samples confirm the crystallinity of the obtained nanopolyhedra. The measured lattice distances on the edges and on the faces of the nanopolyhedra (0.21 nm and 0.20 nm, respectively) correspond to (111) planes of PtNi and PtRhNi alloys. However, the measured lattice distances are smaller than those of pure fcc Pt (111) planes and of pure fcc Rh (111) planes and are bigger than on pure fcc Ni (111). This indicates the formation of a PtNi or a PtRhNi alloy at the edges and facets of the nanopolyhedra. However, the lattice distances at

faces of both $PtNi_3$ and PtRhNi are smaller than the lattice distance at the edges, thus it suggests that edges are Pt-rich and face are Ni-rich, which confirm previous EDS observations.

In order to investigate the formation mechanism of PtRhNi nanopolyhedra, control experiments were performed in which during synthesis nanoparticles were sampled at different temperatures (from 210°C to 270°C with 15°C steps).

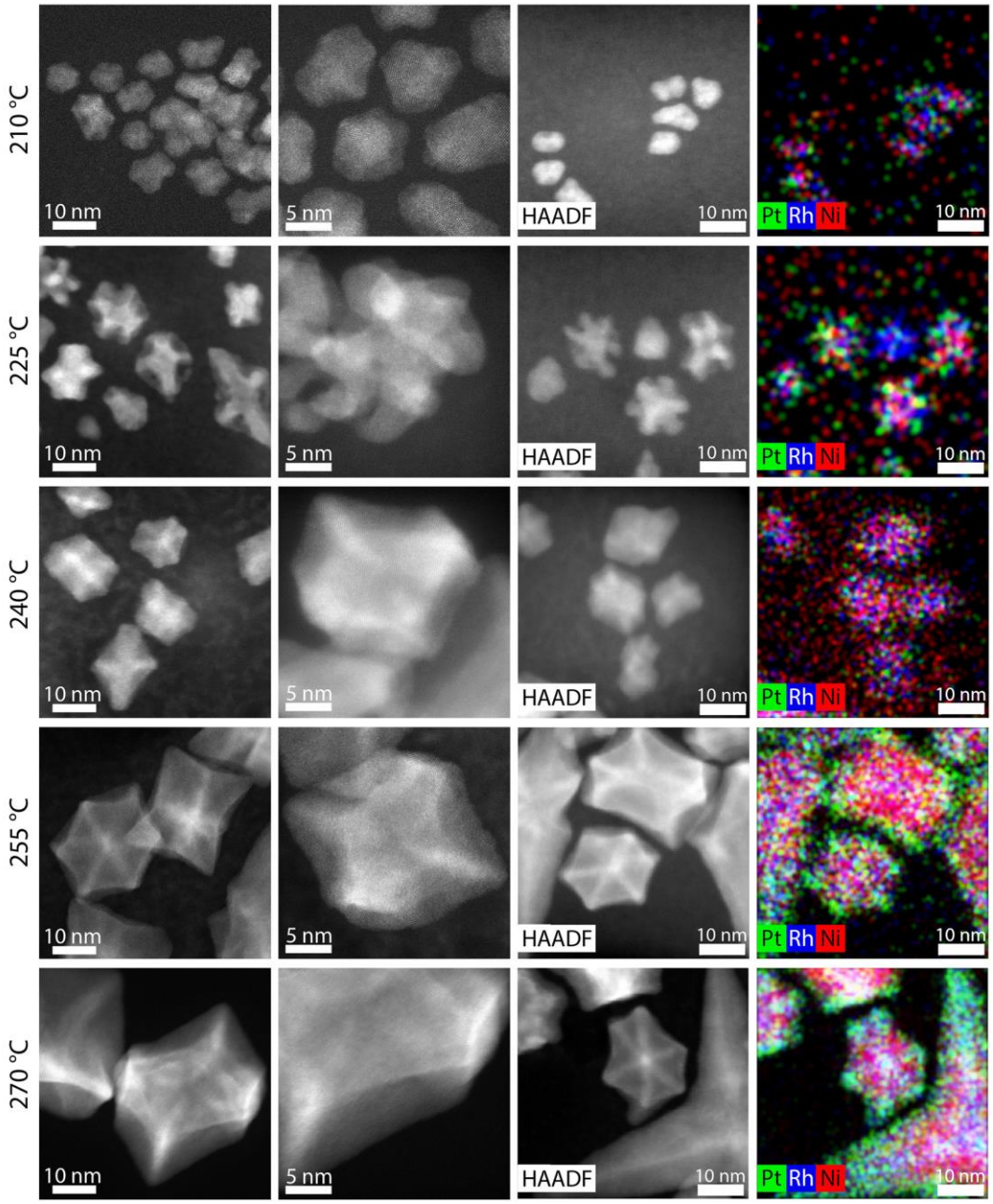

Figure 22. STEM HAADF images and EDS maps of the intermediate products obtained during PtRhNi solid nanopolyhedra synthesis.

HAADF STEM images and EDS maps (Figure 22) reveal that at 210°C small (about 5 nm) polyhedral nanoparticles are formed with no phase segregation – Pt, Rh and Ni are uniformly

distributed within the entire nanoparticle. As the temperature increases to 225°C, the nanoparticles grow and the polyhedral nanoparticles transform into branched structures with branches composed mainly of platinum and rhodium. This transformation is possible due to the diffusion of these elements from the core of the nanoparticles to their outside [118] and a simultaneous constant deposition of freshly reduced Pt and Rh atoms originating from the precursors. During further increase of the temperature to 240°C the nanoparticles change their shape from branched to rhombic dodecahedral due to the deposition of nickel atoms on the nanoparticles and filling the space between the PtRh dendrites in order to minimize the surface energy, which results in obtaining a polyhedral shape close to rhombic dodecahedral. HAADF STEM images show that the edges are slightly brighter than the center of the nanoparticles, which could indicate PtRh phase-segregation at the edges, nevertheless the EDS map shows that Pt, Rh and Ni are still uniformly mixed. At 255°C rhombic dodecahedral nanoparticles are still growing, however the presence of PtRh-rich edges is confirmed by both HAADF STEM images and EDS maps, which suggest that the diffusion of Pt and Rh from the core to edges still occurs. Interestingly, at this temperature not all rhodium diffuses towards the edges, but it is also present in the core of the nanoparticles, which indicates that rhodium diffuses slower than platinum. After increasing the temperature to 270°C, both, platinum and rhodium are only at the edges and not in the core, which is confirmed by HAADF STEM images and EDS maps. Generally, with increasing the temperature to above 250°C, Pt and Rh diffusion into the edges is still in progress until the nanoparticles have a rhombic dodecahedron shape with a phase segregation at the edges. Interestingly, the platinum diffusion from the core to the edges of the nanoparticles occurs despite the fact that platinum has a higher surface energy for {110} facets than nickel (2.82 J m^{-2} vs. 2.37 J m^{-2}, respectively [57]). This phenomenon was investigated by other groups [118,119] and was explained by the reduction of the internal strain caused by the bigger atomic radius of Pt than the one of Ni (1.39Å and 1.24Å, respectively [120]). However, in the studied nanoparticles, there are additionally rhodium atoms, which also diffuse from the core to the edges. This can be explained, similarly as in the case of platinum, although rhodium has the highest surface energy among all the three elements (2.90 J m^{-2} [57]), and a smaller atomic radius than platinum, but bigger than nickel (1.34 Å [120]). Generally, in multimetallic systems, the element with lower surface energy and bigger atomic radius, tends to diffuse to the surface [121]. Rhodium has a higher surface energy than nickel, but due to its bigger atomic radius it is pushed to the surface. However, because Rh has higher surface energy than Pt and slightly smaller atomic radius, it diffuses slower than Pt. It is worth noticing that during

synthesis, except Pt and Rh diffusion, a constant deposition of Pt, Rh and Ni also occurs. This causes an increase of the size of the synthesized nanopolyhedra.

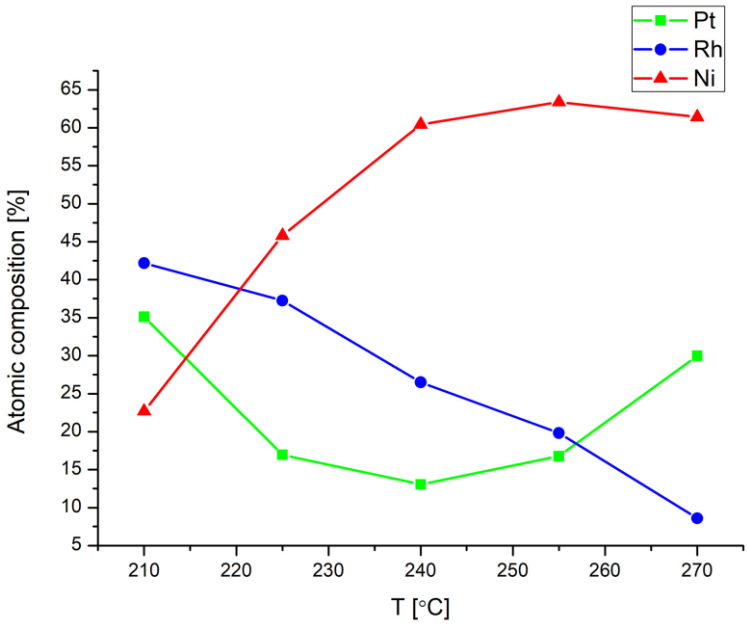

Figure 23. The composition plot of growth process of the PtRhNi rhombic dodecahedral nanopolyhedra.

The results of the chemical analysis performed during synthesis are also interesting. Based on EDS measurements (Figure 23) it can be seen, that initially (at 210°C) the nanoparticles are composed mainly of Pt and Rh. This can be explained by the fact that rhodium and platinum have a high reduction potential (0.758 V vs. SHE and 0.755 V vs. SHE, respectively), while nickel has a low reduction potential (–0.257 V vs. SHE) [122]. It is generally known that compounds with higher reduction potential are reduced faster [123], therefore in this case platinum and rhodium are reduced before nickel, which explains the excess of these two elements in the initial nanoparticles. Due to the relatively low concentration of rhodium in the reaction solution, its atomic ratio decreases during synthesis. On the other hand, the nickel content in the nanoparticles increases during the synthesis, due to the fact that it is reduced later than Pt and Rh. Interestingly, the platinum content in the nanoparticles during synthesis is initially high, next it decreases and then increases again. This can be explained as follows: the rhodium precursor has a relatively low concentration in the reaction solution and it was all used to generate the nanoparticles seeds. On the other hand, the platinum precursor has a higher concentration than rhodium, therefore the generation of nanoparticles seeds, does not use all the Pt atoms, they are still in the reaction solution. These Pt atoms, during the growth of nanoparticles, are deposited on the nanopolyhedra edges, justifying the increase of the platinum content measured by EDS.

To better understand the causes of the process of platinum and rhodium surface segregation occurring during the synthesis of PtRhNi nanopolyhedra DFT calculations were performed (Figure 24).

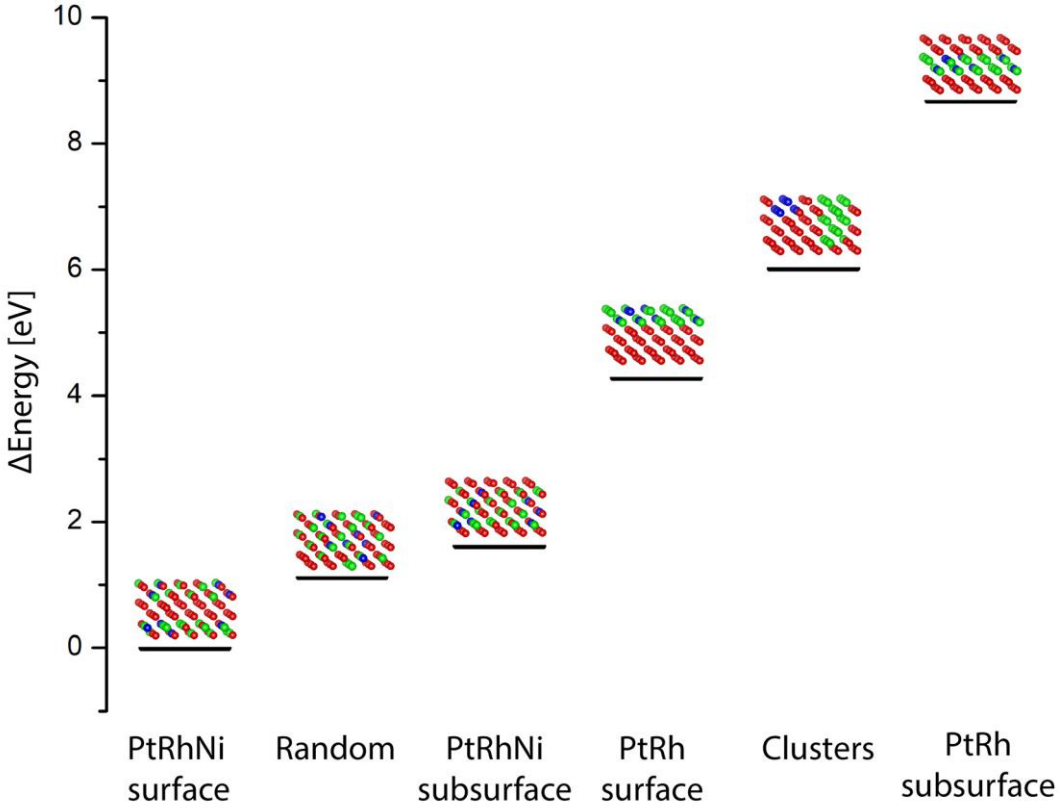

Figure 24. Comparison of differences in total energy calculated by DFT methods.

Six different models of the PtRhNi (110) surface were considered, all calculated energies are summarized in Table 3. The DFT experiments confirmed, that despite the high surface energy of platinum and rhodium, the total energy of the PtRhNi system with Pt, Rh and Ni segregation on the surface and Ni in the subsurface (model "PtRhNi surface") is the lowest compared to the other tested systems. The highest total energy has the system, in which Pt and Rh atoms are inside the cell, while nickel atoms form the surfaces (model "PtRh subsurface", ΔE= 8,68 eV). This atom arrangement causes lattice strain and as a consequence higher total energy. However, this model can be considered as an initial state of the growth of the nanoparticles, where Pt and Rh did not start to diffuse yet. Next, Pt and Rh diffuse outwards, forming a structure presented in the model "PtRhNi subsurface", which has a lower total energy (ΔE= 1.62 eV) due to the mixing of Pt, Rh and Ni. Finally, platinum, rhodium and some nickel atoms are arranged on the surface, while the rest of the nickel atoms are at the subsurface (model "PtRhNi surface"). This system has the lowest total energy (ΔE= 0 eV), due to the reduction of the internal strain caused by the differences in atomic radii. Based on

the DFT results, it also can be concluded, that the most energetically favorable is the mixing of Pt and Rh with Ni at the surface. The system with only Pt and Rh on surface, and nickel in subsurfaces (model "PtRh surface") has a significantly higher total energy than the "PtRhNi surface" model (ΔE= 4.29 eV). The possible explanation of this phenomenon is the lattice mismatch between Pt, Rh and Ni (3.92 Å, 3.80 Å and 3.52 Å, respectively [57]), which hinders the deposition and growth of the PtRh layers on Ni layers due to the increase of strain energy [37]. Moreover, based on the "Clusters model", it can be seen that the separation of the Pt and Rh clusters on the surfaces, caused an increase of the total energy (ΔE= 6.09 eV), which can indicate that mixing of platinum and rhodium is energetically favorable, whereas formation of separated phases is less likely. These results show that the phase segregation occurring during growth of the rhombic dodecahedral PtRhNi nanoparticles is thermodynamically favorable. DFT calculations were performed for PtRhNi system, however these results can also be applied for growth of PtNi phase segregated nanoparticles.

Table 3. Exact values of differences in total energy calculated by DFT methods.

Model	**ΔE (eV)**
PtRhNi Surface	0
Random	1.13
PtRhNi Subsurface	1.62
PtRh Surface	4.29
Clusters	6.02
PtRh Subsurface	8.68

3.1.2. Control experiments revealing the influence of synthesis parameters on the nanoparticles morphology and composition

To better illustrate the kinetics of the synthesis reaction of the $PtNi_3$ and PtRhNi rhombic dodecahedral nanoparticles, control experiments were performed. In the first experiments, the investigation of the impact of precursors adding rate and temperature during their addition were verified.

a) Precursors adding rate and temperature during their addition

Two syntheses were performed, in which the metal precursors (chloroplatinic acid and nickel(II) nitrate) were added to oleylamine at 160°C in two (synthesis 1, Figure 25a, b) and three portions (synthesis 2, Figure 25c, d), respectively, at 1 minute intervals. In both cases bimetallic overgrown rhombic dodecahedron nanoparticles were obtained, but with slightly different morphology. Nanoparticles from synthesis 1 (with an average diameter

of 20.9 ± 1.9 nm) are significantly smaller than those from synthesis 2 (average size 44.6 ± 8.2 nm), and also have a narrower size distribution (16-26 nm versus 21-63 nm). The difference also occurs in dendrites, nanoparticles from synthesis 1 have mostly sharp and straight dendrites, while nanoparticles from synthesis 2 have more rounded and more developed "branches". However, in both cases the dendrites grow anisotropically from the vertex of the nanopolyhedra.

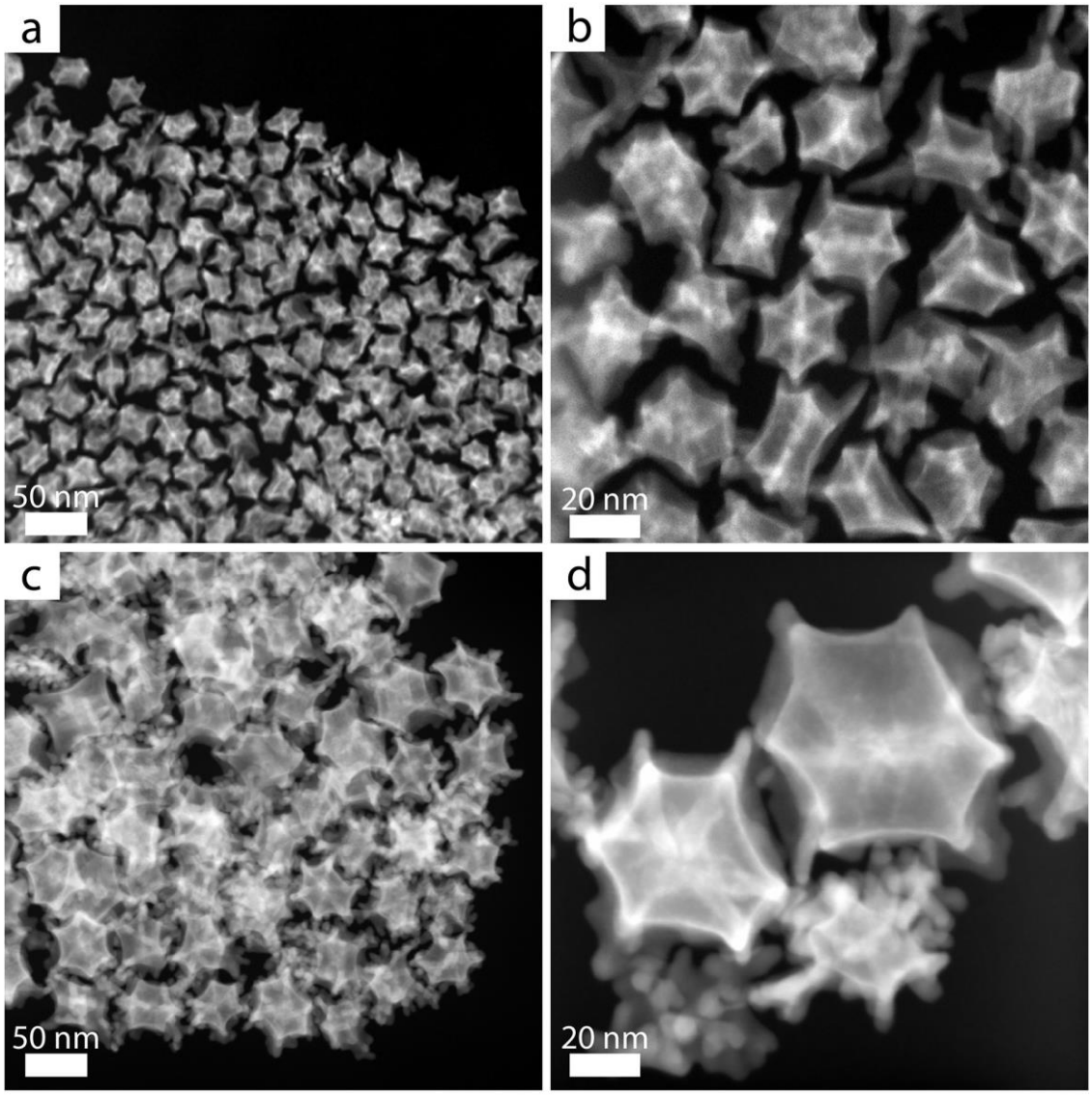

Figure 25. HAADF STEM images of the overgrown PtNi NPs obtained in syntheses with different rates of adding precursors. (a, b) Precursors were injected in two portions (synthesis 1), and (c, d) three portions (synthesis 2).

High-resolution TEM images (Figure 26) revealed that the branches have a crystalline structure with visible lattice fringes having a distance between them d = 0.23 nm, which corresponds to fcc platinum (111) planes. EDS elemental maps (Figure 28a, b) confirm that

the dendrites in nanoparticles from both syntheses are pure platinum. Moreover, similarly like in the case of phase-segregated nanopolyhedra, there is a nickel core inside the nanoparticles, but platinum is not only located at the edges and dendrites, but is also present, in small quantities, on the facets of the nanopolyhedra. Based on the EDS measurements, the atomic composition of the overgrown nanoparticles from synthesis 1 and 2 was evaluated to be $Pt_{44}Ni_{56}$ and $Pt_{51}Ni_{49}$, respectively.

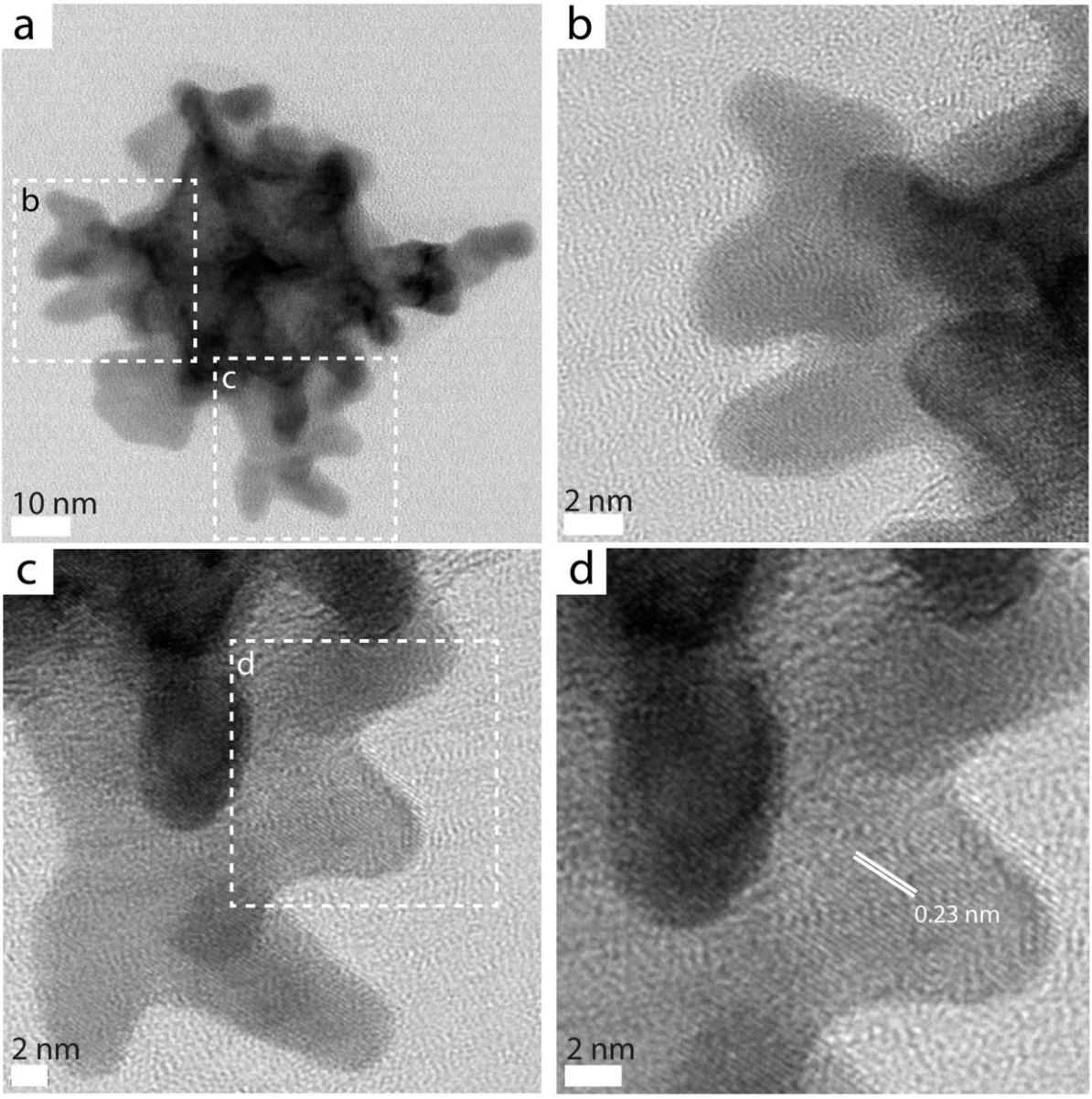

Figure 26. a) HRTEM image of the overgrown PtNi nanoparticles from Synthesis 2; b), c), d) HRTEM images of the dendrites taken from areas marked in (a) and (c).

In another experiment, the metal precursors were added to the oleylamine solution at 40°C (synthesis 3), which resulted in obtaining nanoparticles with various shapes (Figure 27a) with an average diameter of 30.3 ± 8.8 nm. Some of the nanoparticles have shapes close to

polyhedral, but the rest of them have an undefined shape (Figure 27b). The EDS elemental mapping (Figure 28c) shows that the nanoparticles from synthesis 3 have a core-shell structure with a Ni-core and a Pt-shell. The atomic elemental composition of these nanoparticles calculated from EDS is $Pt_{53}Ni_{47}$.

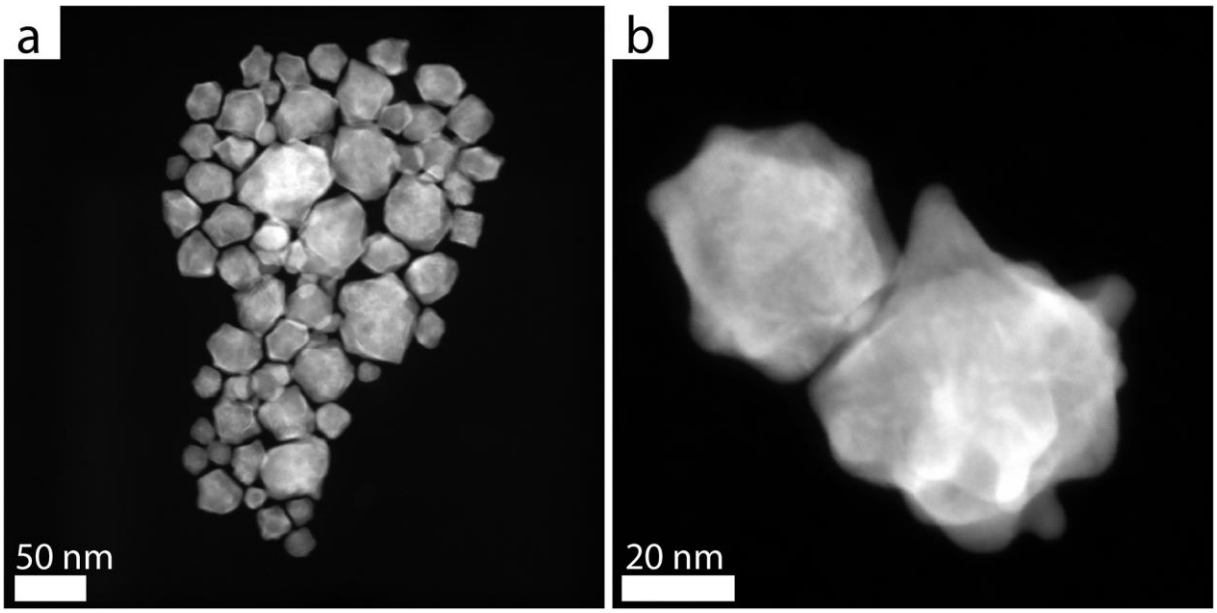

Figure 27. HAADF STEM images of PtNi core-shell nanoparticles obtained from the synthesis with precursors added at low temperature.

These results show that the syntheses of the $PtNi_3$ nanopolyhedra are very sensitive to parameter changes allowing to obtain nanoparticles, which differ in morphology. Other groups have investigated the effect of metal precursors concentration [124] and reaction time [118]. However, in the present study the impact of metal precursors addition rate, and the temperature at which the precursors are added on the morphology of the obtained nanoparticles were investigated. When metal precursors are added to oleylamine in two or three portions, overgrown PtNi nanopolyhedra are obtained, which could be explained by the reaction kinetics. The effects of the first injection are the same as in the case of standard hot-injection method, the solution contains PtNi nuclei and free Pt and Ni atoms. As a result of the second and third injection, Pt and Ni precursors are reduced, but no additional nucleation occurs, due to the drop of the temperature below 160°C. Consequently, the solution contains a certain number of PtNi nuclei resulting from first injection and a large quantity of reduced Pt and Ni atoms resulting from first, second and third injection. This causes an excess of free Pt and Ni atoms in respect to PtNi nuclei, which is a condition for the creation of overgrown nanostructures [125]. After the final injection, the temperature increases and the PtNi nuclei grow by Ni deposition and Pt diffusion from the core to the

edges, similarly like in the case of the one injection method. However, due to the excess of free Pt atoms in the solution, they are deposited on corners of the growing nanoparticles and forming overgrown dendrites.

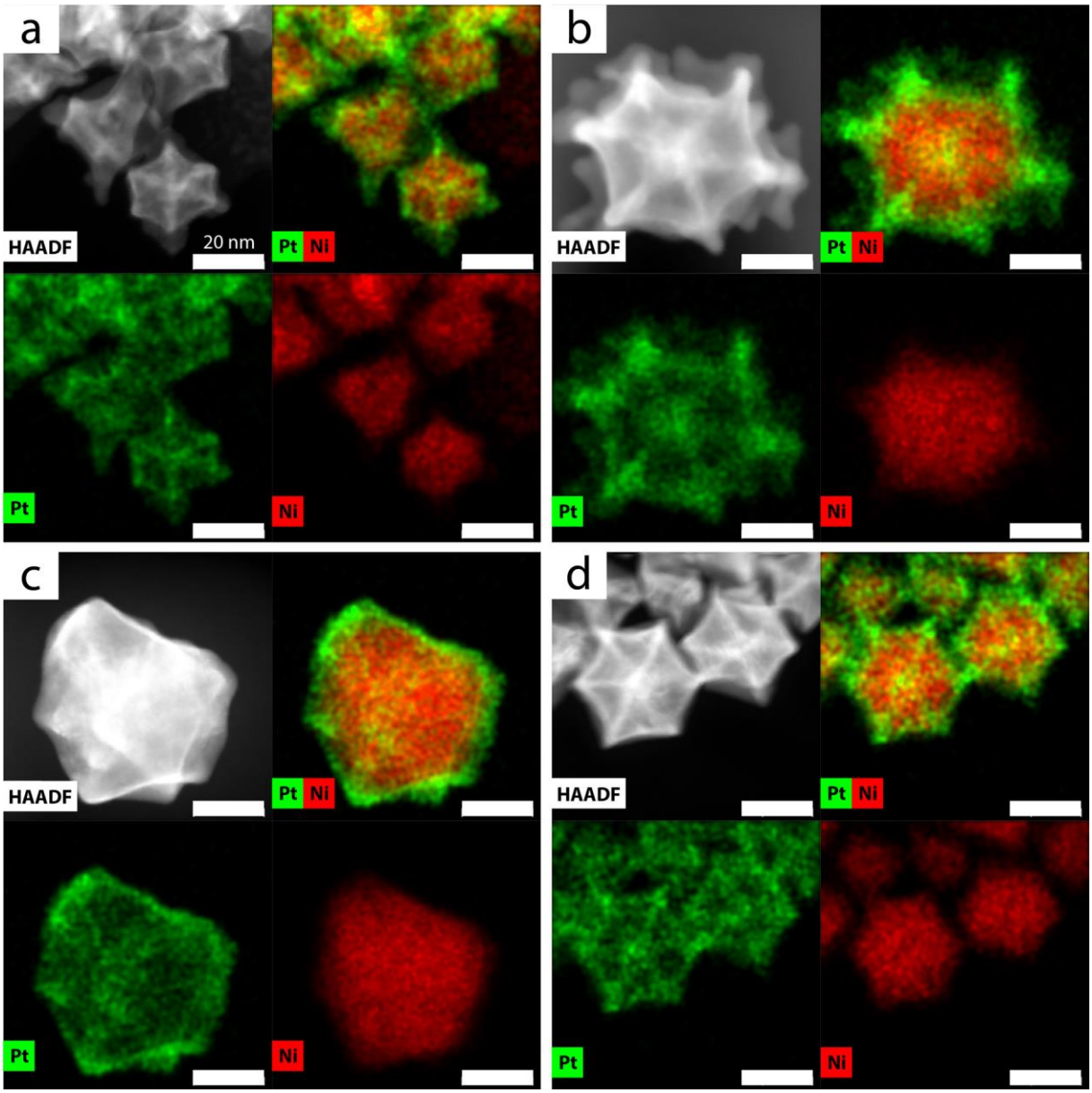

Figure 28. HAADF STEM images with the corresponding EDS elemental maps (Pt – green, Ni – red) and overlaps (Pt+Ni) for a) and b) overgrown PtNi nanoparticles; c) core-shell PtNi NPs and d) surface-segregated rhombic dodecahedral nanopolyhedra. The scale bars are equal to 20 nm.

The growth of the nanoparticles is kinetics depended and could be described by the velocity of deposition ($v_{deposition}$) and velocity of surface diffusion of atoms ($v_{diffusion}$). When $v_{deposition} \approx v_{diffusion}$ (Figure 29a), then the Pt atoms are deposited on the corners of the nanoparticles, due to fact that they are low coordination sites with a high energy [126], and diffuse to the edges forming a core-frame structure, or they diffuse to the facets resulting in a core-shell structure

[57]. When $v_{deposition} > v_{diffusion}$ (Figure 29b), then overgrowth occurs [127,128], due to the rapid deposition and accumulation of platinum atoms at the corners of the nanoparticles. Due to the fact that $v_{diffusion}$ is slower, only part of the deposited platinum atoms can diffuse to the facets of the nanoparticles forming a thin Pt-layer on the nanopolyhedra. Higher values of $v_{deposition}$ than $v_{diffusion}$ results from the excess of platinum atoms in the solution, according to the collision theory: the more atoms are in solution, the faster they are deposited on the growing nanoparticles. The formation of the core-shell nanoparticles can be explained similarly. In this case $v_{deposition} < v_{diffusion}$ (Figure 29c), due to the lower concentration of free Pt and Ni atoms in the solution. Therefore Pt atoms have time to diffuse from the corners to the facets and form a Pt-shell on the Ni-core.

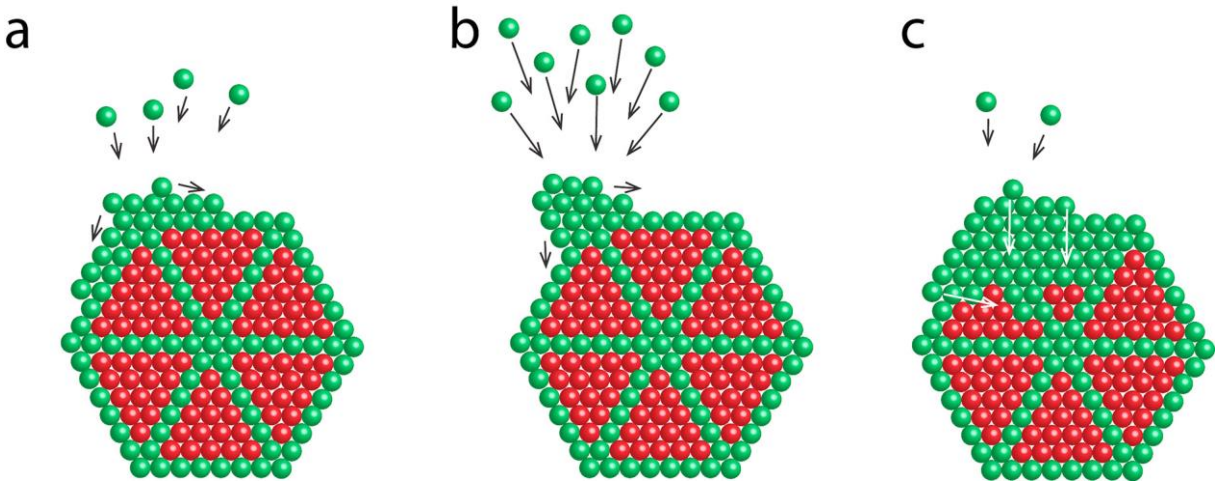

Figure 29. Schematic illustration of the growth process of the $PtNi_3$ nanopolyhedra with a) $v_{deposition} \approx v_{diffusion}$; b) $v_{deposition} > v_{diffusion}$; c) $v_{deposition} < v_{diffusion}$. Note that the models are not in scale.

b) Replacing inert Ar atmosphere by air during synthesis

Another synthesis was performed to verify the role of the inert atmosphere during the growth of the nanoparticles. In this control experiment, the synthesis was performed in air instead of Ar atmosphere (synthesis 4). The obtained nanoparticles (Figure 30), with average size of 126 ± 25 nm, were bigger compared to the rhombic dodecahedral nanopolyhedra synthesized under inert argon atmosphere. Moreover, they have a shape close to hexagonal and porous structure. The EDS maps reveal that platinum and nickel are alloyed throughout the whole nanoparticle. The formation of the pores could be explained by the occurrence of oxidative etching of the nickel atoms during the growth of the nanoparticles. The oxygen from the air, especially in combination with halide ions (e. g. Cl^-, I^-, F^-), is a strong etching agent, which can corrode metals [127,129]. In this case, the oxygen from air coupled with Cl^-

ions originating from the chloroplatinic acid (Pt precursor), etch away the nickel from the growing nanoparticles, resulting in obtaining porous nanoparticles with different morphology than solid rhombic dodecahedral nanoparticles. This approach is often used in obtaining porous bimetallic nanoparticles [130].

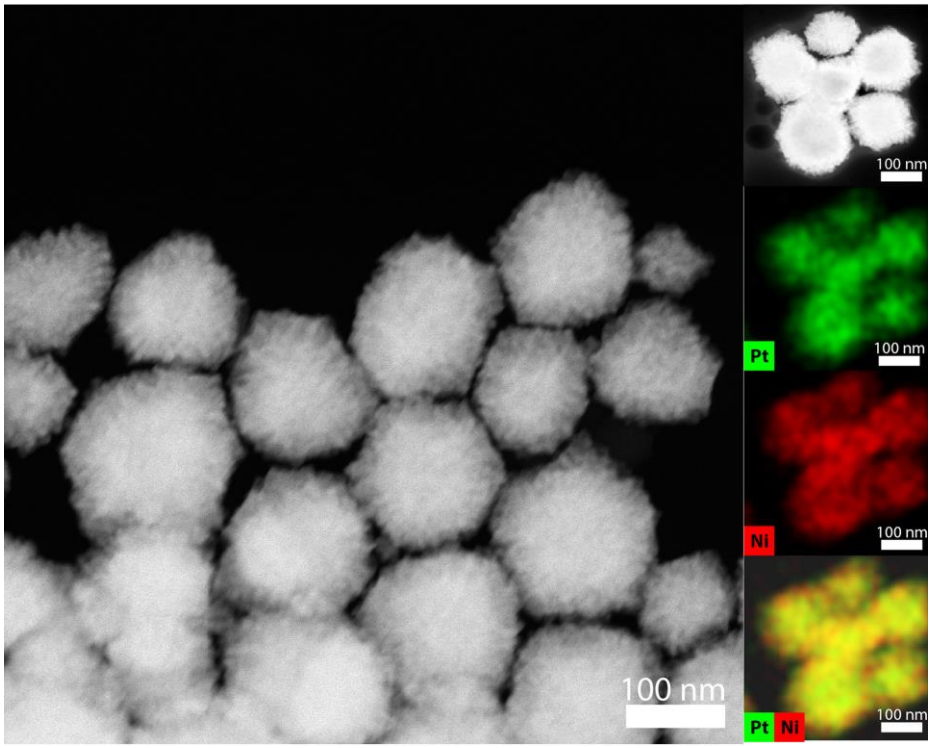

Figure 30. HAADF STEM overview image and EDS elemental maps of PtNi nanoparticles synthesized in air atmosphere.

c) Synthesis in the absence of the Pt precursor

To verify the role of platinum in the synthesis of rhombic dodecahedral nanopolyhedra, a control experiment was conducted, in which the synthesis was performed in the absence of the Pt precursor (synthesis 5). As a result, small (~ 10 nm) crystalline RhNi nanoparticles were obtained (Figure 31a, b). As it can be seen on EDS elemental maps (Figure 31c), rhodium and nickel are uniformly distributed in the obtained nanoparticles, nevertheless in some cases nickel or rhodium dominate the individual nanoparticles. The atomic ratio of Rh:Ni, estimated based on the EDS mappings, is 62:38, which corresponds to Rh_3Ni_2. These results indicate that the presence of platinum is necessary in the synthesis of PtRhNi rhombic dodecahedra nanoparticles. This can be caused by the low reduction potential of nickel (-0.257 V vs. SHE) making it difficult to reduce. Platinum facilitates the reduction of nickel and formation of PtRhNi nanoparticles. Indeed, it is well known,

that reduction of 3d transition metals, such as nickel, is enhanced by presence of noble metal seeds [131,132].

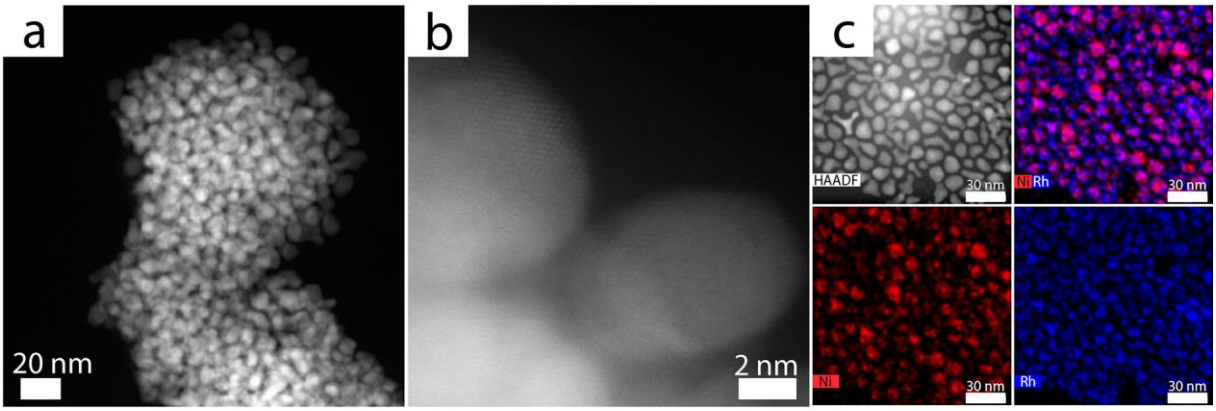

Figure 31. a) STEM HAADF overview image; b) HRSTEM images of RhNi nanoparticles; c) STEM HAADF image with the corresponding EDS elemental maps of Rh and Ni distribution in the NPs.

d) Influence of heating rate increase

Another control experiment was performed to verify the role of changing the rate of temperature increase during the synthesis (synthesis 6).

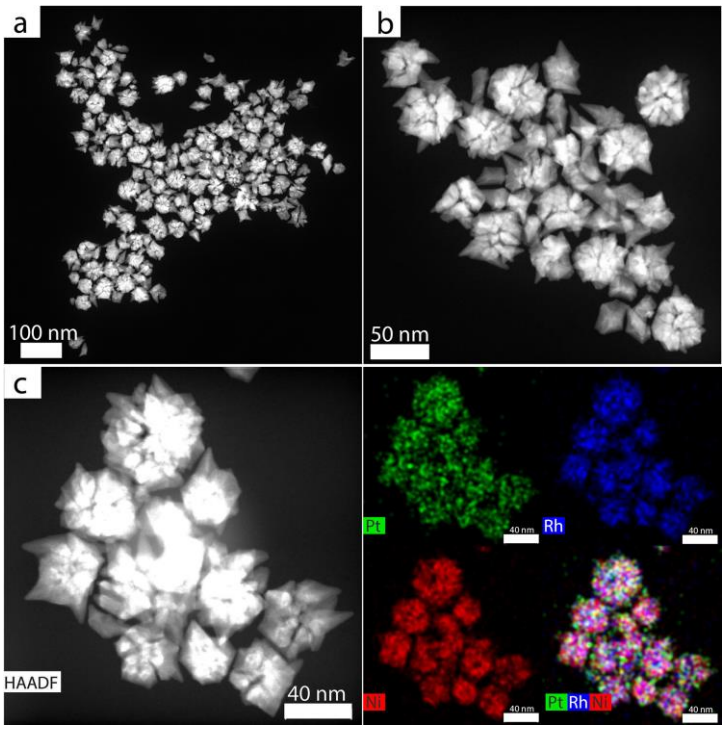

Figure 32. a, b) STEM HAADF images of PtRhNi overgrown nanoparticles; c) STEM HAADF image with corresponding EDS elemental maps.

After increasing the heating rate from 3°C/min to 8°C/min, mostly overgrown PtRhNi nanoparticles were obtained (Figure 32a, b), however some rhombic dodecahedral

nanoparticles are still visible in the sample. It is worth noticing that overgrown nanoparticles are much larger than rhombic dodecahedral NPs (45 nm vs. 18 nm). EDS elemental maps (Figure 32c) show that the synthesized nanoparticles are indeed composed of platinum, rhodium and nickel, nevertheless no phase-segregation occurs, all elements are uniformly distributed forming a nanoalloy.

3.2. Acidic etching of $PtNi_3$ and PtRhNi nanopolyhedra into hollow nanoframes and assembly of SnO_2@Pt_3Ni and SnO_2@PtRhNi heteroaggregates

3.2.1. Obtaining hollow Pt_3Ni and PtRhNi nanoframes by Ni-etching

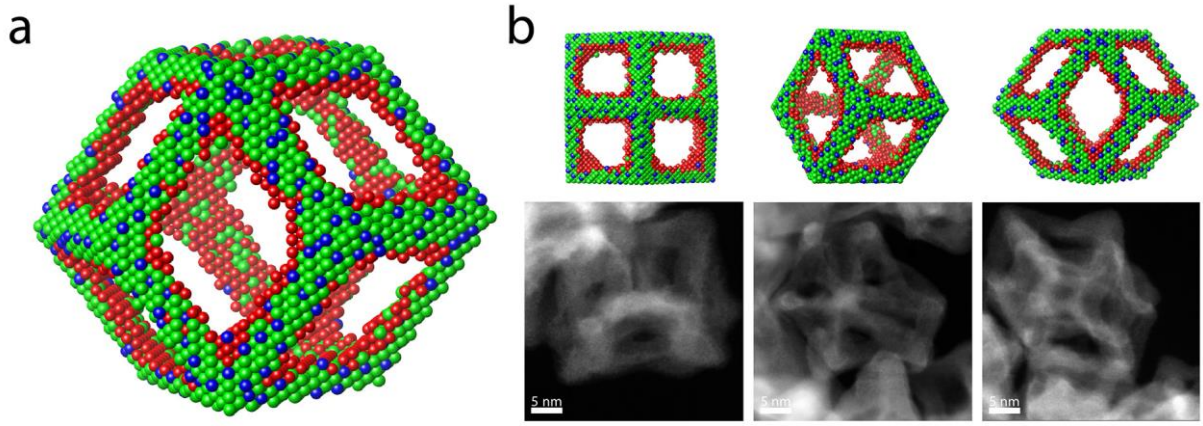

Figure 33. a) Schematic illustration of PtRhNi nanoframes after Ni etching - Pt atoms are green, Rh blue, Ni red; b) models of the three basal projections from three different position with corresponding HAADF STEM images. Note that models are not in scale.

The next step in the preparation of the nanoframes-based catalyst was the etching of the Ni-core from the $PtNi_3$ and PtRhNi rhombic dodecahedral solid nanoparticles with acetic acid in order to obtain Pt_3Ni and PtRhNi nanoframes. An additional advantage of using acetic acid is its ability to remove olyelamine from the surface of the nanoparticles [133]. Based on the STEM images taken for the three different projections of the nanoparticles (Figure 33), it can be stated that after etching the NPs became hollow in the centre forming nanoframes. The particles preserved their rhombic dodecahedral shape, moreover, collapse or frame breaking was not observed. As it can be seen on the HAADF STEM overview images, the Pt_3Ni nanoframes are uniform in shape and size (Figure 34a), while in the PtRhNi nanoframes sample two shapes like in the case of their solid counterparts can still be distinguished (Figure 34b).

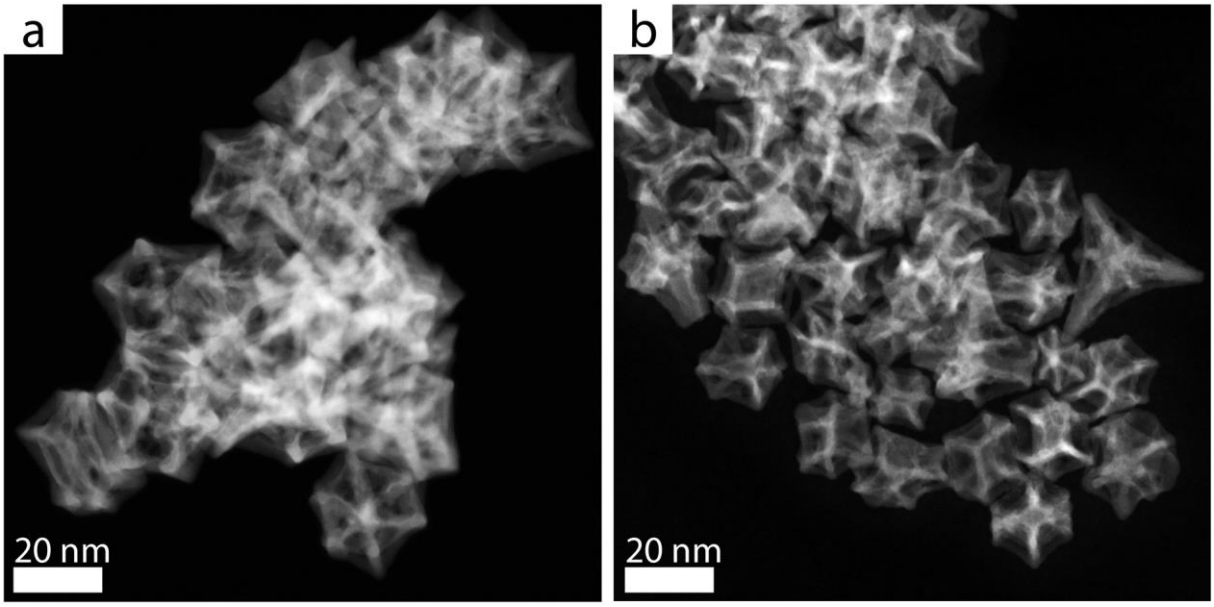

Figure 34. HAADF STEM overview images of a) Pt_3Ni and b) PtRhNi rhombic dodecahedral nanoframes after Ni etching.

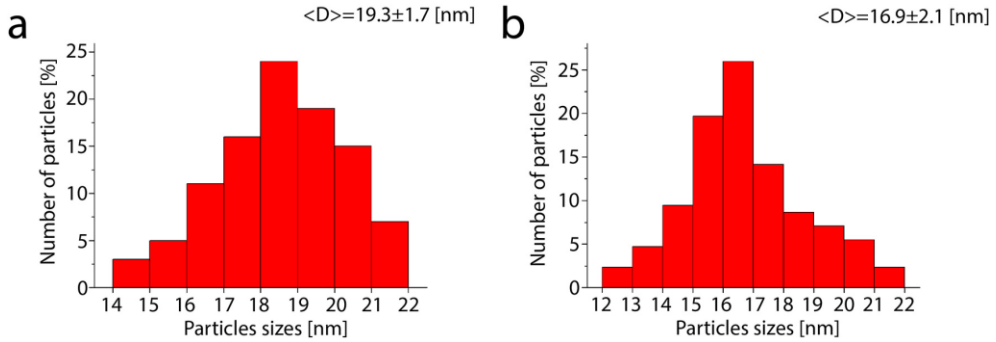

Figure 35. Size distribution of the a) Pt_3Ni and b) PtRhNi rhombic dodecahedral nanoframes after Ni etching.

The size of the Pt_3Ni nanoframes, measured on basis of the STEM images, is between 14 nm – 22 nm, with an average of 19.3±1.7 nm (Figure 35a), while the size of the PtRhNi nanoframes is between 12 – 22 nm with an average of 16.9±2.1 nm (Figure 35b). These results indicate a size reduction of the nanoframes in comparison to the parental $PtNi_3$ and PtRhNi nanopolyhedra, due to the loss of nickel from the core and some platinum and rhodium atoms from the edges. The selected area electron diffraction patterns (Figure 36) confirm the polycrystalline structure of the nanoframes. The diffraction rings, were indexed with the {111}, {200}, {220}, {222} and {311} planes of Pt and Ni for Pt_3Ni nanoframes (Figure 36b) and with the {111}, {200}, {220}, {222} and {311} planes of Pt, Rh and Ni for PtRhNi nanoframes (Figure 36d). Indeed, the observed rings are located between the indexed arcs therefore it is assumed that Pt and Ni in $PtNi_3$ and Pt, Rh and Ni in PtRhNi forms an

alloy phase in the nanoparticles. However, it can be seen that the diffraction rings of Pt_3Ni (Figure 36b) and PtRhNi (Figure 36d) nanoframes are slightly smaller than the diffraction rings for their solid counterparts (Figure 36a and Figure 36b, respectively), due to the higher Pt and Rh content in sample resulting from Ni etching.

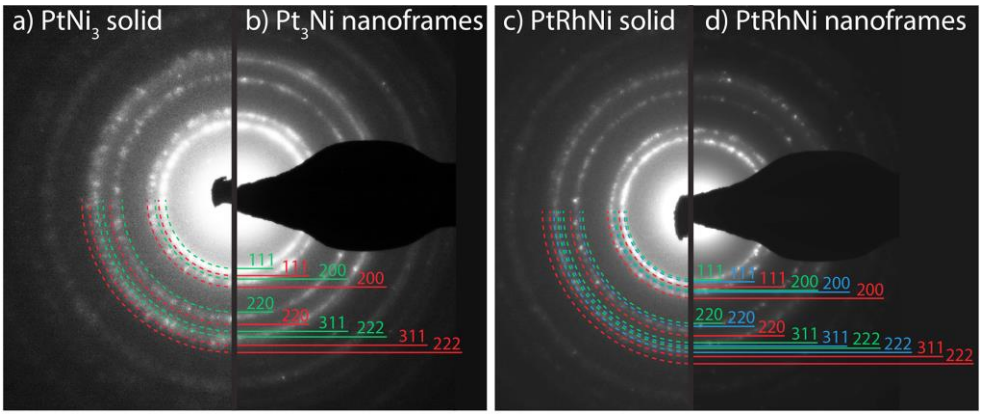

Figure 36. Comparison of selected area electron diffraction patterns of a) $PtNi_3$ rhombic dodecahedral nanopolyhedra with b) Pt_3Ni nanoframes and c) PtRhNi rhombic dodecahedral nanopolyhedra with b) PtRhNi nanoframes. Pt planes are indexed with green lines, Rh with blue lines and Ni with red lines.

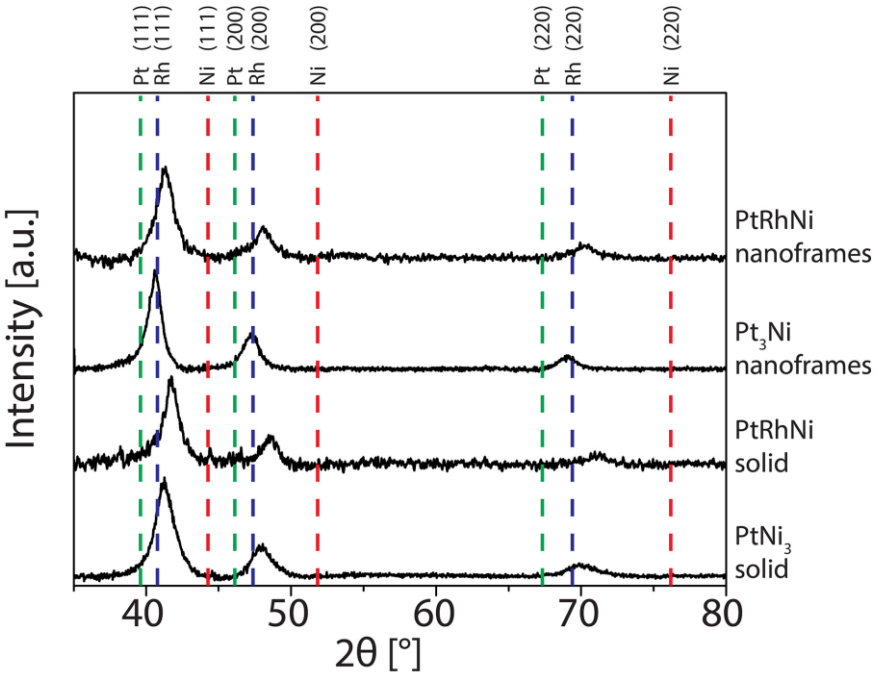

Figure 37. XRD diffractograms of (from bottom to top) $PtNi_3$ nanopolyhedra, PtRhNi nanopolyhedra, Pt_3Ni nanoframes and PtRhNi nanoframes. The standard reflexes for pure Pt – green, Rh - blue and Ni – red are marked for comparison.

In the collected XRD diffractograms (Figure 37), similarly to SAED patterns, the diffraction peaks are located between the peaks identified as {111}, {200}, {220} fcc

platinum and fcc nickel for $PtNi_3$ sample, and fcc platinum, fcc rhodium and fcc nickel in PtRhNi samples. This suggests the formation of a nanoalloy phase of these metals in the nanoframes. However, in comparison to solid $PtNi_3$ and PtRhNi nanopolyhedra, the XRD reflexes originating from Pt_3Ni and PtRhNi nanoframes are shifted towards the lower 2θ values, due to the Ni loss resulting from etching. From both, SAED and XRD, it can be seen that the nickel content in the sample was decreased.

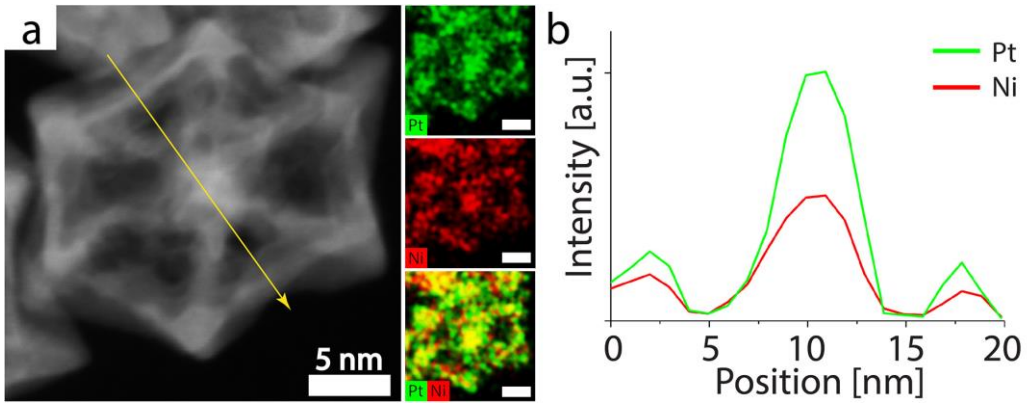

Figure 38. a) HAADF STEM image of single Pt_3Ni nanoframe after Ni etching with the corresponding EDS maps; b) EDS line-scan taken along the line marked in a).

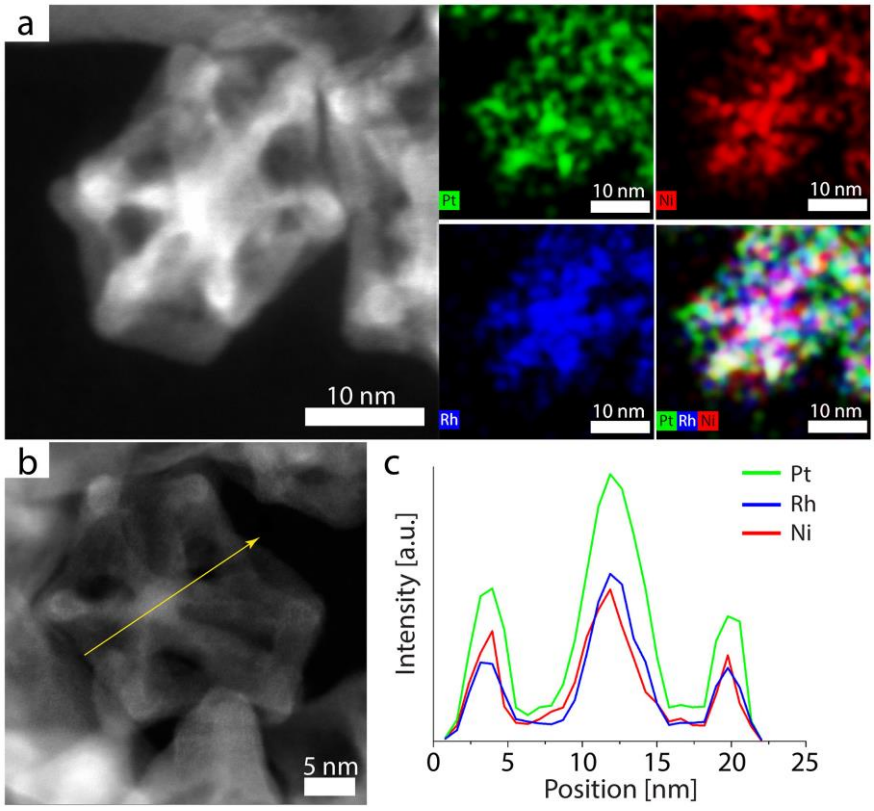

Figure 39. a) HAADF STEM image of a single PtRhNi nanoframe after Ni etching with the corresponding EDS maps; b) HAADF STEM image with the corresponding EDS line-scan through the nanoparticle.

Indeed, EDS elemental mapping confirms the previous observations that nickel was removed from the core of the nanoparticles, but remained at the edges of the nanoframes, forming a nanoalloy with platinum (Figure 38a) or platinum and rhodium (Figure 39a). The EDS line-scan also reveals that the signal from platinum and nickel for Pt_3Ni (Figure 38b) or platinum, rhodium and nickel for PtRhNi (Figure 39) is collected only from the edges, while there is a void in the center of the nanoframes.

The EDS maps were semi-quantitatively analyzed to obtain the atomic ratio of the elements in both samples, and the results were compared with the atomic ratio obtained from the ICP-OES measurements (Table 4). Based on these results, the Pt:Ni and Pt:Rh:Ni atomic ratio could be estimated to 3:1 and 3:1:2, respectively. This ratio corresponds to Pt_3Ni and $Pt_3Rh_1Ni_2$, however to simplify, the $Pt_3Rh_1Ni_2$ will be referred as PtRhNi in further text.

Table 4. Comparison of atomic composition of Pt_3Ni and PtRhNi nanoframes obtained by quantified EDS maps and ICP-OES measurement.

	Atomic %			
	EDS		**ICP-OES**	
	$PtNi_3$	**PtRhNi**	**$PtNi_3$**	**PtRhNi**
Pt	76	51	74	48
Rh	-	17	-	19
Ni	24	32	26	33

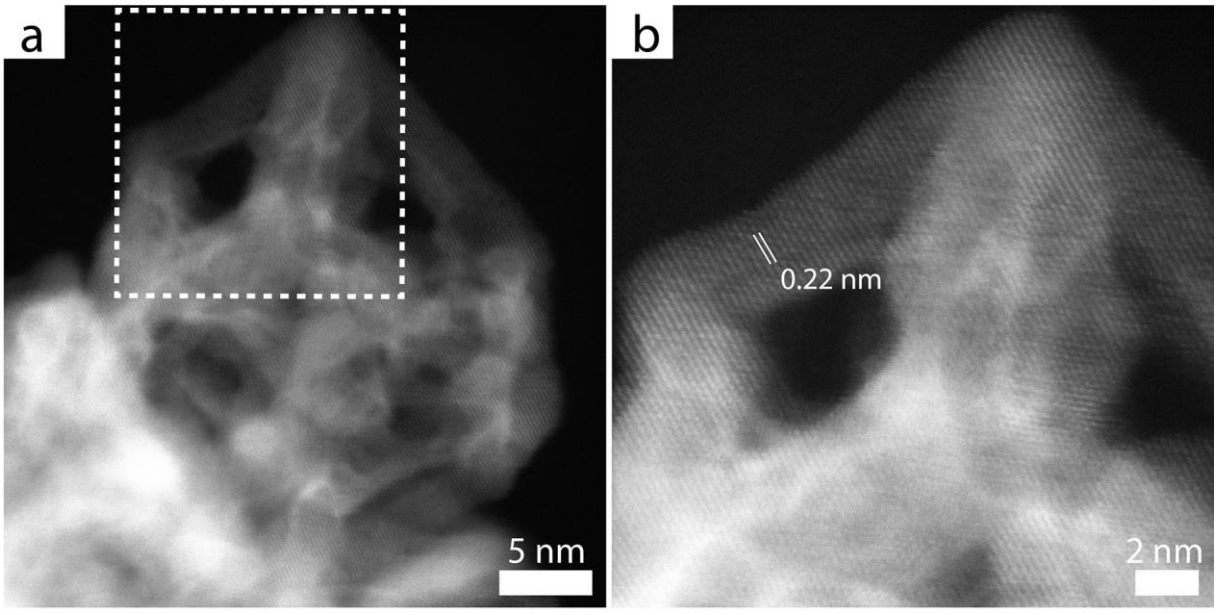

Figure 40. a) High-resolution HAADF STEM image of a Pt_3Ni nanoframe; b) magnified area marked in a) with measured lattice distances on the edge of the nanoframe.

High-resolution HAADF STEM images of Pt_3Ni (Figure 40) and PtRhNi (Figure 41) samples confirm the crystallinity of the obtained nanoframes. The measured lattice distances on the nanoframes (0.21 nm for Pt_3Ni and 0.22 nm for PtRhNi nanoframes) are similar to the lattice distance at the edges of solid nanopolyhedra, which suggests that nickel was not removed from the edges of nanopolyhedra, but only from the interior of the nanoparticles. Indeed, the presence of the PtNi and PtRhNi alloy in the nanoframes was previously confirmed by SAED, XRD and EDS measurements. This is caused by fact that nickel is more stable when it is alloyed with platinum [134]. Nevertheless, due to the fact that some of the PtRhNi nanoframes are rough and slightly amorphous, it can be deduced that the acetic acid treatment partially affects on the PtRhNi alloy forming the nanoframes.

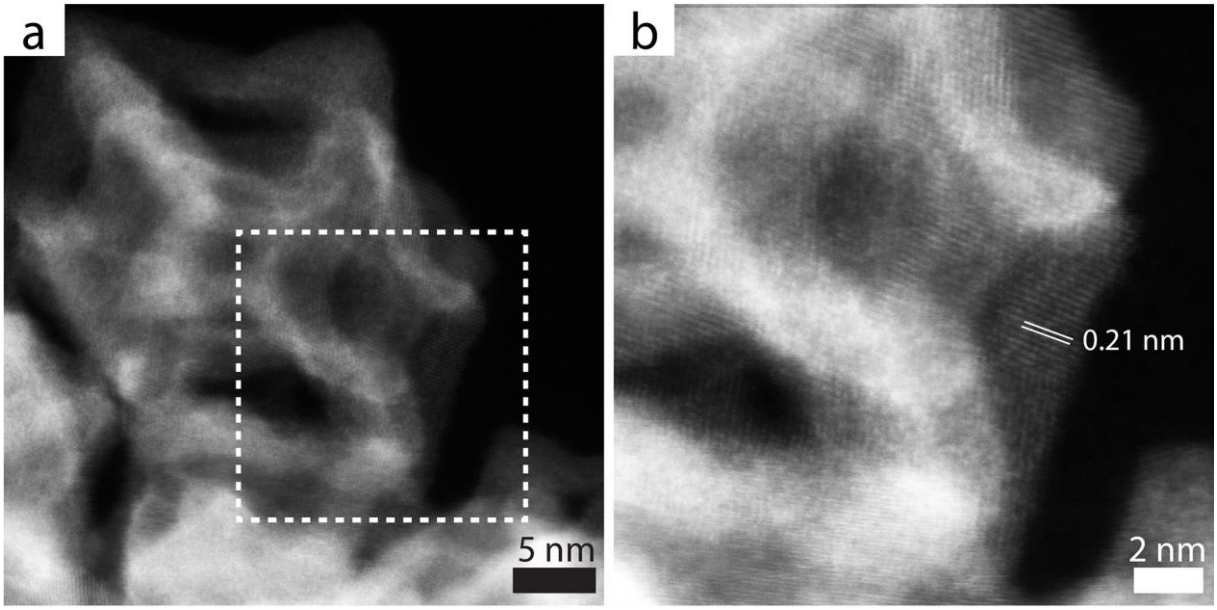

Figure 41. a) High-resolution HAADF STEM image of PtRhNi nanoframes; b) magnified area marked in a) with measured lattice distances on the edge of nanoframe.

The high-resolution HAADF STEM images of Pt_3Ni (Figure 40) and PtRhNi (Figure 41) also show that after etching, the nanoframes are not smooth like they were before Ni removal. Furthermore, locally some of the edges after etching lose their atomic ordering and are rather amorphous (Figure 42a). Additionally, the EDS line-scan through the edges of the etched nanoframes (Figure 42c) reveals that Pt, Rh and Ni are mixed homogeneously within entire nanoframes. Therefore, in order to obtain a Pt-skin layer over the nanoframes and to perform surface restructuring, the Pt_3Ni and PtRhNi nanoframes were, after deposition on carbon Vulcan XC-72, annealed at 200°C. The HAADF HRSTEM image (Figure 42b) shows that after annealing the nanoframes are highly crystalline and have smoother surfaces compared to nanoframes before annealing. Also the EDS line-scan (Figure 42d) reveals that

after annealing, platinum tends to segregate on the surfaces of the nanoframes, forming at least a 0.6 nm thick Pt-skin layer corresponding to three or more Pt monolayers. This migration of Pt atoms to the surface induced by heating causes the formation of a so-called Pt-skin, which was reported before by many groups investigating platinum segregation in Pt-bimetallic systems such as PtNi [17], PtRh [135], PtCo [136], PtSn [20] and other. In this case Pt segregation occurs in the presence of nickel and rhodium. This can be explained by the differences in atomic radii and the surfaces energies [120], similarly like in the case of Pt diffusion during the synthesis of solid PtRhNi NPs. Usually, Pt-skin surfaces consists of to 3 Pt mono layers (ML) [17,137], which correspond to about 0.5 nm thickness. Herein, the measured Pt-skin surface is about 0.6 nm to 0.8 nm thick, which corresponds to 4 and 5 Pt ML. This can be explained by Ostwald ripening occurring during oxygen annealing, which leads to obtaining thicker Pt-skin surfaces [136].

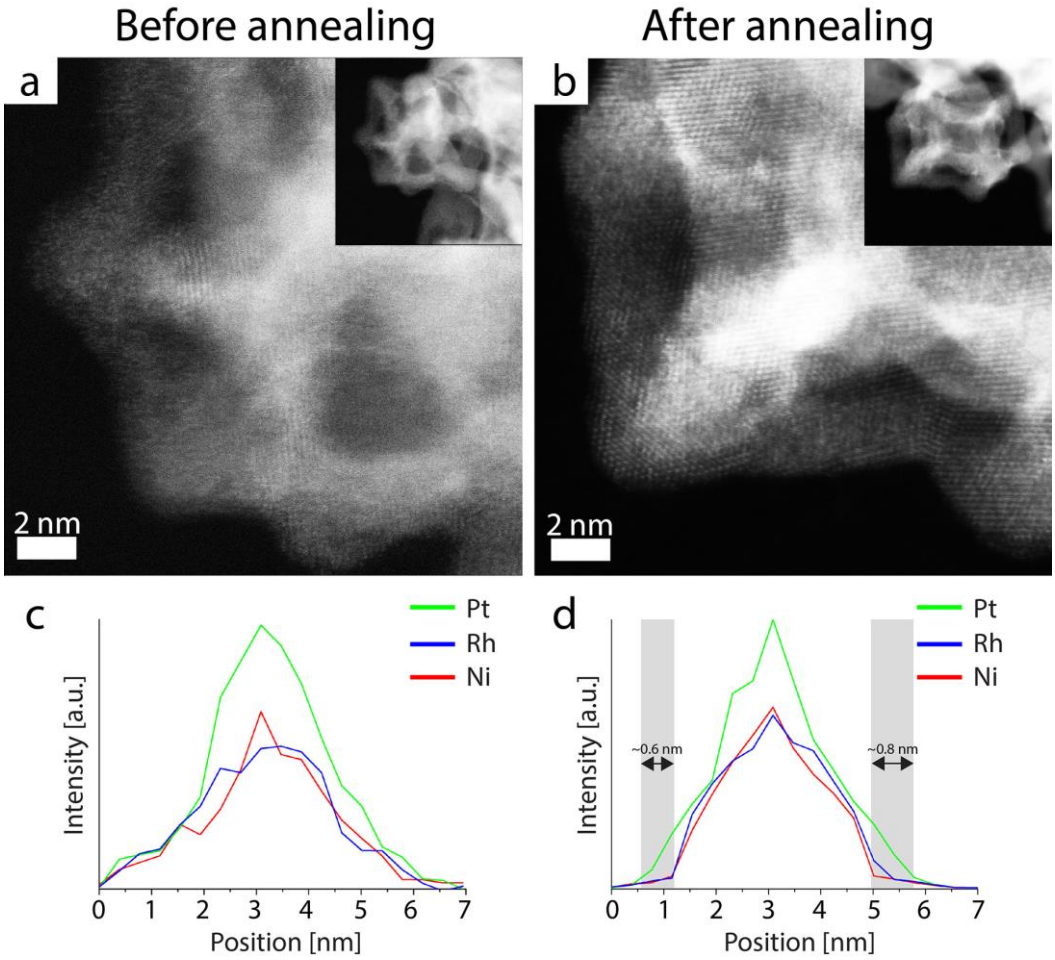

Figure 42. HAADF HRSTEM images of PtRhNi nanoframes a) before and b) after annealing with EDS line-scan through the edges of the PtRhNi nanoframes c) before and d) after annealing, the Pt-skin layer was marked with grey areas. Note that the EDS line-scans do not correspond to the HAADF images.

Due to the high platinum surface area resulting from the presence of dendrites and potential applications in catalysis, dendritic PtNi nanoparticles obtained in synthesis 2 were also treated with acetic acid in order to remove the nickel core. However, only some of the nickel cores of nanoparticles were etched away, thus only a certain volume fraction of the nanoparticles have an open 3D structure. The rest of the nanoparticles have unchanged solid morphology and structure, which was confirmed by STEM observations (Figure 43). This can be explained by the presence of platinum not only at the edges, but also on the facets as thin layer, which protects the nickel against acetic acid and prevented its dissolution [138]. The second explanation could be the fact, that PtNi alloys with Ni content close to 50%, like in this case, which is the most stable composition against etching [139].

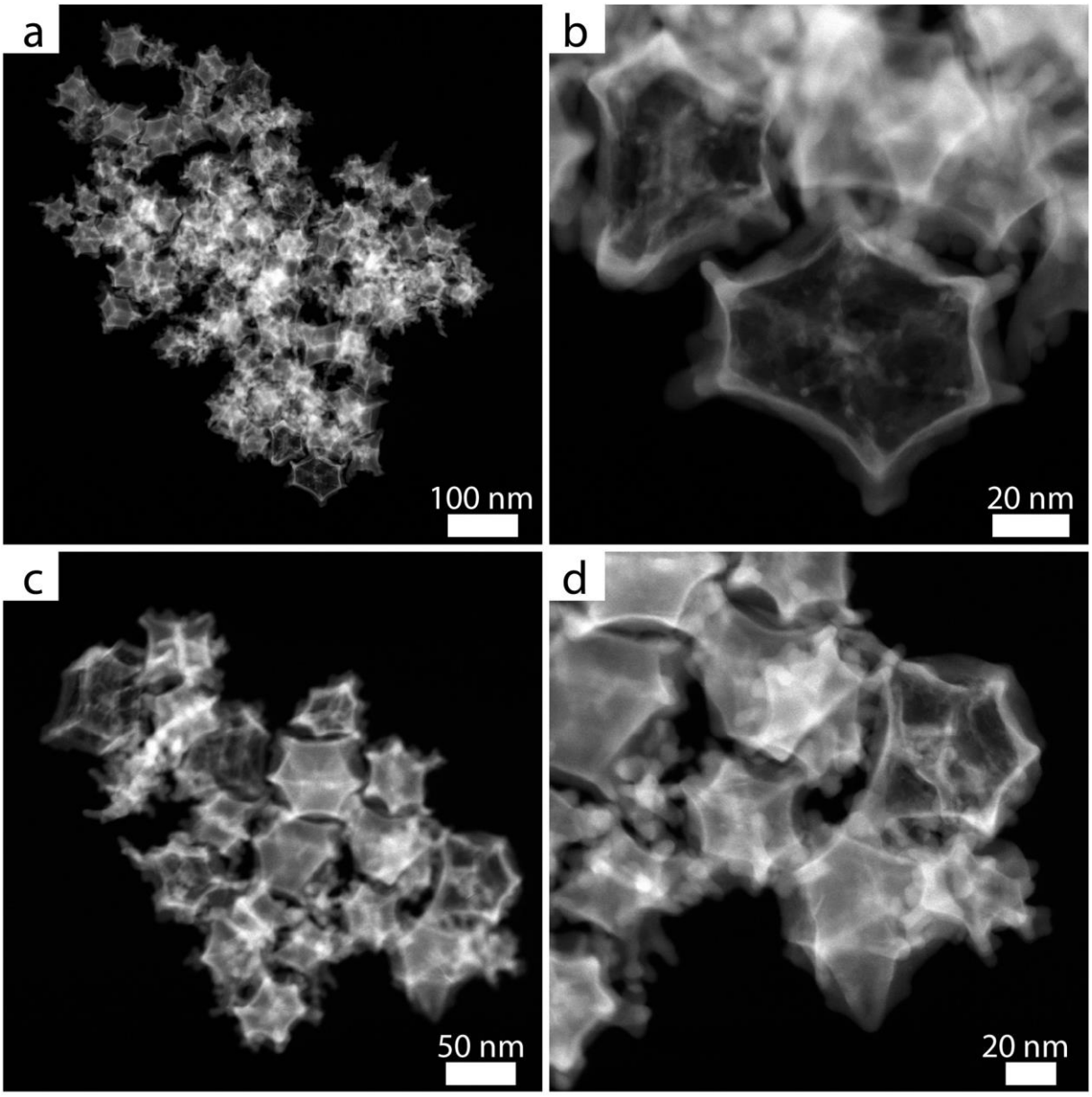

Figure 43. HAADF STEM images of chemically etched dendritically overgrown PtNi nanoparticles.

3.2.2. Thermodynamics of the Pt_3Ni and PtRhNi nanoframes Ni-etching

Thermodynamically, the dissolution energy of metal atoms is directly related with the cohesive energy (E_{coh}) by addition of a constant, which includes the ionization potentials, the vaporization entropy, and the solvation energy [140]. The E_{coh} of the crystal is the energy required to decompose this crystal to free atoms with the same electronic configuration [141]. The lower the E_{coh}, the easier it is to separate the atoms, similarly, the lower the E_{coh}, the easier is to etch the atoms from the nanoparticle surfaces. For instance, for Ni E_{coh_Ni} = 4.44 eV/atom, for Pt E_{coh_Pt} = 5.84 eV/atom, and for Rh E_{coh_Rh} = 5.75 eV/atom [141]. Therefore, by comparing the cohesive energies of Pt, Rh and Ni, it is possible to determine, which element will be easier to remove. However, the cohesive energy depends not only on the type of metal atoms, but also on the atomic plane at which this atom is located and how many and what elements are the nearest neighboring atoms (coordination number) [142]. Due to the fact that E_{coh} values cited above refer to monometallic crystals, they cannot be applied for multimetallic systems. Therefore, due to the fact that the rhombic dodecahedral nanoparticles are enclosed by 12 {110} planes, DFT calculations were performed by using two different models. The first one is the (110) surface of PtRhNi alloy model, which simulates the edges of the rhombic dodecahedral nanoparticles, and the second one is the (110) surface of the monometallic Ni cell model, which simulates the facets of the rhombic dodecahedral nanoparticles. From the first model by removing one Pt, Rh or Ni atom, E_{coh_Pt}, E_{coh_Rh}, E_{coh_Ni} respectively were calculated. Analogously, from the second model by removing one Ni atom, E_{coh_Ni} was calculated. All calculated energies are presented in Table 5.

Table 5. Atomic cohesion energies calculated by density functional theory. The Ni, Pt and Rh refer to which atom was removed, while (Ni) and (PtRhNi) refer to the model with only Ni atoms and to the model with Pt, Rh and Ni atoms, respectively.

	E_{coh} [eV/atom]
Ni (Ni)	5.429
Ni (PtRhNi)	5.776
Pt (PtRhNi)	6.259
Rh (PtRhNi)	6.197

Based on the calculated E_{coh} values it can be concluded that from the thermodynamic point of view, the etching process will proceed in the following order: Ni atoms from the facets of the nanoparticles > Ni atoms from the edges of the nanoparticles > Rh atoms from

the edges of nanoparticles > Pt atoms from the edges of nanoparticles. These results indicate that mainly Ni atoms are removed from the facets of rhombic dodecahedral nanoparticles, which is confirmed by the STEM images and EDS maps. However locally, amorphization of some of the Pt- or PtRh-rich edges after etching is observed on the STEM images (Figure 42a). This can be caused by the fact that Pt, Rh and Ni atoms at the edges are poorly coordinated, thus they are susceptible to partial etching, despite that they have a relatively high E_{coh} value in comparison to Ni atoms on the facets of the nanoparticles. Nevertheless, it is worth noticing that only part of the Pt- and PtRh-rich edges are amorphous, most of them remain crystalline.

According to Wu et. al. [142], who proposed the chemical etching mechanism of PtNi alloys based on DFT calculations, there are three conditions that must be fulfilled for Ni-etching. First, the content of Ni must be higher in comparison to the Pt or PtRh content. Second, the etched nanoparticles must be enclosed by active surfaces, for example {110}, which ensures the formation of voids. Third, an etching solution should be chosen, which could selectively etch nickel, but not affect platinum and rhodium. All of the above mentioned conditions are met in the case of $PtNi_3$ and PtRhNi parental nanoparticles. Firstly, in both cases there is an excess of nickel in comparison to platinum and rhodium. Secondly, the rhombic dodecahedrons are enclosed by {110} facets. Finally, the acetic acid used as an etchant is not corrosive to platinum and rhodium. Therefore, it is possible to obtain Pt_3Ni and PtRhNi nanoframes from solid $PtNi_3$ and PtRhNi rhombic dodecahedral nanoparticles, by etching in acetic acid.

3.2.3. Synthesis of the SnO_2 nanoparticles and assembly of SnO_2@Pt_3Ni and SnO_2@PtRhNi heteroaggregates

The next stage was to synthesize small, about 3 nm, SnO_2 NPs. Based on the overview HAADF STEM images (Figure 44a) it can be seen that the obtained nanoparticles are spherical with average diameter of 2.6±0.4 nm (Figure 44b). The HAADF HRSTEM image (Figure 45b) confirms the crystallinity of the nanoparticles, while the measured lattice distance is 0.27 nm and 0.34 nm, which correspond to (101) and (110) planes of tetragonal SnO_2, respectively.

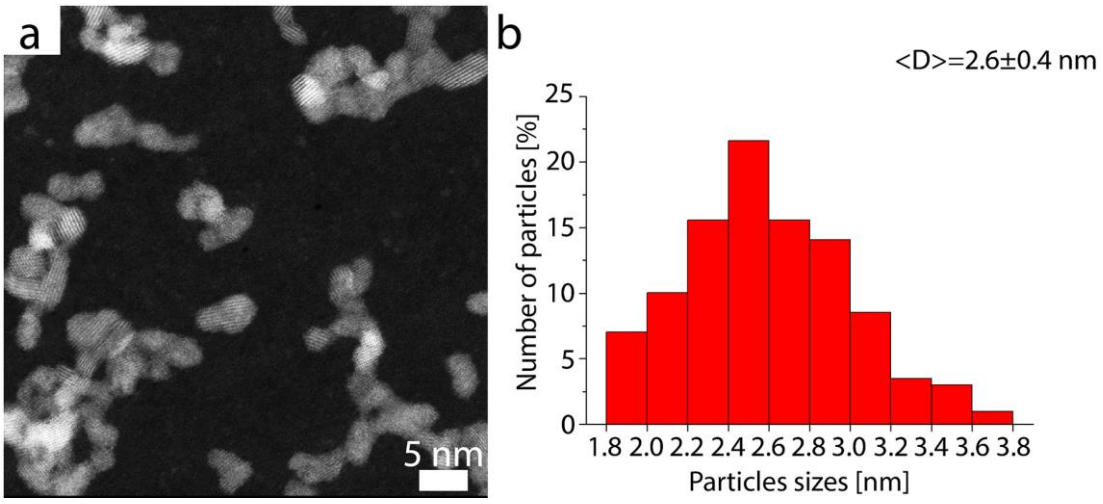

Figure 44. a) HAADF STEM overview image; b) size distribution of the SnO_2 nanoparticles.

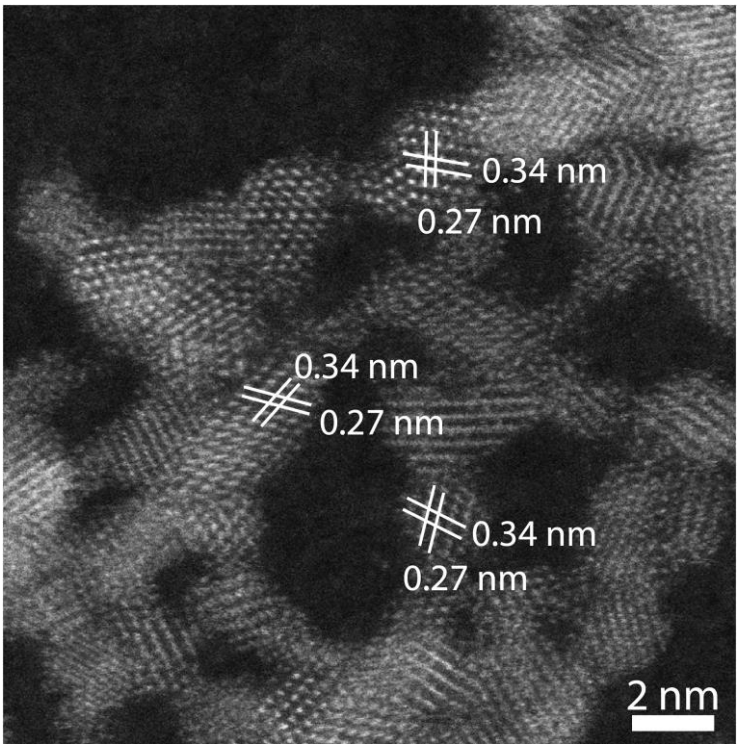

Figure 45. HAADF HRSTEM image of SnO_2 NPs with measured lattice distances.

The crystallinity of the SnO_2 nanoparticles is also confirmed by the SAED patterns (Figure 46a), the presented set of diffraction rings can be indexed as the {110}, {101}, {200}, {111}, {210}, {211} and {220} planes of tetragonal SnO_2. The crystallinity of SnO_2 is also confirmed by XRD (Figure 46b), the reflexes presented on the diffractogram can be indexed as {200}, {211} and {112} planes of tetragonal SnO_2. Moreover, the reflexes are broad, which indicates that the SnO_2 NPs are indeed very small, which is confirmed by the STEM observations. Additionally, there are no visible peaks originating from metallic Sn.

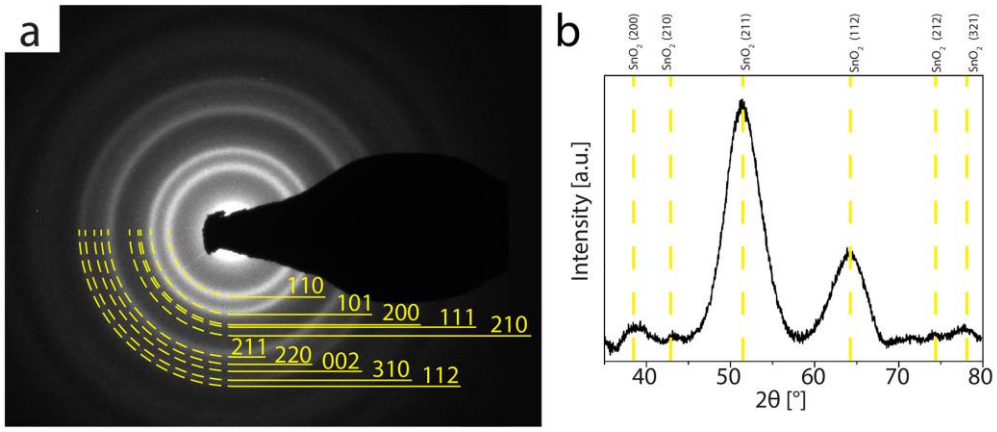

Figure 46. a) Selected area electron diffraction patterns and b) XRD diffractogram of SnO_2 nanoparticles.

The obtained Pt_3Ni and PtRhNi nanoframes were decorated by small crystalline SnO_2 nanoparticles in order to enhance their catalytic performance in ethanol oxidation reaction. In the literature of the subject, there are reports, in which usually small Pt NPs are deposited on larger oxide nanoparticles [143]. However, in this study relatively large, Pt-containing nanoframes (~20 nm), were decorated by smaller SnO_2 NPs (~ 2 nm), in order to maximize the interface surface between both types of nanoparticles and shorten the distance of catalytically active sites between the PtRh alloy and the SnO_2 NPs. The controlled deposition of the SnO_2 NPs on the nanoframes was possible due to the electrostatic interactions resulting from the difference in their the zeta potentials [96]. The zeta potential measurements were performed in a pH range between 3.5 – 13 (Figure 47).

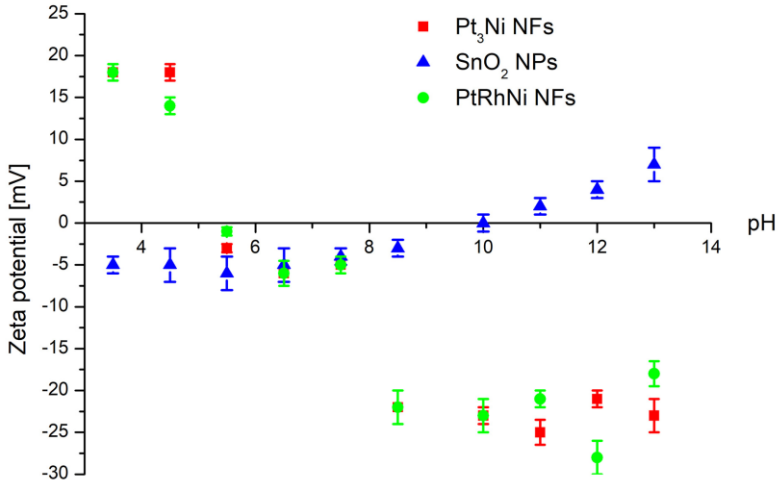

Figure 47. Dependence of the zeta potential on the pH for Pt_3Ni nanoframes, PtRhNi nanoframes and SnO_2 nanoparticles.

It is worth noticing that for both nanoframe samples, the zeta potentials at different pH are very similar or even the same. The zeta potential exhibits initially a high value of 18 mV

at a pH = 3.5, but with increasing pH values the zeta potential decreases until reaching the isoelectric point at pH ≈ 5. With further increasing pH values, the zeta potential still decreases. On the other hand, the zeta potential values for SnO_2 are completely different. First at pH = 3.5 the zeta potential equals to -6.5 mV, while with the increasing pH this value is roughly constant up to a value of pH = 10 where the isoelectric point is located. With further increasing the pH, the zeta potential also increases. Based on these results, it can be seen that either at low pH values (below 5) or at high pH values (over 10) the zeta potentials of the nanoframes and of the SnO_2 NPs have opposite signs. It is worth mentioning, that the nanoframes containing solution as well as the SnO_2 containing solution must have the same pH values, in order to obtain a solution with the same pH after mixing. This is crucial, due to the fact that the zeta potential strongly depends on pH, even a small change in pH could affect the zeta potential, and as a consequence the deposition of SnO_2 NPs on the nanoframes would be impossible [97]. Therefore, the connection of the Pt_3Ni and PtRhNi nanoframes with the SnO_2 NPs was performed at a pH = 4.5. Interestingly, the zeta potentials of the obtained SnO_2 NPs are different than those reported previously, where the zeta potential is positive at pH range from 2 to about 5.6 [144]. In the present study, the zeta potential of the SnO_2 NPs prepared for decoration of the nanoframes takes negative values in this pH range. This can be attributed to the presence of citric acid, which is used as a capping and reducing agent during the synthesis of the SnO_2 nanoparticles. The -COOH functional groups of citric acid at low pH (below 7.4) can be deprotonated to $-COO^-$, which explains the decrease of the zeta potential of the nanoparticles [145].

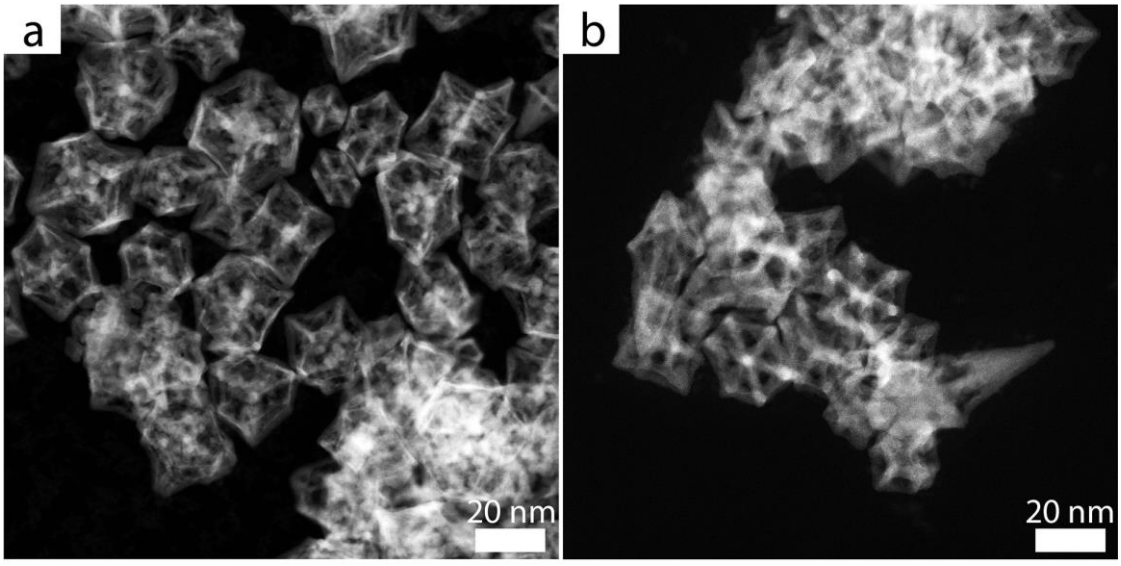

Figure 48. HAADF STEM overview images of a) Pt_3Ni and b) PtRhNi nanoframes decorated with SnO_2 nanoparticles.

On the HAADF STEM overview images of the obtained SnO_2@Pt_3Ni (Figure 48a) and SnO_2@PtRhNi (Figure 48b) heteroaggregates only the nanoframes are visible, probably due to the relatively low magnification. However, based on the three different projections of STEM images at higher magnification (Figure 49), both, nanoframes and SnO_2 NPs are visible. Due to the difference in Z-number of Pt and Sn, the Pt-rich nanoframes have a more intensive contrast in the HAADF STEM images than the SnO_2 NPs.

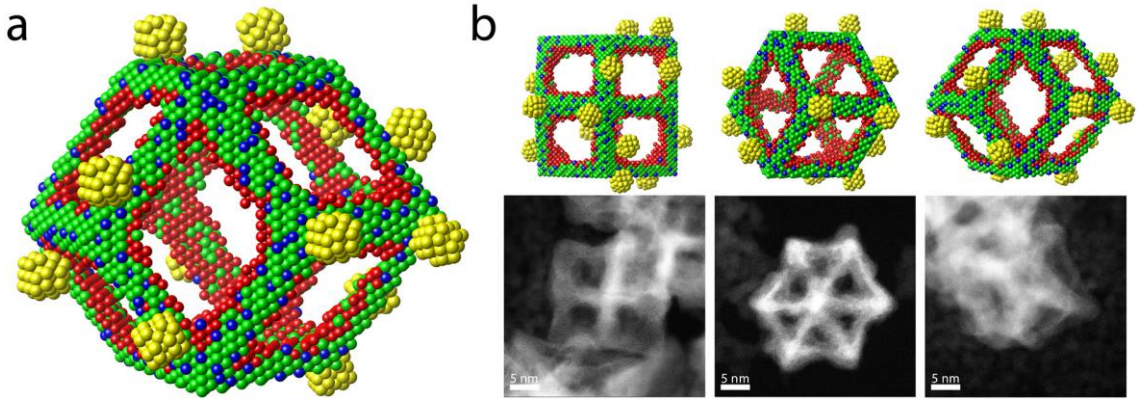

Figure 49. a) Schematic illustration of PtRhNi nanoframes after SnO_2 NPs deposition - Pt atoms are green, Rh blue, Ni red, SnO_2 NPs yellow; b) models of the three basal projections with corresponding HAADF STEM images. Note that the models are not in scale.

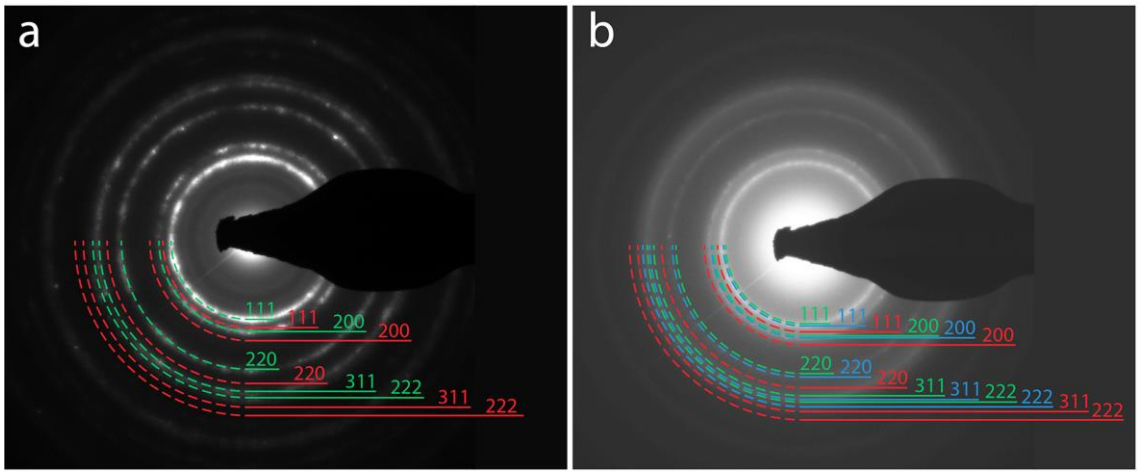

Figure 50. Selected area electron diffraction patterns of a) Pt_3Ni and b) PtRhNi nanoframes decorated with SnO_2 nanoparticles. The Pt planes are indexed with green lines, Rh with blue lines and Ni with red lines.

The selected area electron diffraction patterns (Figure 50) confirm the polycrystalline structure of the nanoframes. The diffraction rings, were indexed with the {111}, {200}, {220}, {222} and {311} planes of Pt and Ni for SnO_2@Pt_3Ni (Figure 50a) and with the {111}, {200}, {220}, {222} and {311} planes of Pt, Rh and Ni for SnO_2@PtRhNi (Figure

50b). However, there are no visible diffraction rings corresponding to SnO_2 nanoparticles. This poor detection of SnO_2 NPs by diffraction methods is probably caused by the small size of the oxide nanoparticles. It is similar in the case of XRD diffractograms (Figure 51a), where diffraction peaks are located between peaks identified as the {111}, {200}, {220} planes of fcc platinum and fcc nickel for SnO_2@Pt_3Ni sample, and fcc platinum, fcc rhodium and fcc nickel in SnO_2@PtRhNi sample. However, in both samples additional reflexes are visible (Figure 51b), which could be indexed as (211) and (112) planes of tetragonal SnO_2.

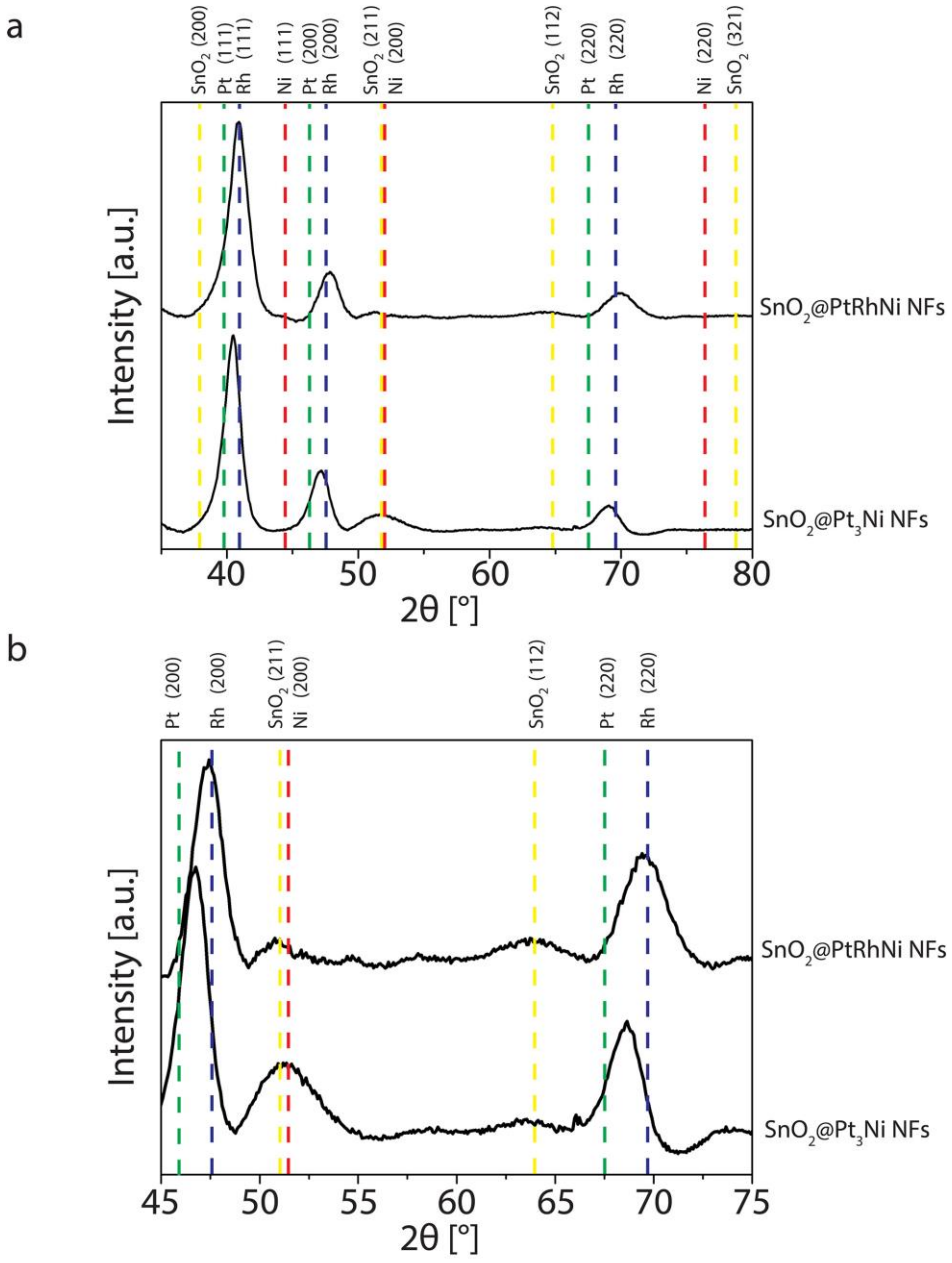

Figure 51. a) XRD diffractograms of Pt_3Ni (lower pattern) and PtRhNi nanoframes (upper pattern) decorated with SnO_2 nanoparticles; b) magnified section of the diffractogram presented in a). The standard reflexes for pure Pt – green, Rh – blue, Ni – red and SnO_2 - yellow are marked for comparison.

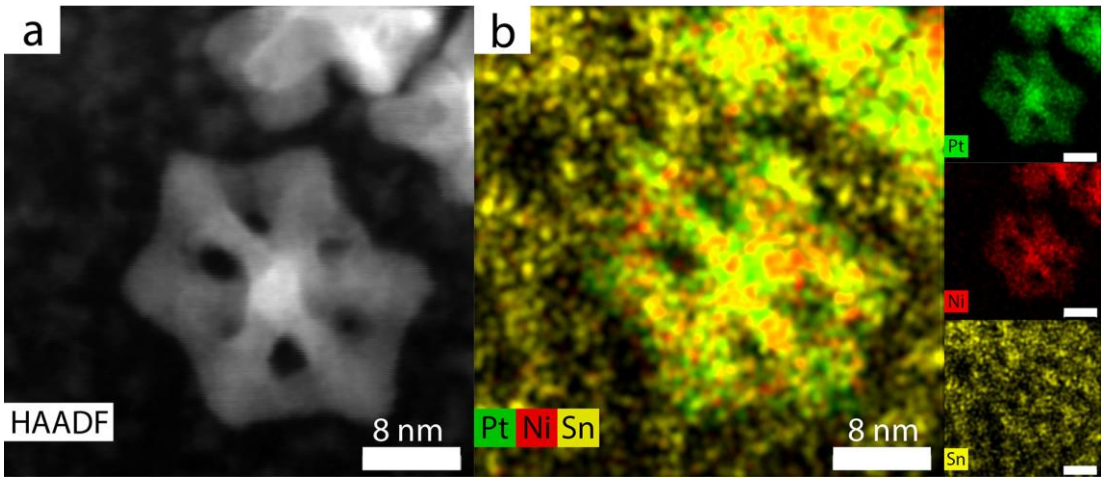

Figure 52. a) HAADF STEM image of a single Pt_3Ni nanoframe decorated with SnO_2 NPs with b) the corresponding EDS maps.

EDS elemental mapping confirms the presence of the SnO_2 NPs deposited on the outer and inner surface of the Pt_3Ni (Figure 52) and PtRhNi nanoframes (Figure 53). However, the SnO_2 NPs are not only deposited on the nanoframes, but are also present individually in the whole volume of the sample. The EDS maps were semi-quantitatively analyzed to obtain the atomic ratio of the elements in both samples, and the results were compared with atomic ratio obtained by the ICP-OES measurements (Table 6). Based on the EDS results, the Pt:Ni:Sn atomic ratio can be estimated as 3:1:4 (EDS) for the SnO_2@PtRhNi and the Pt:Rh:Ni:Sn atomic ratio is 3:1:2:3 for the SnO_2@PtRhNi. On the other hand, based on the ICP-OES measurements the Pt:Ni:Sn atomic ratio is 3:1:8, while in Pt:Rh:Ni:Sn the atomic ratio is 3:1:2:10. This difference between EDS and ICP results can be attributed to the fact that EDS is a local technique, while ICP-OES provides global information.

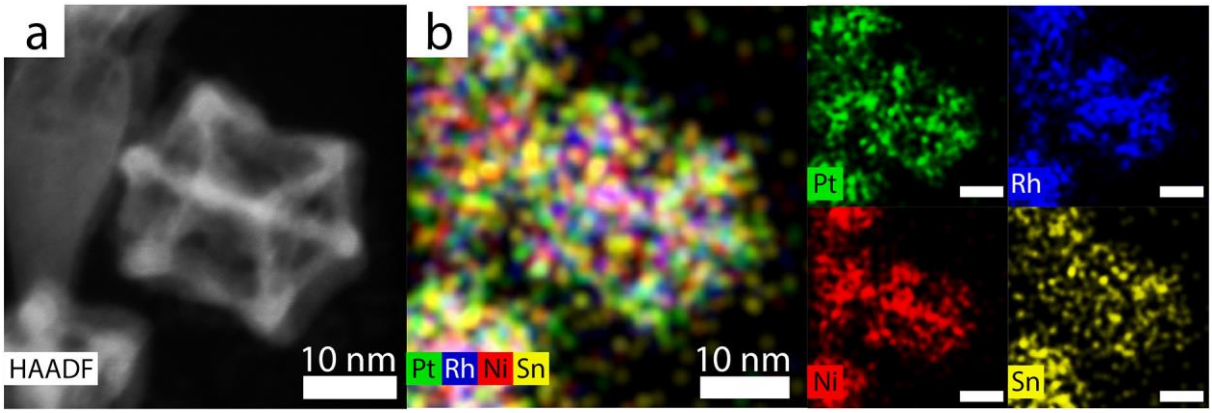

Figure 53. a) HAADF STEM image of single PtRhNi nanoframes decorated with SnO_2 NPs with b) corresponding EDS maps.

Table 6. Comparison of atomic composition of Pt_3Ni and PtRhNi nanoframes decorated with SnO_2 NPs obtained by quantified EDS spectra and ICP-OES measurements.

	Atomic %			
	EDS		ICP-OES	
	$PtNi_3$	PtRhNi	$PtNi_3$	PtRhNi
Pt	39	35	25	19
Rh	-	11	-	6
Ni	12	21	8	11
Sn	49	33	67	64

The HRSTEM bright field image of the SnO_2@Pt_3Ni sample (Figure 54) clearly shows that small SnO_2 NPs are attached to the Pt_3Ni frame. The measured lattice distance of 0.32 nm corresponds to (110) SnO_2 planes.

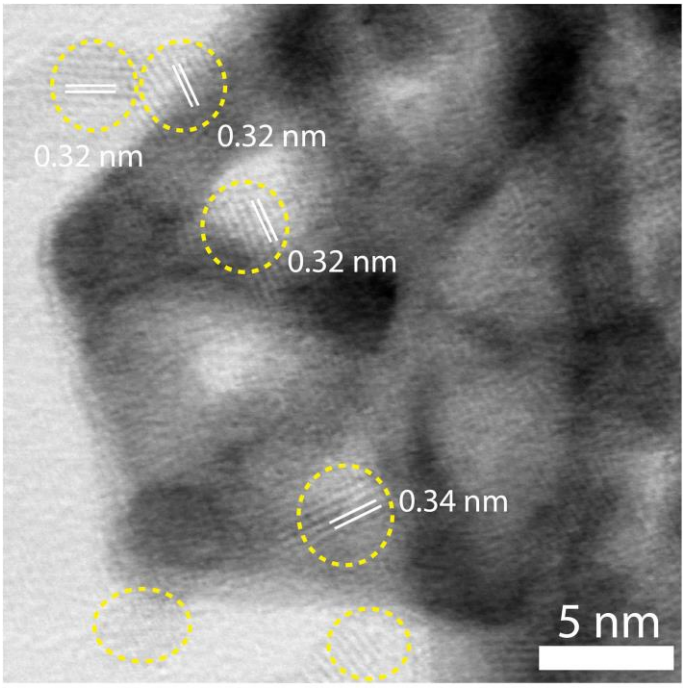

Figure 54. High-resolution STEM bright field image of $PtNi_3$ nanoframes decorated with SnO_2 NPs (marked with yellow ellipses).

Similarly, the high-resolution STEM bright-field image allows to observe that indeed SnO_2 NPs are deposited on PtRhNi nanoframes (Figure 55b). The lattice distance of 0.18 nm and 0.21 nm measured on the HRSTEM bright field image could be indexed as the (200) and (111) planes of fcc PtRhNi alloy. On the other hand, the measured lattice distances of 0.24 nm, 0.26 nm, 0.32 nm and 0.33 nm could be indexed as the (200), (101) and (110) planes of tetragonal SnO_2, respectively. The HAADF STEM image (Figure 55a) and the 3d model of the frames (Figure 55c) are shown to better illustrate the shape and different orientations of

the presented nanoframes. In this STEM photograph the SnO_2 NPs are deposited only directly on PtRhNi nanoframes surfaces, however a certain volume fraction of the SnO_2 NPs are also found outside the nanoframes in the sample (Figure 56).

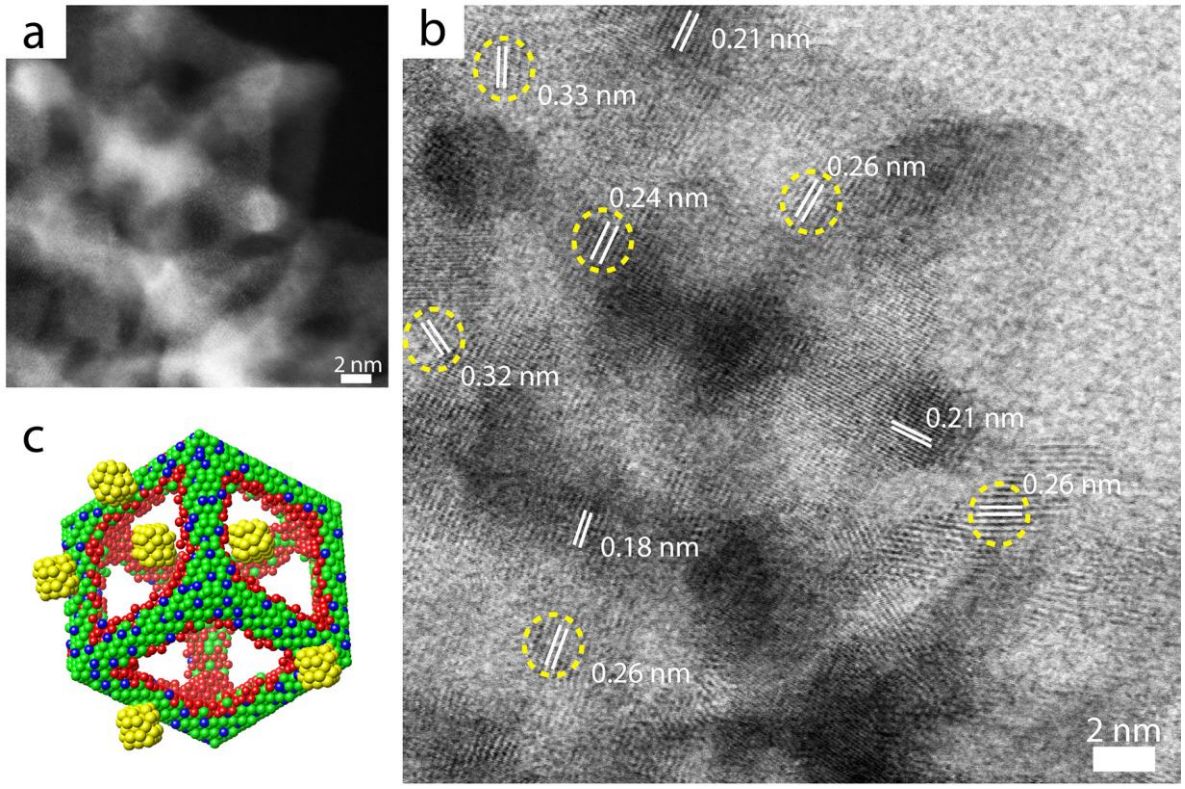

Figure 55. a) HAADF STEM and b) bright field HRSTEM images of a single PtRhNi nanoframe decorated with SnO_2 NPs with measured lattice distances. SnO_2 NPs are marked with yellow ellipses; c) schematic illustration of a nanoframe decorated with SnO_2 shown in a) and b).

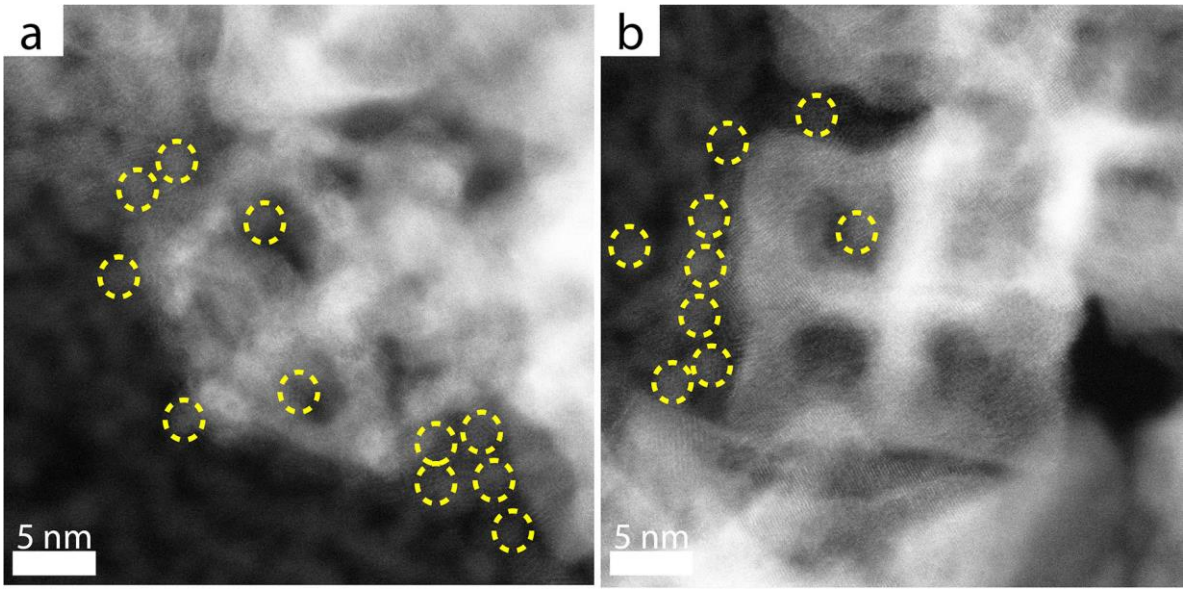

Figure 56. HAADF STEM images of PtRhNi nanoframes decorated with SnO_2 NPs; some of the deposited SnO_2 NPs are marked with yellow ellipses.

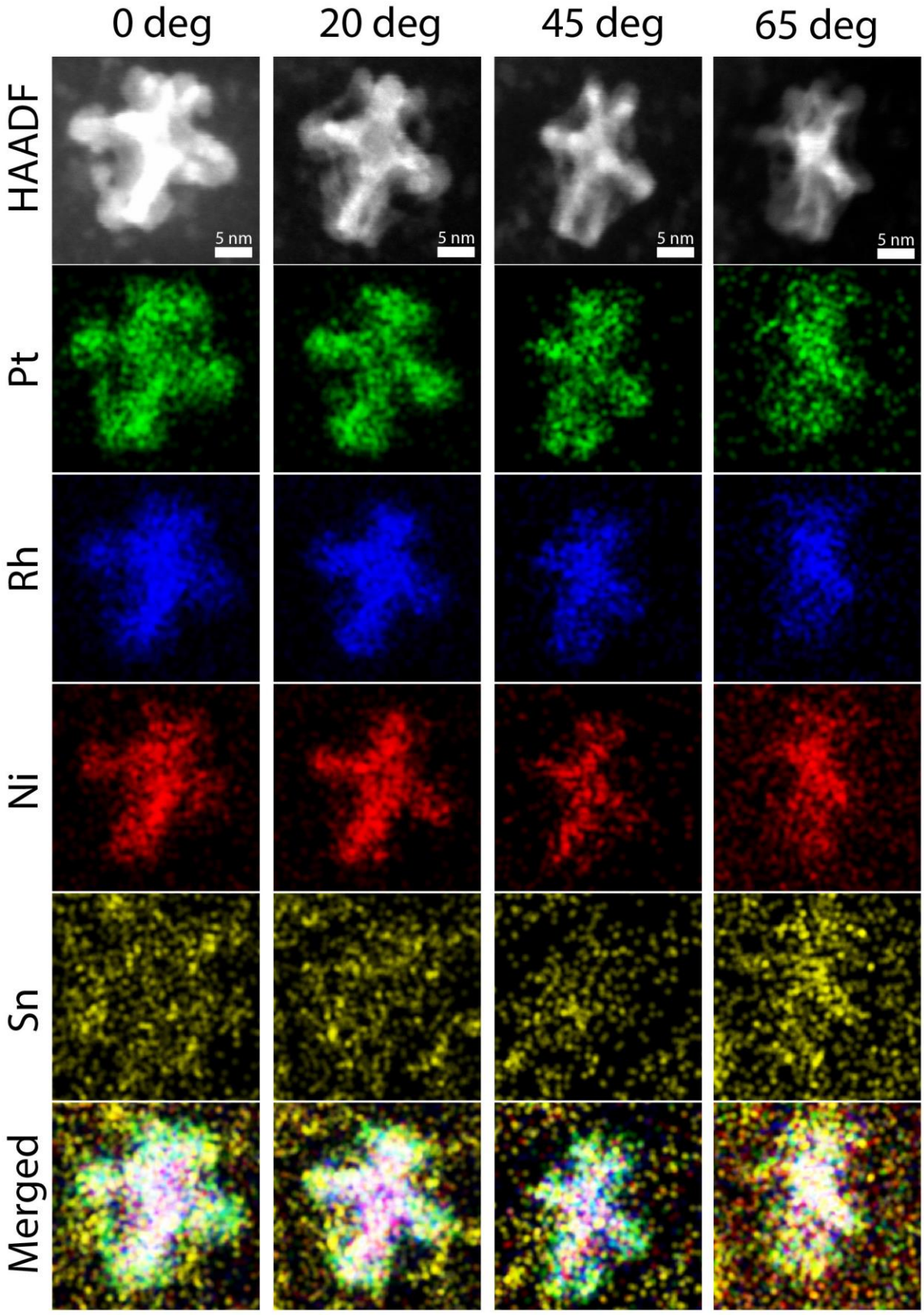

Figure 57. EDS tilt series of the PtRhNi nanoframes decorated with SnO_2 NPs.

Due to the fact that the STEM images are 2D projections of 3D objects, sometimes it is hard to determine whether the SnO_2 NPs are attached to surface of the nanoframes or are only placed next to nanoframes without physical contact. To verify that, EDS tilt series were performed (Figure 57), which visualize that the signal from tin is recorded on the nanoframes from different sides. Unfortunately, during exposure to the electron beam the nanoframes were damaged, which is visible on the images. However, it can be noticed that the tin signal is on the nanoframes, no matter from which angle the EDS map is acquired. Both samples SnO_2@Pt_3Ni and SnO_2@PtRhNi after deposition on the Vulcan carbon were annealed at 200°C in order to obtain Pt-skin layer and surface restructuration analogously as in the case of Pt_3Ni and PtRhNi nanoframes.

3.3. Kinetics of formation of $PtNiSnO_2$ and $PtRhNiSnO_2$ nanoframes by galvanic replacement reaction[1]

3.3.1. Obtaining the $PtNiSnO_2$ and $PtRhNiSnO_2$ nanoframes by galvanic replacement reaction

To obtain hollow PtNi and PtRhNi nanoframes covered by a thin layer of Sn, a galvanic replacement reaction (GRR) was performed. This reaction occurs by oxidative dissolution of nickel from the core of the solid rhombic dodecahedral nanoparticles (here called "parental" or "template") and reductive deposition of Sn^{4+} ions from the $SnCl_4$•$5H_2O$ salt onto the surface of the resulting nanoframes.

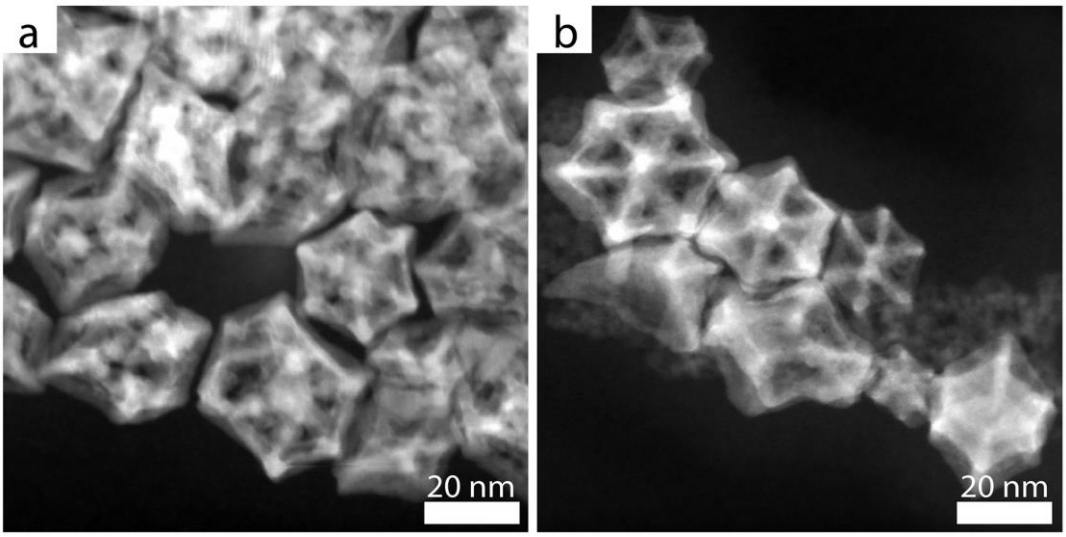

Figure 58. HAADF STEM overview images of a) PtNiSn and b) PtRhNiSn nanoframes.

[1] Results presented in this chapter were partially published in Nanoscale journal ("Conversion of bimetallic $PtNi_3$ nanopolyhedra to ternary PtNiSn nanoframes by galvanic replacement reaction", DOI:10.1039/C9NR01359H).

As it can be seen on HAADF STEM overview images (Figure 58) nanoframes are hollow inside, but preserved their rhombic dodecahedral shape, indeed, collapse or frames breaking was not observed. Both, PtNiSn (Figure 58a) and PtRhNiSn (Figure 58b) samples, mostly containing hollow nanoframes, however there are still some solid nanoparticles, but they constitute less than 10% of the total.

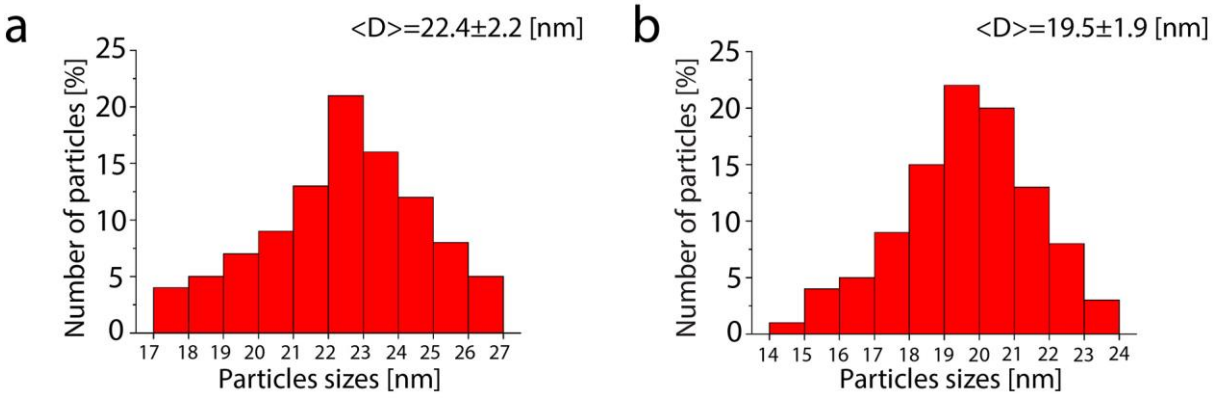

Figure 59. Size distribution of the a) PtNiSn and b) PtRhNiSn nanoframes after GRR.

The size of the PtNiSn hollow nanoframes, measured on basis of the STEM images, is between 17 nm – 27 nm, with an average of 22.4±2.2 nm (Figure 59a), while the size of the PtRhNi nanopolyhedra is between 14 – 24 nm with an average of 19.5±1.9 nm (Figure 59b). These results show an increase of about 2 nm of the nanoframes size in comparison to parental $PtNi_3$ and PtRhNi nanopolyhedra caused by Sn deposition. This indicates that the Sn-layer on the nanoframes has nearly 1 nm from each side.

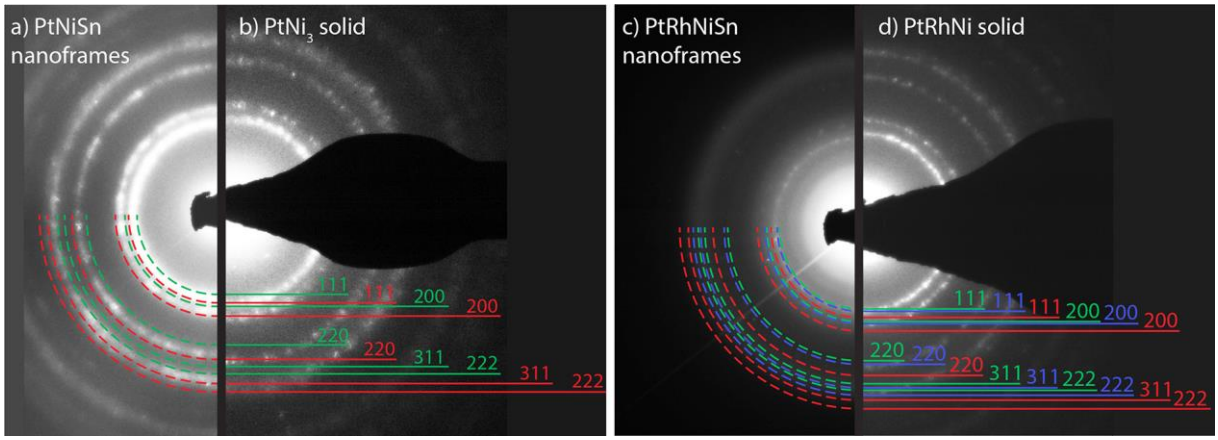

Figure 60. Comparison of selected area electron diffraction patterns of a) PtNiSn nanoframes with b) $PtNi_3$ rhombic dodecahedral nanopolyhedra and c) PtRhNiSn nanoframes with d) PtRhNi rhombic dodecahedral nanopolyhedra. The Pt planes are indexed with green lines, Rh with blue lines and Ni with red lines.

The selected area electron diffraction patterns (Figure 60) confirm the polycrystalline structure of the nanoframes. The diffraction rings, were indexed with the {111}, {200}, {220}, {222} and {311} planes of Pt and Ni for PtNiSn nanoframes (Figure 60a) and with the {111}, {200}, {220}, {222} and {311} planes of Pt, Rh and Ni for PtRhNi nanoframes (Figure 60c). Indeed, the observed rings are located between the indexed arcs, therefore it is assumed that Pt and Ni in PtNiSn and Pt, Rh and Ni in PtRhNi formed an alloy phase in the nanoparticles. Moreover, it can be seen that the diffraction rings of PtNiSn (Figure 60a) and PtRhNiSn (Figure 60c) nanoframes are slightly smaller than the diffraction rings for their parental counterparts (Figure 60b and Figure 60d, respectively). This is due to the higher Pt and Rh content in the sample resulting from Ni oxidative dissolution during the replacement with Sn^{4+} ions. Furthermore, no diffracion rings originating from Sn are visible, probably due to the fact that the Sn-layer is too thin (~1 nm) to be detected by SAED.

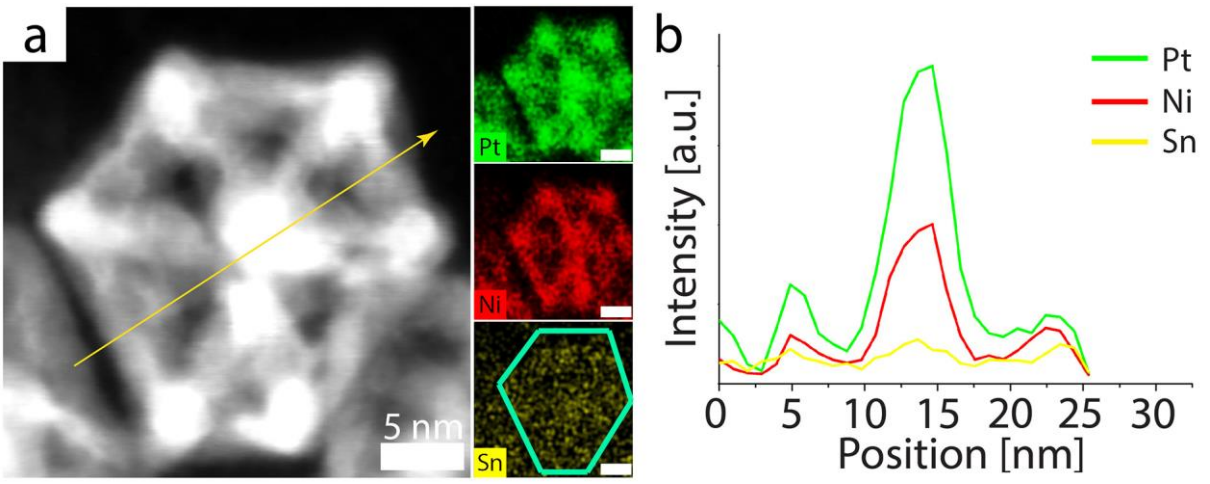

Figure 61. a) HAADF STEM image of a single PtNiSn nanoframe with the corresponding EDS maps; b) EDS line-scan taken along the line marked in a).

The EDS elemental mapping confirms the previous observation that nickel was removed from the core of the nanoparticles, but remained at the edges of nanoframes, forming a nanoalloy with platinum (Figure 61a) or platinum and rhodium (Figure 62a). Moreover, either PtNiSn and PtRhNiSn nanoframes are covered by tin. Also, the EDS line-scan confirms the hollow structure of PtNiSn (Figure 61b) and PtRhNiSn (Figure 62c) nanoframes with a void in the center. The EDS maps were semi-quantitatively analyzed to obtain the atomic ratio of the elements in both samples, and the results were compared with the atomic ratio obtained by the ICP-OES measurements (Table 7). Based on these results, the Pt:Ni:Sn and Pt:Rh:Ni:Sn atomic ratio can be estimated to 3.5:2:1 and 3:1:3:1, respectively.

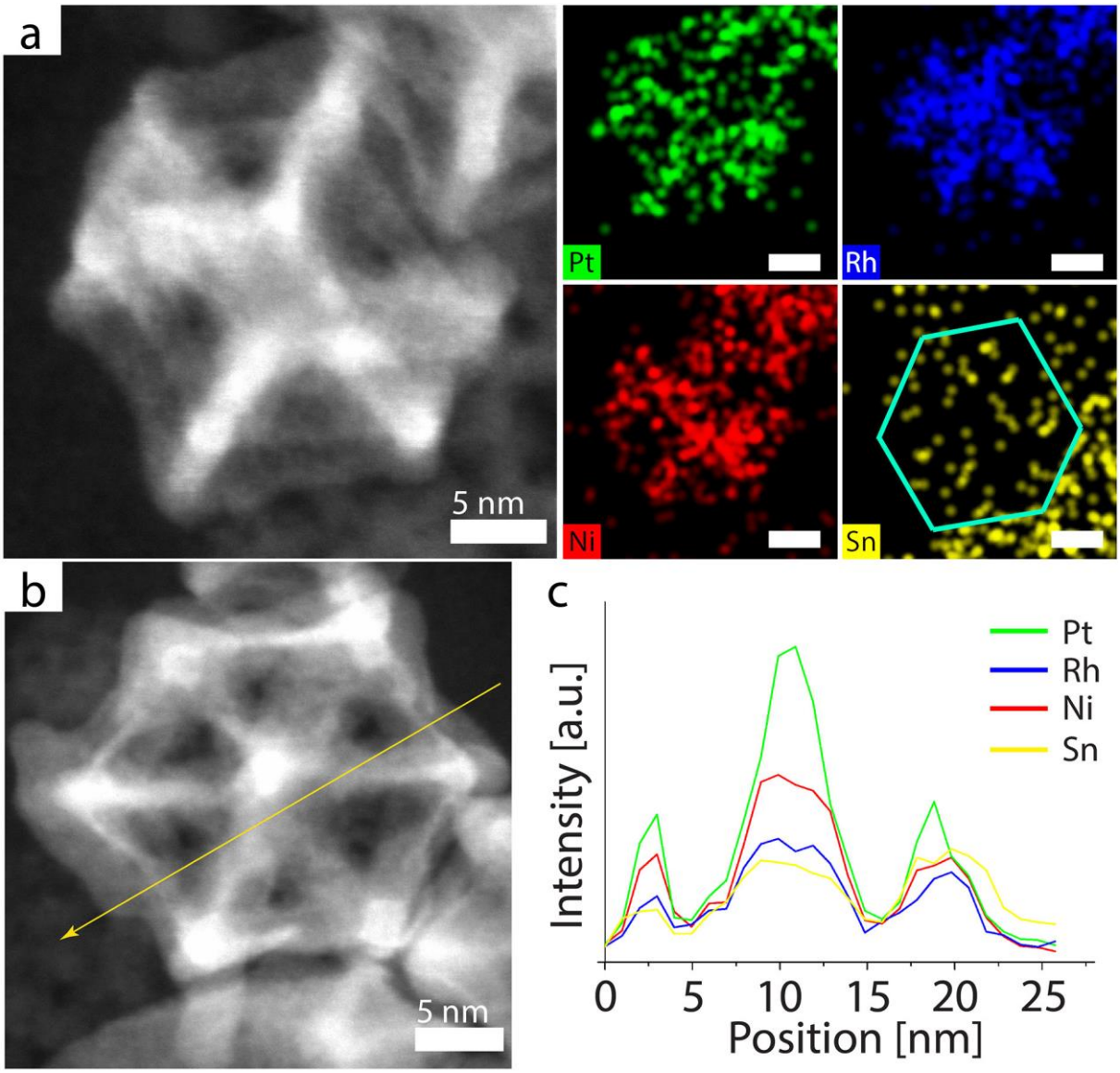

Figure 62. a) HAADF STEM image of a single PtRhNiSn nanoframe with the corresponding EDS maps; b) HAADF STEM image with the corresponding EDS line-scan through the nanoparticle.

Table 7. Comparison of the atomic composition of PtNiSn and PtRhNiSn nanoframes obtained by quantified EDS spectra and ICP-OES measurements.

	Atomic %			
	EDS		**ICP-OES**	
	$PtNi_3$	**PtRhNi**	**$PtNi_3$**	**PtRhNi**
Pt	54	38	55	39
Rh	-	12	-	12
Ni	31	33	30	35
Sn	15	17	15	14

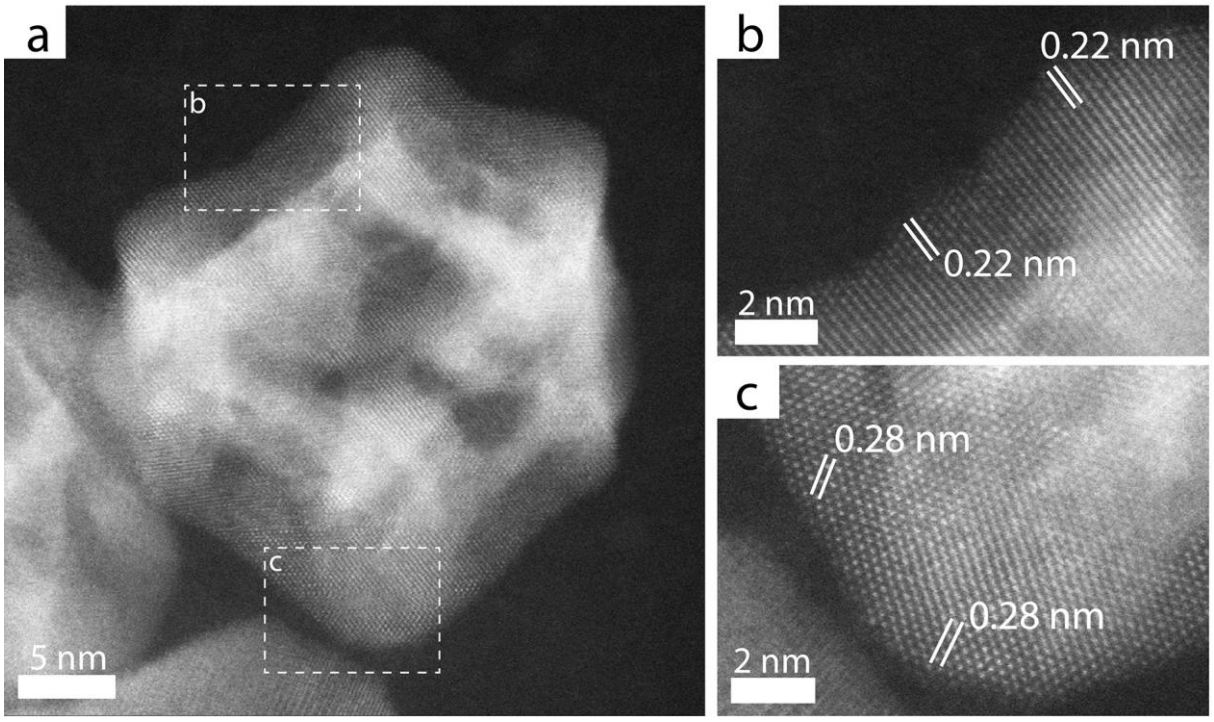

Figure 63. a) HRSTEM HAADF image of a single PtNiSn nanoframe; b) and c) magnifications of the areas marked in a), with measured lattice distances.

High-resolution HAADF STEM images of PtNiSn (Figure 63) and PtRhNiSn (Figure 64) samples confirm the crystallinity of the obtained nanoframes. The measured lattice distances between atomic planes of the PtNiSn nanoframes were found to be 0.28 nm (Figure 63c), corresponding to the (101) planes of tetragonal tin, which confirms that tin is indeed deposited on the nanoframe surface. However, the measured lattice distance of 0.22 nm (Figure 63b) is smaller than that on pure fcc Pt (111) planes and it is bigger than of pure fcc Ni (111). Thus it can be assumed that this lattice distance corresponds to the (111) planes of the PtNi alloy. Similarly, the measured lattice distance between the atomic planes of the PtRhNiSn nanoframes was found to be 0.27 nm (Figure 64c), corresponding to the (101) planes of tetragonal tin, which confirms that tin is deposited on the PtRhNi nanoframes surface. On the other hand, the measured lattice distance of 0.22 nm (Figure 63b) is smaller than that on pure fcc Pt and Rh (111) planes and it is bigger than of pure fcc Ni (111), thus it can be assumed that corresponds to the (111) planes of the PtRhNi alloy. Based on this information it can be concluded that there are sites on the PtNiSn and PtRhNiSn nanoframes, which are not covered by tin, consequently an incomplete Sn layer is formed over the nanoframes. Moreover, it is worth noticing that the Sn layer is atomically smooth.

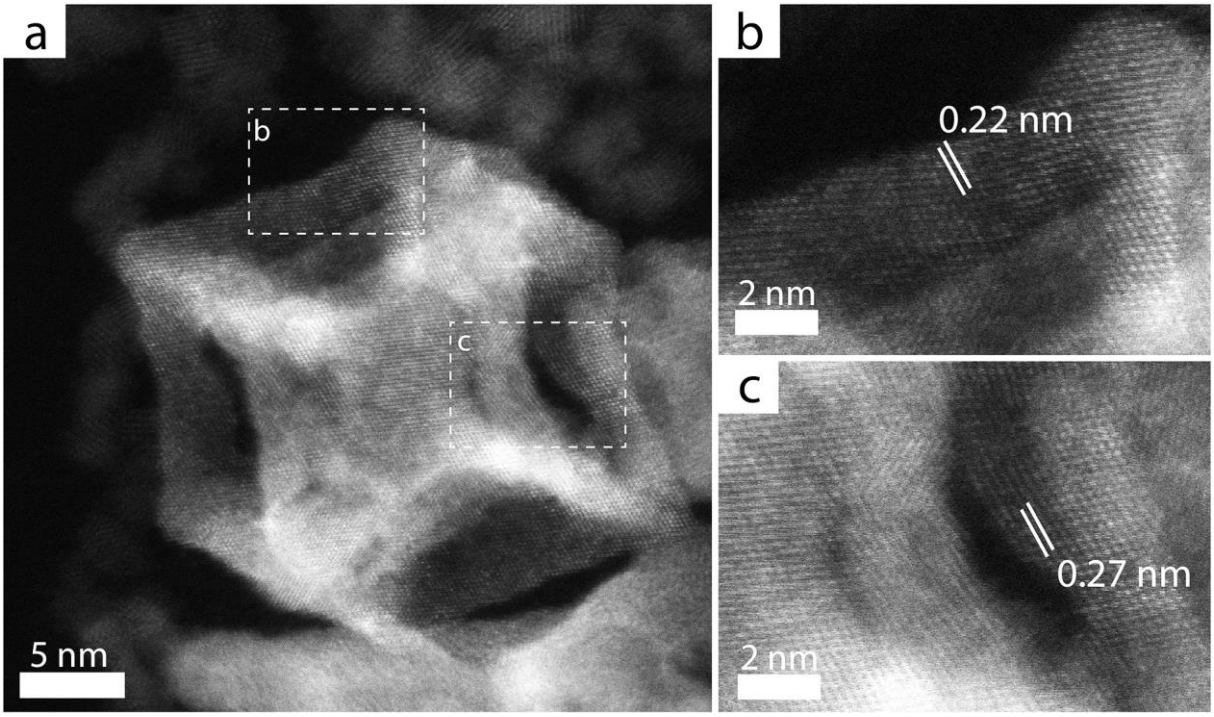

Figure 64. a) HRSTEM HAADF image of a single PtRhNiSn nanoframe; b) and c) magnifications of the areas marked in a), with measured lattice distances.

The formation of the PtNiSn and PtRhNiSn nanoframes could be explained as follows. The galvanic replacement reaction occurs between two metals with different standard reduction potentials. The metal in the template nanoparticles has a lower reduction potential, whereby it is oxidized and then dissolved in solution. The metal ions in a solution have higher reduction potentials, hence they are reduced and deposited on the template surface. In the case of the solid $PtNi_3$ and PtRhNi nanopolyhedra, with a Pt-rich phase on the edges, dispersed in a $SnCl_4$ solution, the GRR occurs between nickel atoms (E°= –0.257 V vs. SHE) from the nanoparticles core and tin ions from tin chloride solution (E°= –0.1375 V vs. SHE). Platinum and rhodium do not participate in the galvanic exchange due to their higher reduction potential compared to tin (E° = 0.755 V vs. SHE for Pt and E° = 0.758 V vs. SHE for Rh). Therefore, the expected structures to obtain after reaction are PtNiSn and PtRhNiSn nanoframes. A simplified chemical equation of galvanic displacement is as follows:

$$2Ni^0(s) + Sn^{4+}(aq) \rightarrow 2Ni^{2+}(aq) + Sn(s) \quad (27)$$

As two nickel atoms are needed to reduce one tin ion, thus the 2:1 exchange ratio explains the formation of voids in the nanoparticles core and consequently the formation of an open structure of the nanoparticles. At the same time, the deposition of tin on the resulting nanoframes increases the average size of nanoparticles. It should be noted that not all nickel from the nanoparticles is oxidized and exchanged with tin (Figure 61, Figure 62), regardless

how long the reaction takes place. These nickel atoms, which are located at the nanoparticles edges form an alloy with platinum and are thus not oxidized and dissolved, because the PtNi alloy is more stable than pure nickel [134]. Moreover, as platinum and rhodium is neutral during the galvanic displacement, even if the reaction is significantly prolonged, the nanoframes do not break up into smaller fragments, as it was reported in other studies [80], but they are being covered by tin.

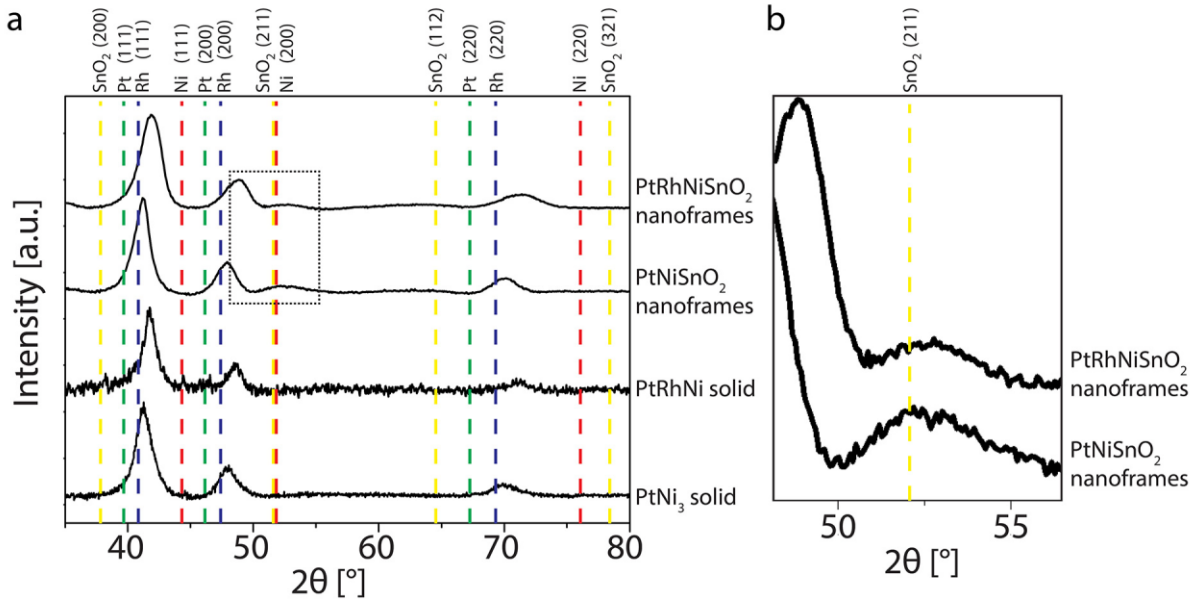

Figure 65. a) XRD diffractograms of (from bottom to top) $PtNi_3$ nanopolyhedra, PtRhNi nanopolyhedra, $PtNiSnO_2$ nanoframes and $PtRhNiSnO_2$ nanoframes; b) magnified section of the diffractogram presented in a). The standard reflexes for pure Pt – green, Rh – blue, Ni – red and SnO_2 - yellow are marked for comparison.

After galvanic replacement reaction, the PtNiSn and PtRhNiSn nanoframe samples were deposited on carbon Vulcan XC-72 and annealed in 200°C in order to remove the oleylamine residue and to oxidize Sn to SnO_2. The XRD measurements (Figure 65) show that in the case of PtNiSn and PtRhNiSn nanoframes the reflexes are shifted towards lower 2θ values in comparison to $PtNi_3$ and PtRhNi template nanopolyhedra, due to the Ni loss resulting from galvanic replacement reaction. Moreover, there is an additional reflex in both samples, which can be indexed as the SnO_2 {211} planes. This suggests that the Sn-layer was oxidized to SnO_2-layer by thermal annealing in air method [146,147], after deposition on carbon Vulcan. The presence of carbon does not allow to use high temperatures, however the temperature of 200°C is sufficient to obtain a SnO_2 layer [148].

3.3.2. Mechanism of the formation of PtNiSn and PtRhNiSn nanoframes

To better understand the kinetics of Ni and Sn exchange, the galvanic replacement reaction was stopped after 4, 13, 17 and 32 minutes in order to track the changes in nanoparticles morphology and chemical composition. Due to the fact that rhodium does not affect on GRR, all the control experiments were performed with $PtNi_3$ nanoparticles. However, these results can be extrapolated also to PtRhNi nanoparticles.

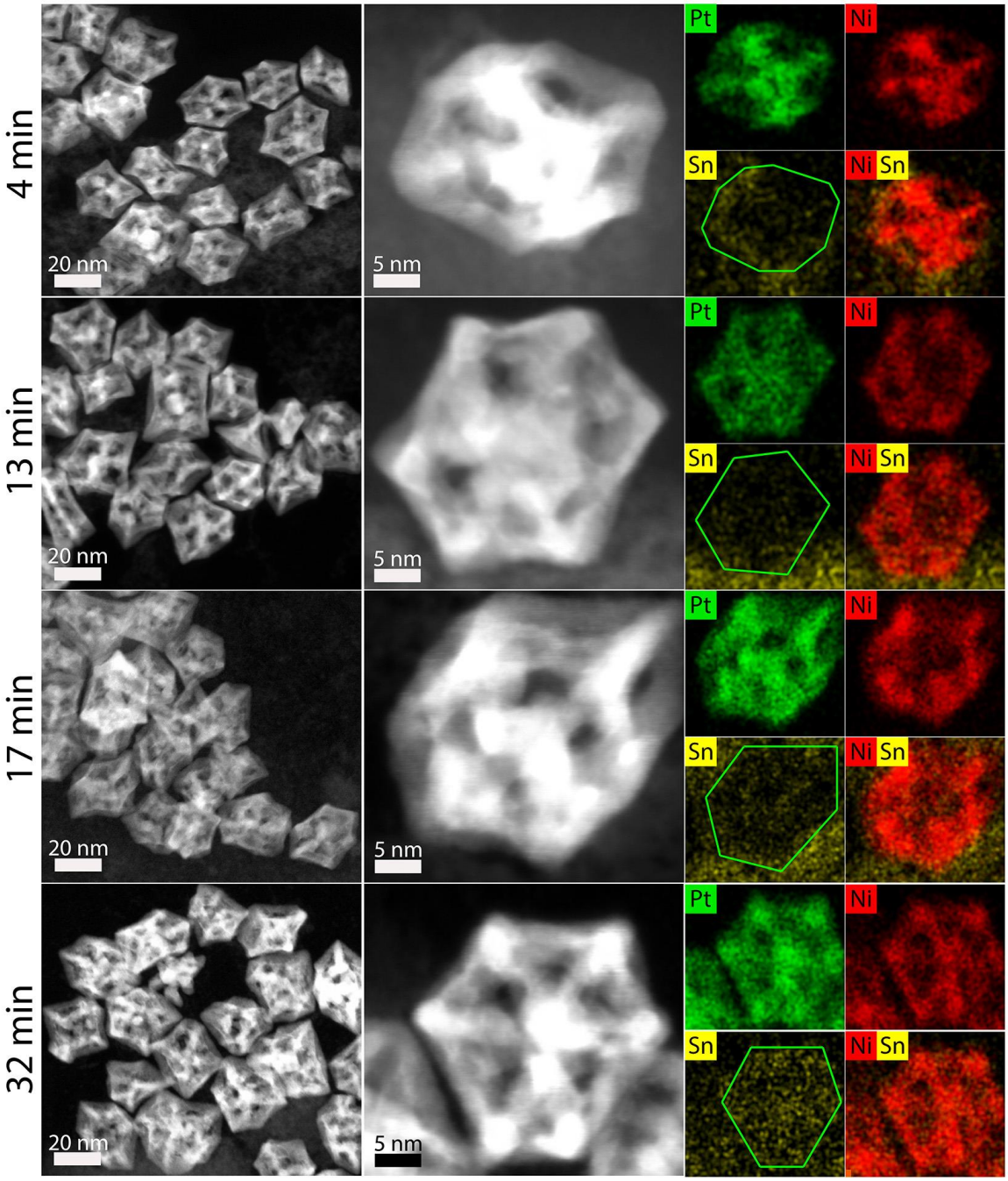

Figure 66. HAADF STEM images with the corresponding EDS elemental mappings of PtNiSn nanoparticles after 4, 13, 17 and 32 min of galvanic replacement reaction. The green frames indicate the area of nanoparticles.

Based on the HAADF STEM images and EDS maps (Figure 66), it can be seen that the nickel core dissolves and the Ni atoms diffuse out of the nanoparticles, which is followed by tin deposition after 4 minutes. At first, a void is created in the Ni core of the nanoparticles and subsequently the deposition of tin on the nanoparticle surfaces slowly occurs. After 13 and 17 minutes the tin deposition is continued and the existing void is slightly expanding as a result of the nickel core dissolution and the Ni atoms diffusing out of the NPs. After 32 minutes, the galvanic replacement reaction was stopped by centrifugation and washing with ethanol to avoid blocking the platinum active sites by the excess of tin, which was continuously deposited on the nanoframes.

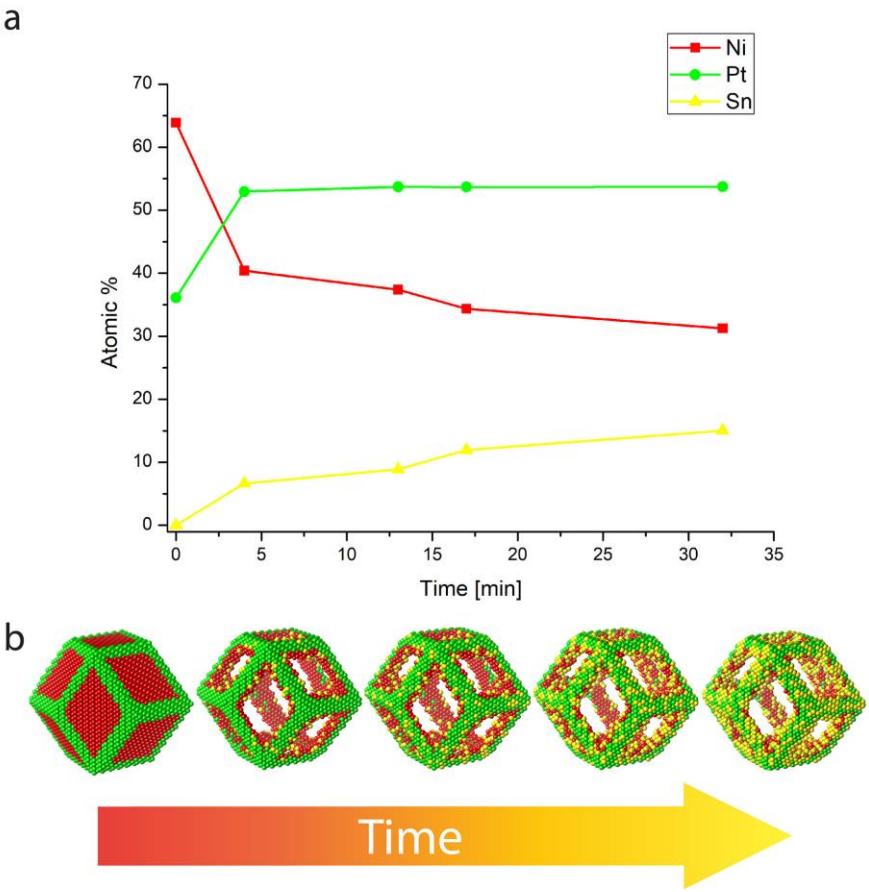

Figure 67. a) Correlation between the content of Pt, Ni, Sn (as atomic ratios) and the GRR time. The atomic percent values were plotted based on the results from quantified EDS maps for samples after 4, 13, 17 and 32 min of galvanic replacement reactions; b) schematic representation of the galvanic replacement reaction over time.

The change in chemical composition of the nanoparticles as a function of time, obtained from EDS data, is shown in Figure 67a. It can be seen that the nickel content in the nanoparticles is mainly decreasing during the first 4 minutes of the galvanic replacement reaction. This suggests that during this time most of the nickel atoms are oxidized and dissolved, which

would explain the void formation inside the nanoparticles. This process is schematically shown in Figure 67b. The results show that the removal of nickel is fast, while the deposition of tin is relatively slow. The explanation for this may be the presence of Cl^- ions in the solution. These ions, like other halide ions (Br^-, I^-), are strong oxidative etchants when combined with oxygen [127,129]. Thus the combination of Cl^-/O_2 causes corrosion of nickel atoms resulting in their removal from the core of nanopolyhedra. To exclude the dominant role of oxidative etching in void formation, we performed a control experiment, in which the $PtNi_3$ solid nanoparticles were suspended in a mixture of ethylene glycol and chloroform in the absence of Sn precursor in air atmosphere (Figure 68). After one hour, the obtained nanoparticles are rather porous than hollow, which suggests that no nanoframes were obtained. This indicates that oxidative etching indeed affects the nickel dissolution, however it is not the main process causing nickel removal. The oxidative etching in very slow at room temperature [17], therefore the GRR is dominant in the formation of PtNiSn nanoframes and oxidative etching could be a supporting process of removing Ni atoms.

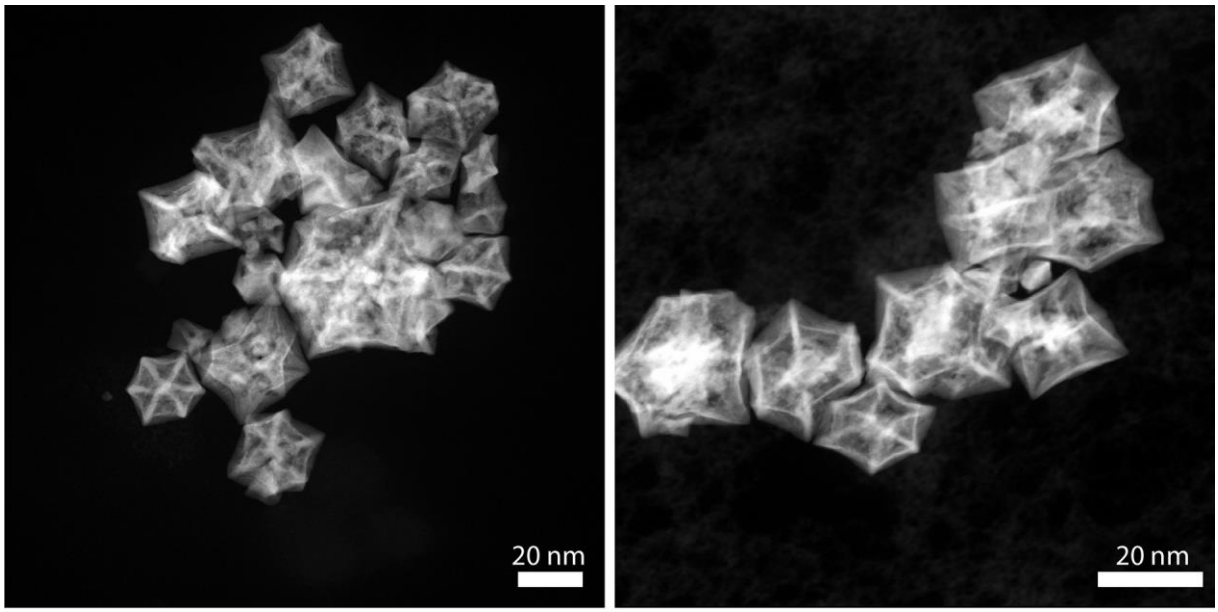

Figure 68. $PtNi_3$ solid nanoparticles after ethylene glycol with chloroform treatment for 1 hour.

Additionally, in the case of the GRR between Ni atoms and Sn^{4+}, the impact of Kirkendall effect causing faster diffusion of nickel atoms cannot be excluded. This phenomenon is associated with the difference in diffusion rates of atoms and ions participating in the reaction [149,150]. Since nickel atoms are smaller and lighter than tin atoms, they diffuse faster [151]. Because deposition of tin on the surface is slow, the resulting Sn layer is smooth [152]. In summary, nickel atoms are subjected to two processes: galvanic displacement with tin and

oxidative etching due to the presence of chlorine ions and oxygen, which accelerate their oxidation and dissolution. Unfortunately, due to the high reaction rate, it is impossible to observe the early stages of the reaction under these conditions.

Interestingly, although the reaction occurs in ethylene glycol (EG), which is a strong reducing agent, nor Sn or SnO_2 nanoparticles are synthesized. This is explained by the fact that the galvanic replacement reaction takes place at room temperature, and the nucleation of nanoparticles requires energy [153]. It is worth mentioning, that the $PtNi_3$ nanopolyhedra after the synthesis are capped by oleylamine, which is also a reducing agent. However, since it is present in small quantities in the sample and it is a mild reducing agent [154], therefore its reducing properties can be neglected.

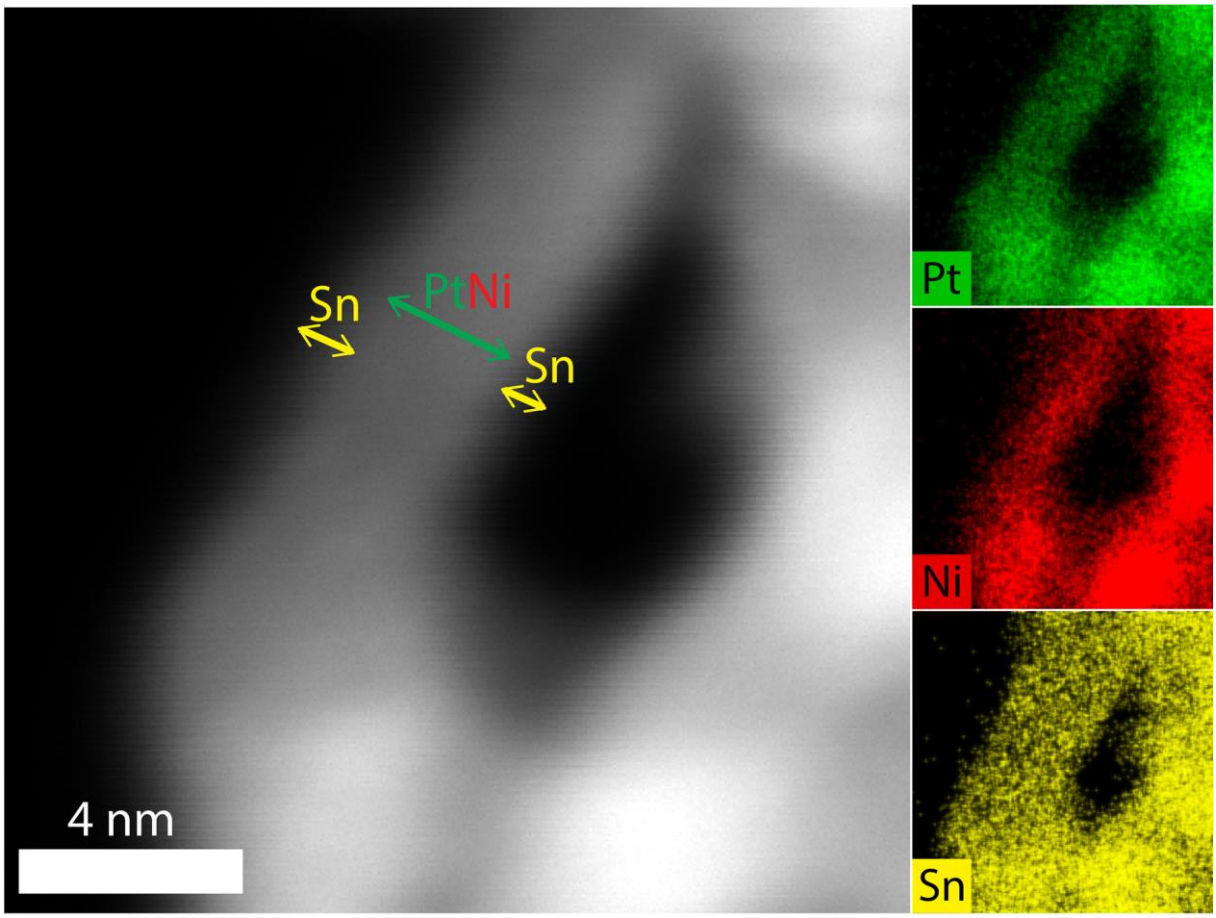

Figure 69. HAADF STEM image and the corresponding Pt, Ni, and Sn EDS maps of an edge of a PtNiSn nanoframe.

In order to verify the deposition sites of tin, the galvanic replacement reaction was prolonged to 10 hours to obtain a thicker Sn layer on the Pt-rich nanoframe. Based on the EDS maps (Figure 69), it can be noticed that tin is deposited not only inside the nanoframes, where Sn replaces Ni atoms, but also on the outer side of the Pt frame.

It is worth noticing that, after 10 hours of reaction the Sn layer covered all the Pt sites, preventing platinum from participating in any catalytic reaction. To better illustrate the coverage of Pt by Sn layer, EDS maps were acquired at several tilt angles (Figure 70). These maps confirm that platinum forms a frame and the Sn layer covers the entire surface of the Pt nanoframe. The Sn-deposition inside the frames is easily attributed to the fact, that tin undergoes galvanic exchange with nickel, replacing it in the nanoparticle core. On the other hand, platinum does not participate in the galvanic exchange, yet, the outer surface of nanoframe, which is rich in platinum, is also coated with a tin layer. An explanation of this phenomenon may be the use of tin excess with respect to the number of nickel atoms and the additional use of EG as a solvent. Nickel atoms, after oxidation, are able to reduce only part of the tin ions, which deposit on the inner frames surfaces. The rest of the tin ions are reduced by EG, so they can deposit on the outer surface of the $PtNi_3$ template forming a thin and incomplete Sn layer. As the reaction time increases, more tin is deposited, until the Sn layer covers the entire internal and external surface of nanoframes, blocking thus the Ni atoms, which could reduce tin ions.

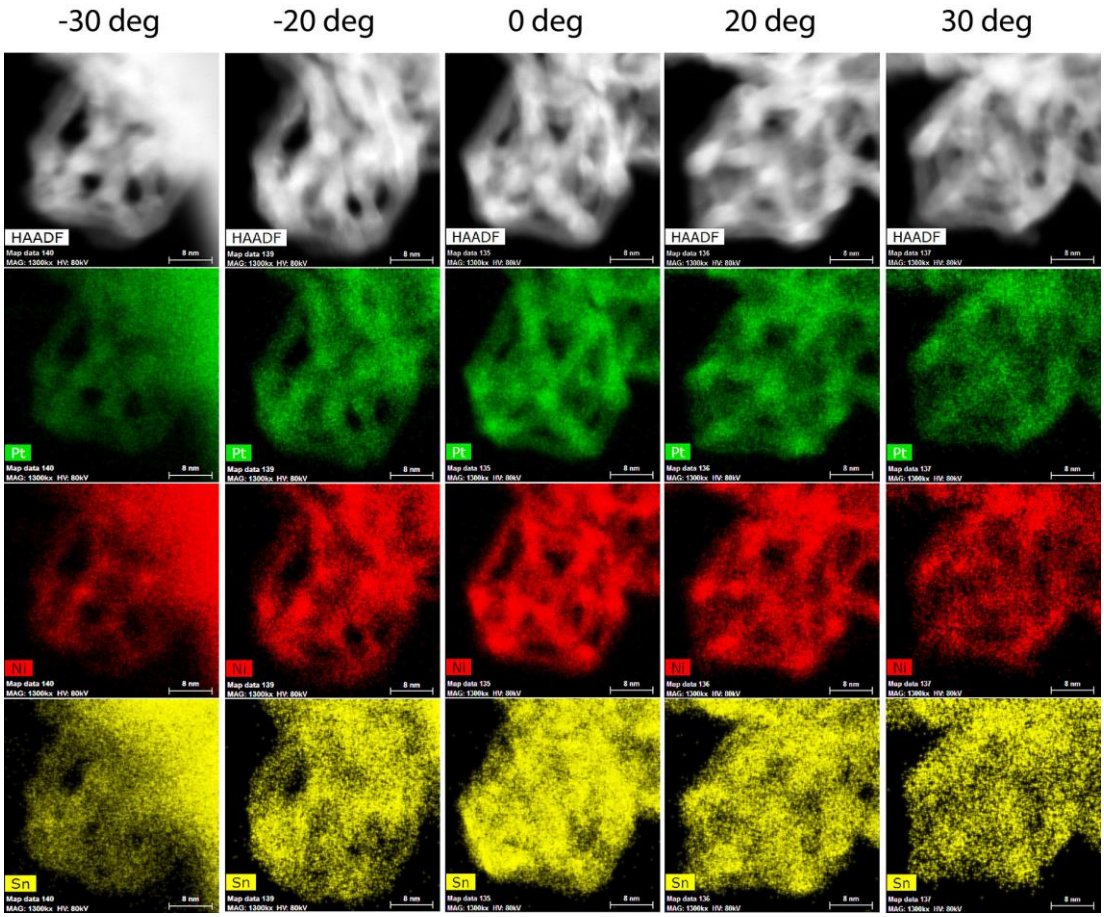

Figure 70. EDS tilt series of PtNiSn nanoframes after 10 h of galvanic replacement reaction. The scale bars correspond to 8 nm.

Based on STEM and EDS observations of intermediate states of PtNiSn nanoframes during galvanic replacement reaction, two mechanisms of ion exchange can be distinguished. The first one is simultaneous diffusion of nickel from the core of the solid nanoparticles and deposition of the tin on the surfaces of the nanoframes as illustrated in (Figure 71a). As it can be seen, the signal from nickel is most intensive in the core of nanoparticle, but not in the center of the core, where the void begins to form. Moreover, Ni is also present around the nanoparticle. In contrast, the signal from tin is the most intensive around the nanoparticle, but some tin is already deposited on the surface of the nanoparticle. This suggests that the exchange of nickel and tin takes place simultaneously. This could be explained by the presence of ethylene glycol, which is a strong reducing agent, whose impact will be discussed in details below. The second mechanism derived from Figure 71b is the initial oxidation and dissolution of nickel followed by tin deposition. Indeed the EDS mapping reveals intensive nickel signal, both, inside and outside of the nanoparticles, but the signal from tin is very low. This may be explained by the fact, that the dissolution of the template atoms is faster on facets with the highest surface free energy, while the deposition of atoms occurs first on facets with lower surface free energy [74]. Since solid template $PtNi_3$ polyhedra are enclosed by 12 {110} facets, which have the highest surface free energy among the low-index facets, the nickel dissolution proceeds faster than tin deposition. In conjunction with the previously discussed impact of the oxidative etching resulting from the presence of Cl^-/O_2, a faster dissolution of nickel than tin deposition occurs.

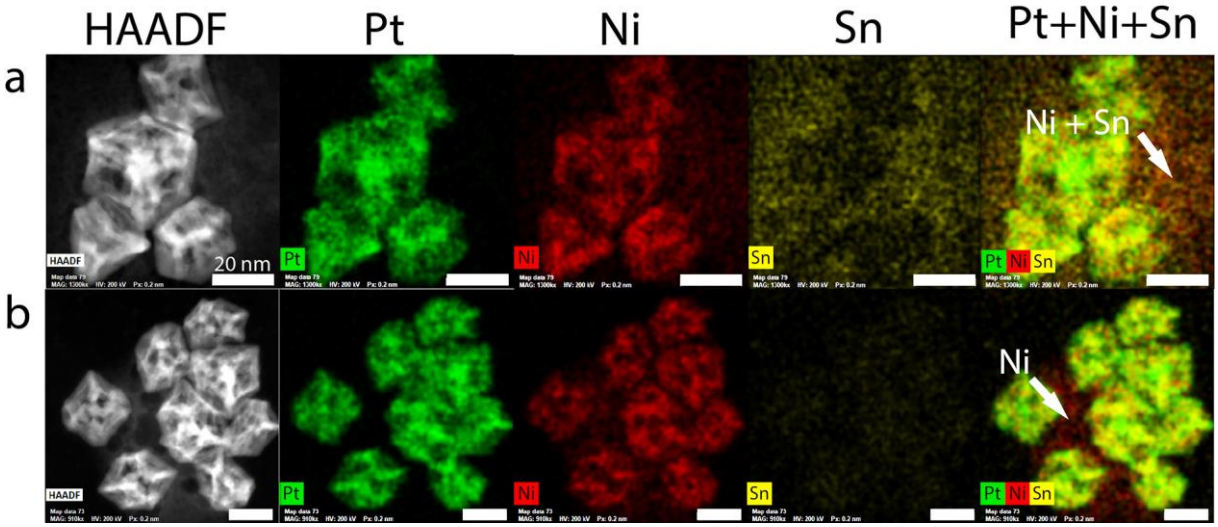

Figure 71. STEM HAADF images with the corresponding EDS maps showing (a, b) simultaneous diffusion of nickel atoms out of the nanoparticles and tin deposition on the nanoparticles and (c, d) diffusion of nickel from out of the nanoparticles without tin deposition. Scale bars are 20 nm.

3.3.3. Control experiments revealing the effect of the solvent and tin concentration on the reaction course

Additional experiments were carried out to investigate the effect of the solvent type on the GRR and the influence of tin salt concentration on the kinetics of the process. In the first experiment, instead of ethylene glycol, water was used as a solvent. This allowed to verify, how replacing a strong reducing agent (i.e. EG) with water affects the rate of the GRR. STEM HAADF images and EDS maps (Figure 72a) reveal that the galvanic exchange process progress is slower, both in terms of oxidation and dissolution of nickel, as well as in reduction and deposition of tin. After 30 min of reaction in water, only pores are formed in the cores of the nanopolyhedra. The average atomic ratio of Pt:Ni:Sn equal to 15:43:42 reacted in water, confirms that the reaction is not completed. Conversely, when the reaction proceeds in EG, after 30 minutes the nanopolyhedra transform into hollow nanoframes. High nickel content confirms that the oxidation and dissolution of the nanopolyhedra core is still in progress. On the other hand, high tin content originates from the presence of non-reduced tin chloride. Indeed, the EDS Sn signal is located everywhere in the sample, not only at the surface of nanoparticles. This indicates that the ethylene glycol accelerates deposition of tin on nanoframes, but also affects the oxidation and dissolution of nickel. Tin ions (IV) are reduced according to the equation 28 and equation 29:

$$Sn^{4+}(aq) + 2e^{-} \rightarrow Sn^{2+}(aq) \quad (28)$$

$$Sn^{2+}(aq) + 2e^{-} \rightarrow Sn\,(s) \quad (29)$$

Both of these reactions have a relatively low standard reduction potential (+0.151 V and -0.1375 V vs. SHE, respectively), so tin ions are difficult to reduce. Ethylene glycol, by supporting the reduction of Sn ions, facilitates the oxidation and dissolution of nickel atoms. It could be expected that using water should increase the occurrence of oxidative etching, due to the presence of oxygen in water molecules. However, as shown on Figure 72a, the presence of water slows down the formation of nanoframes. This may be due to the fact, that increasing the concentration of oxygen without increasing the concentration of Cl^- is insufficient to increase the rate of obtaining nanoframes.

The second experiment was performed to evaluate, how reducing the concentration of tin chloride from 1M to 0.1M will affect the rate of the galvanic replacement reaction. The EDS maps (Figure 72b) show that the galvanic exchange was slower compared to higher concentrations of tin salt. After 30 minutes of the reaction, the atomic ratio of Pt:Ni:Sn was equal to 20:64:16, which suggests that GRR is not completed due to high nickel content.

These results indicate that after reducing 10 times the concentration of $SnCl_4$, the reaction rate was decreased, similarly as when replacing EG with water. This could be explained with the collision theory, according to which lower concentration of reagents generates fewer collisions between reagents and thus the reaction rate decreases. In both cases, either replacing EG with water or reducing the concentration of tin chloride, has slown down the reaction sufficiently to capture the initial reaction stage. HAADF STEM images and EDS maps show, that at the surface of the nanoparticles, first voids are formed, which later coalesce to reduce the surface energy [150]. This is in accordance with previous studies on the mechanism of the GRR [155–157]. On the other hand, in other studies [142,158] during galvanic replacement pores are formed preferentially at the corners than on facets or edges, due to the fact, that low-coordination sites have high surface energy, therefore the replacement would first start there. In the current case, because corners and edges are composed of platinum, which is inert during galvanic replacement, pores are formed on nickel facets (Figure 72), despite that they are less active than the corners.

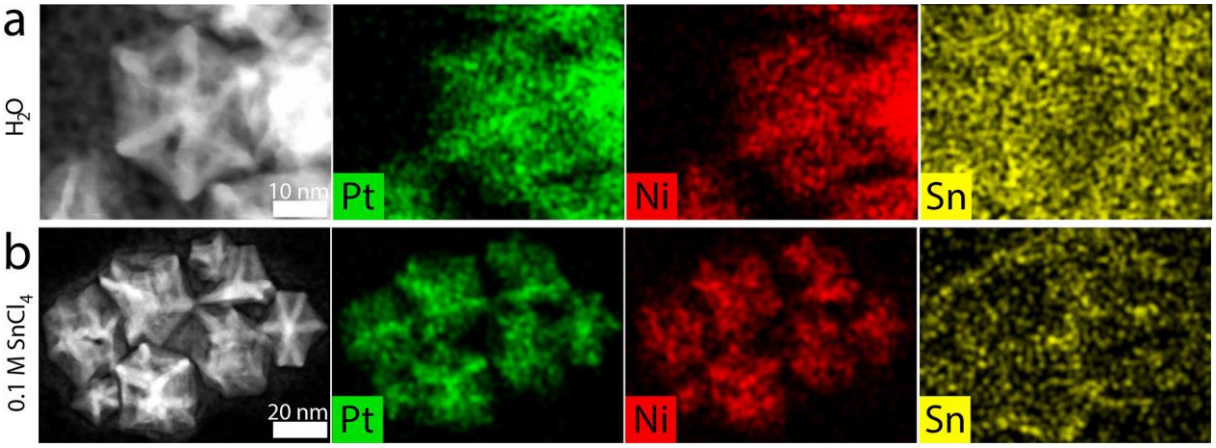

Figure 72. EDS maps of PtNiSn nanoframes after galvanic replacement performed in a) water and b) in ethylene glycol with lower concentration of $SnCl_4$ (0.1 M vs. 1.0 M before).

3.4. Electrochemical characterization of the obtained nanocatalysts

All obtained nanoframes were deposited on carbon Vulcan XC-72R resulting in obtaining the following nanocatalysts: Pt_3Ni/C and PtRhNi/C nanoframes, SnO_2@Pt_3Ni/C and SnO_2@PtRhNi/C, PtNiSnO_2/C GR and PtRhNiSnO_2/C GR. Nanocatalysts with an abbreviation "GR" refer to nanoframes obtained by galvanic replacement reaction to distinguish from nanoframes decorated with SnO_2 NPs (SnO_2@Pt_3Ni/C and SnO_2@PtRhNi/C). To simplify, the "/C" part in the name of samples, which refer to

nanoparticles deposited on carbon, will be omitted in text. However, note that all samples tested electrochemically were deposited on carbon (Figure 73).

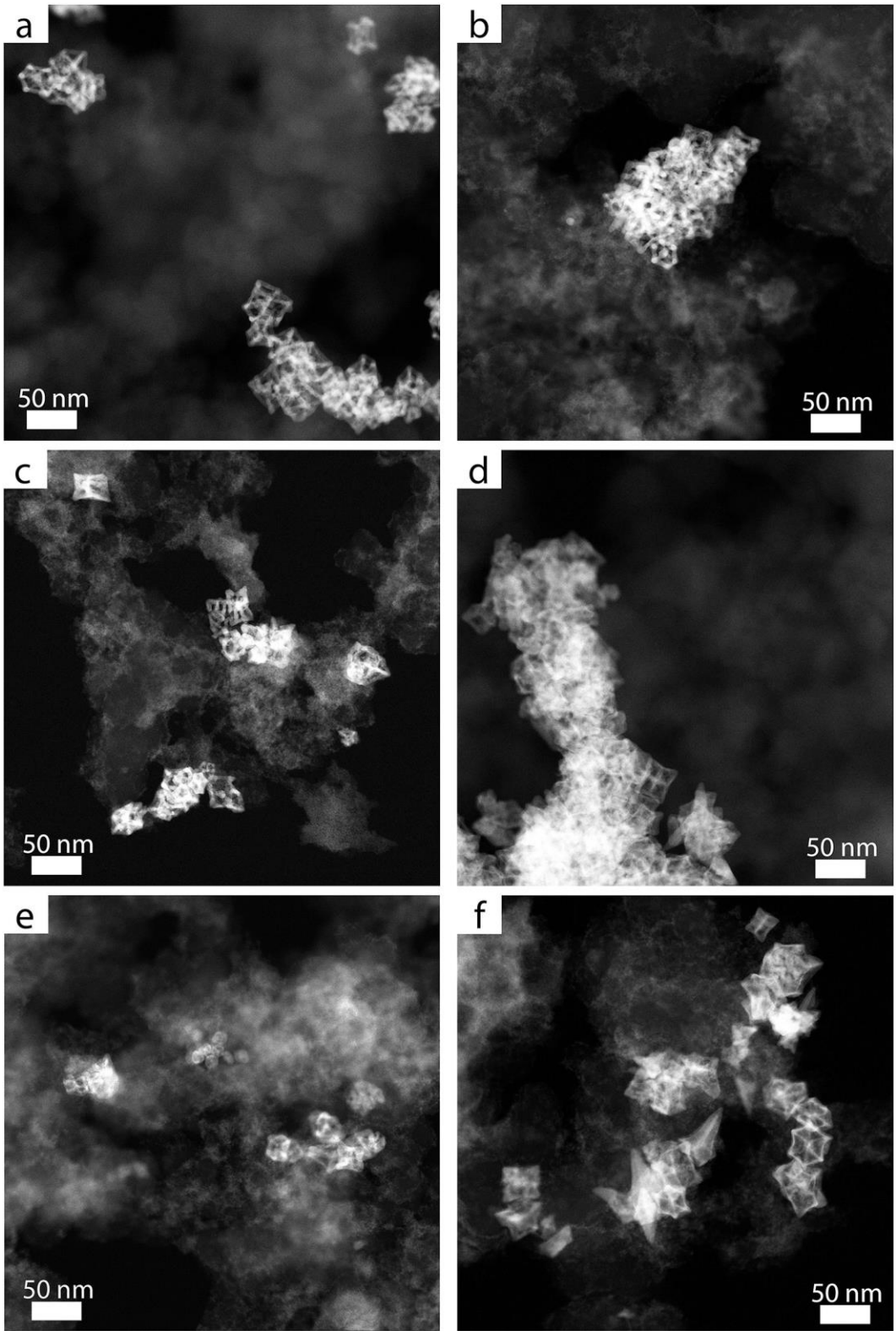

Figure 73. HAADF STEM images of a) Pt_3Ni nanoframes; b) SnO_2@Pt_3Ni nanoframes; c) $PtNiSnO_2$ nanoframes; d) PtRhNi nanoframes; e) SnO_2@PtRhNi nanoframes and f) $PtRhNiSnO_2$ nanoframes deposited on carbon Vulcan XC-72R.

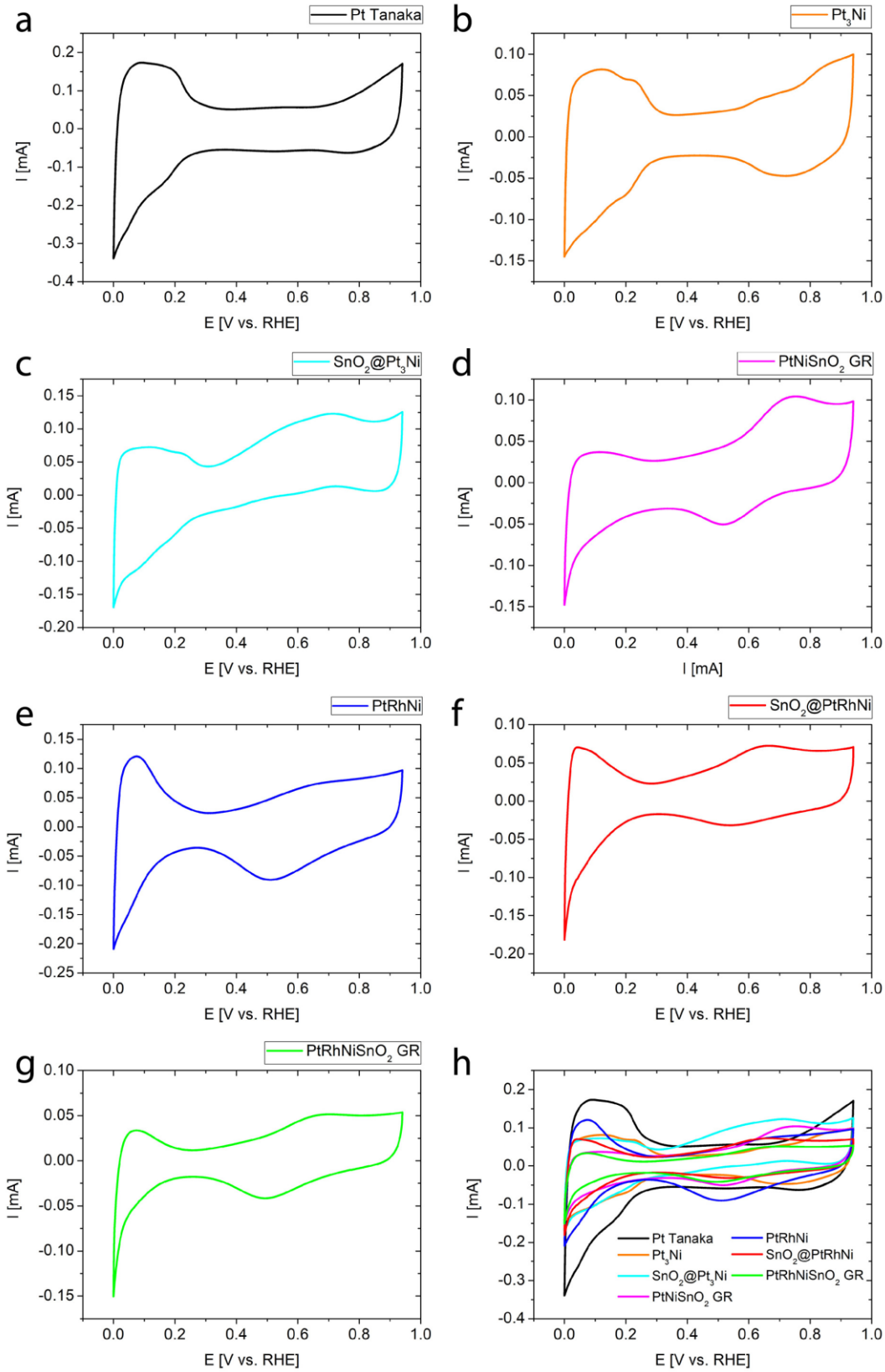

Figure 74. CV profiles of a) Pt Tanaka; b) Pt_3Ni nanoframes; c) SnO_2@Pt_3Ni nanoframes; d) $PtNiSnO_2$ GR nanoframes; e) PtRhNi nanoframes; f) SnO_2@PtRhNi nanoframes; g) $PtRhNiSnO_2$ GR nanoframes deposited on carbon Vulcan XC-72R and h) their overlap. All CVs were recorded in Ar-purged 0.1 M $HClO_4$ solution, at a scan rate of 20 mV s^{-1}.

After deposition on the Vulcan XC-72R, the nanoframes-based catalysts were electrochemically tested and compared with commercial 2 nm spherical Pt catalysts (Pt/C Tanaka). First, based on the CVs measurements (Figure 74), it can be seen that in the samples containing SnO_2, both in the form of nanoparticles and thin layer, except hydrogen desorption peak (around 0 – 0.25 V), there is also a peak around 0.6 – 0.8 V. This may be originating from the oxygen adsorption/desorption, from the dissociation of water on SnO_2 [159,160]. Therefore this is another confirmation of the presence of SnO_2 in samples. Based on hydrogen adsorption peaks the platinum ECSA was calculated and converted to platinum SSA (Table 8). As can be seen, the highest ECSA is for Pt Tanaka, while the lowest is for $PtRhNiSnO_2$ GR sample. However, after dividing ECSA by mass of Pt, the specific surface area is obtained, which is more accurate to describe the nanocatalysts. By comparing the specific surface area of the all tested catalysts it turns out that the highest value is 405 cm^2 mg^{-1} Pt for Pt_3Ni nanoframes, while Pt Tanaka has 297 cm^2 mg^{-1} Pt, which is the third greatest value after Pt_3Ni and PtRhNi nanoframes. Interestingly, the Pt_3Ni and PtRhNi nanoframes have higher SSA than SnO_2@Pt_3Ni, SnO_2@PtRhNi, $PtNiSnO_2$ GR and $PtRhNiSnO_2$ GR. This could be explained by the fact that SnO_2 deposited on nanoframes, either in form of nanoparticles or thin layer, decreases the surface of platinum and in consequence the platinum SSA [161]. It is noticeable that the lowest ECSA and SSA has the sample $PtRhNiSnO_2$ GR, which is more than four times lower than for $PtNiSnO_2$ GR (47.5 cm^2 mg^{-1}Pt vs. 219 cm^2 mg^{-1}Pt, respectively). This may be astonishing, due to the fact that the SnO_2 content in both samples is similar (15 at% vs. 17 at% for $PtNiSnO_2$ GR and $PtRhNiSnO_2$ GR, respectively). However, it is hard to determine the thickness of the SnO_2 layer on the nanoframes, it cannot be excluded that for $PtNiSnO_2$ GR the tin oxide layer is thicker, therefore it occupies a smaller area, while the oxide layer on PtRhNi nanoframes is thinner and covers larger area.

Table 8. Comparison of Pt ECSA and Pt ECSA per Pt mg for all tested catalysts.

	Pt Tanaka	Pt_3Ni	SnO_2@Pt_3Ni	$PtNiSnO_2$ GR	PtRhNi	SnO_2@PtRhNi	$PtRhNiSnO_2$ GR
Pt ECSA [cm^2]	5.65	3.24	2.31	1.75	2.95	1.44	0.38
Pt SSA [cm^2 mg^{-1}Pt]	297	405	289	219	369	180	47.5

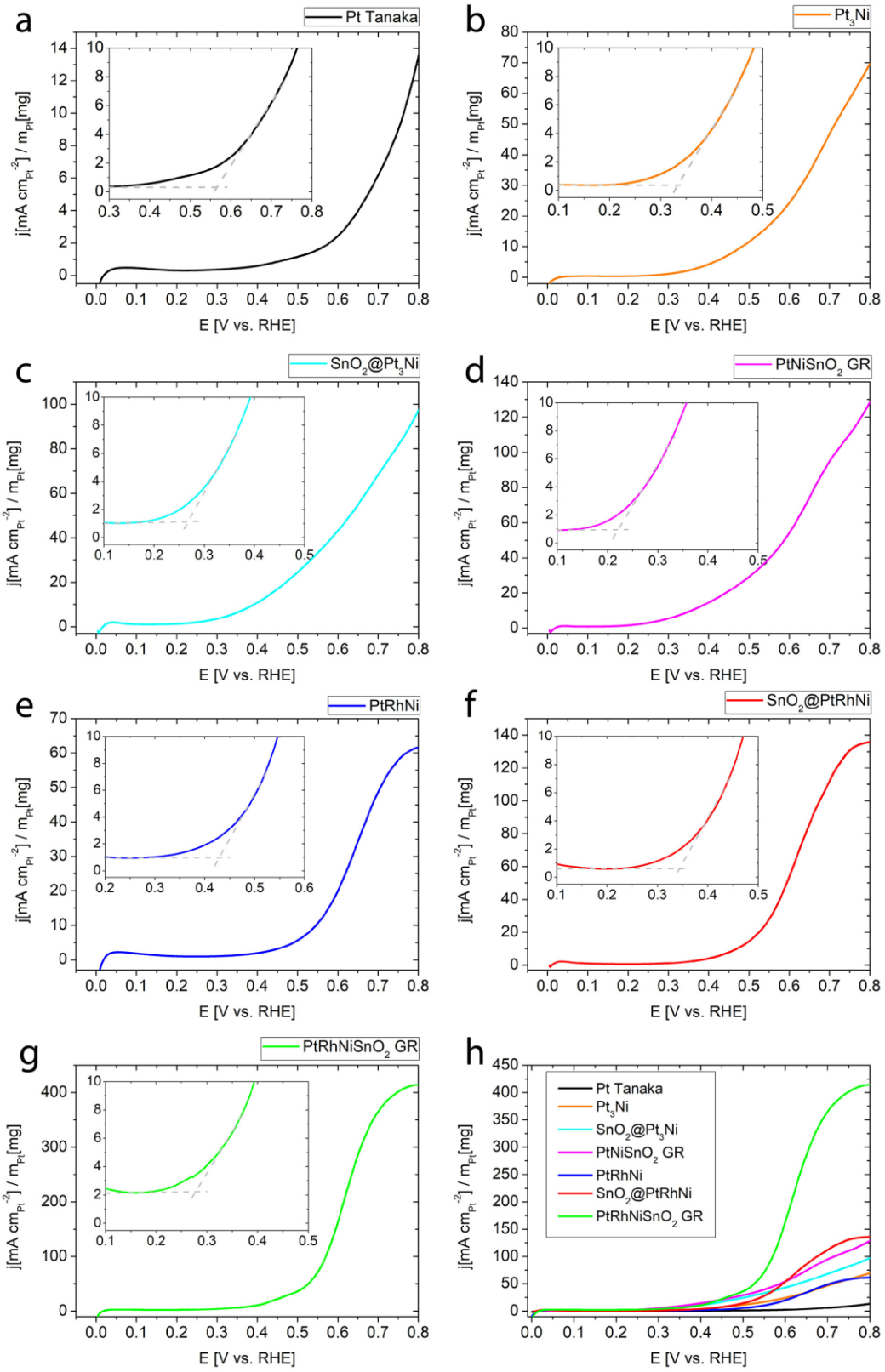

Figure 75. First EOR forward scan of a) Pt Tanaka; b) Pt_3Ni nanoframes; c) SnO_2@Pt_3Ni nanoframes; d) $PtNiSnO_2$ GR nanoframes; e) PtRhNi nanoframes; f) SnO_2@PtRhNi nanoframes; g) $PtRhNiSnO_2$ GR nanoframes deposited on carbon Vulcan XC-72R and h) their overlap. Insets show the onset potential region for each catalyst. All curves were recorded in 0.1 M $HClO_4$ + 0.5 M C_2H_5OH solution at a scan rate of 10 mV s^{-1}.

Next, the EOR activities for all catalysts were evaluated. Based on the polarization curves of all the catalysts in ethanol containing electrolyte (Figure 75), it can be seen that the $PtRhNiSnO_2$ GR nanocatalysts exhibit the highest EOR activity among all the tested samples. At a potential of 0.65 V (Figure 76), it reaches a 3 times higher value of current density per mg of Pt than SnO_2@PtRhNi catalyst, with the second highest value of current density per mg of Pt, and near 71 times higher than Pt Tanaka.

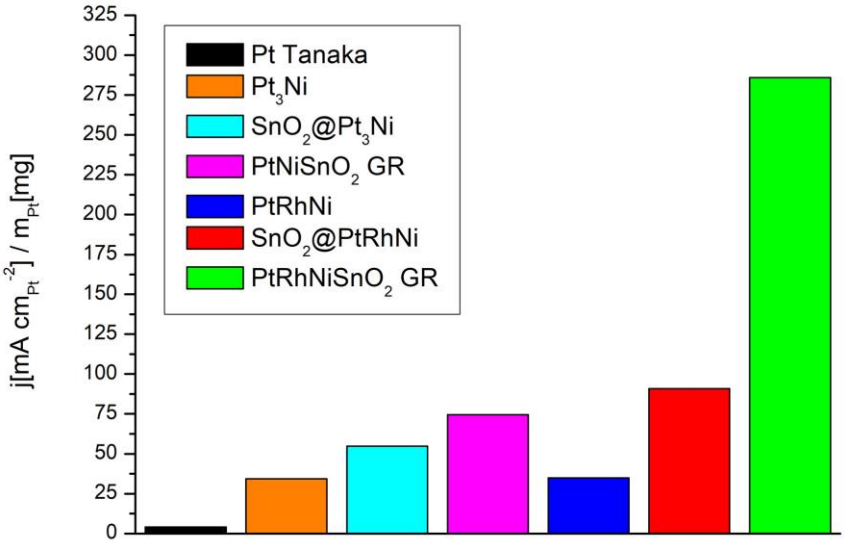

Figure 76. Activity of all tested catalysts at a potential of 0.65 V vs. RHE.

Also, from the EOR curves it can be concluded that the addition SnO_2 NPs to nanoframes or deposition of SnO_2 as a thin layer on the nanoframes increases the EOR efficiency. This is due to the fact that SnO_2 strongly adsorbs water on its surface instead of the Pt and Rh surfaces, making them available to adsorbing ethanol. Moreover, by dissociation of water on its surface, SnO_2 provides OH species, which help in oxidation of CO to CO_2 [23,162,163], this is the so-called bifunctional effect [19,164].

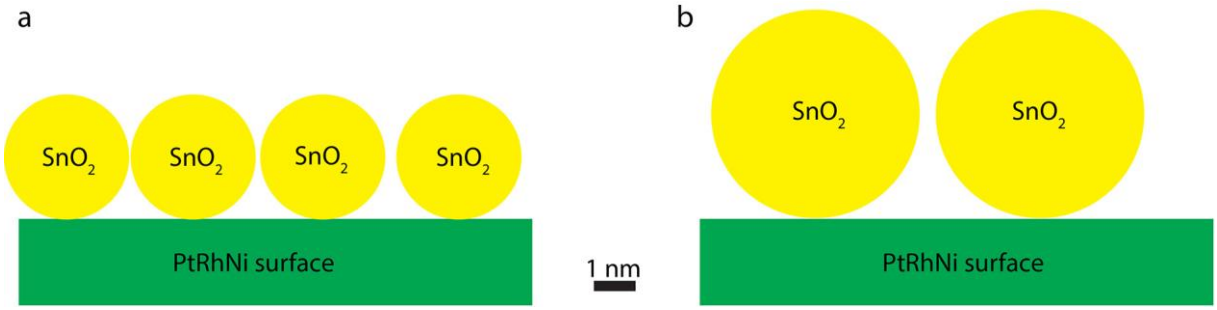

Figure 77. Schematic representation of a) small 3 nm SnO_2 NPs and b) larger 5 nm SnO_2 NPs on the nanoframes surfaces.

The presence of interfaces between the metal (Pt) and oxide (SnO_2) nanoparticles also could induce charge transfer, which could enhance the catalytic performance [165]. However, it is accepted that interactions between metals and oxides are highly local, as they occur at distances below 1 nm from the interface [166]. Therefore, small (about 3 nm) SnO_2 NPs instead larger, e.g. 5 nm, or a thin incomplete SnO_2 layer were used in order to maximize the number of interface sites (Figure 77). Small sizes of SnO_2 NPs not only provide more interface points between metal and oxide than the larger nanoparticles, but also play an important role in CO_2 generation during ethanol oxidation. Based on the DFT calculations performed by the Adzic group [167], it can be concluded that binding energy of the adsorbed OH species depends on size of SnO_2. They showed that small, about 2 nm SnO_2 NPs provide weaker interactions between SnO_2 surface and OH species, than larger 20 nm SnO_2 NPs. This leads to easier release of adsorbed OH species from SnO_2 surface, and in consequence causes a more efficient oxidation of CO adsorbed on Pt surface to CO_2. It is worth noticing that the presence of nickel atoms in the catalysts also affects on EOR. According to the DFT calculations performed by Nørskov *et al*. [168–170], alloying platinum with nickel atoms down-shifts the Pt d-band center. This so-called ligand effect leads to the weaker bonding of the adsorbed molecules by the Pt surface, and prevents poisoning of the catalysts [171]. Moreover, Ni atoms are oxophilic, and similarly like SnO_2, provide active OH species, which oxidize the molecules adsorbed on the surfaces [29,172,173].

By comparing the respective pairs of catalyst i.e. Pt_3Ni vs. PtRhNi, SnO_2@Pt_3Ni vs. SnO_2@PtRhNi and PtNiSnO_2 GR vs. PtRhNiSnO_2 GR, it can be concluded that the addition of rhodium also affects the EOR. Except the pair Pt_3Ni vs. PtRhNi, where the current density per mg Pt is almost the same, the catalysts with rhodium exhibit higher current densities per mg Pt than their counterparts without rhodium. This could be explained by the fact that rhodium facilitates the breaking of C-C bond in the ethanol molecule, which is confirmed by both experimental methods and DFT calculations [15,16,174,175]. In “ideal” EOR nanocatalysts, a complete oxidation of ethanol to CO_2 occurs, which generates 12 electrons and ensures the highest efficiency of the reaction. However, due to the difficulty of breaking the C-C bond in the ethanol molecule, instead of CO_2, acetic acid or acetaldehyde are obtained with simultaneous generation of 4 or 2 electrons [23]. The presence of rhodium allows to obtain CO_2 as a product and as a consequence, enhances the yielding of the current. However, the presence of rhodium in the studied PtRhNi nanoframes, without SnO_2 does not enhance the ethanol oxidation reaction in comparison to Pt_3Ni nanoframes, which is consistent with studies of other groups [23,27]. According to Adzic *et al.* [15,162] this is due

to the electronic interactions of Pt and Rh, the rhodium donates d-band electrons to platinum, which fill the Pt d-band. In consequence, the catalysts stronger binds the adsorbed molecules, such as CO, which poison the surface of Pt and lower its activity. As it was mentioned before, the addition of SnO_2 facilitates removing the adsorbates and compensates the poisoning caused by rhodium.

Another important parameter describing the activity of the catalysts is the so-called onset potential, which is defined as the value of potential at which the current rapidly rises. The lower is the onset potential, the faster the reaction starts. Among all tested catalysts, the lowest onset potential have the catalysts obtained by the galvanic replacement reaction (Table 9), both $PtNiSnO_2$ GR and $PtRhNiSnO_2$ GR (0.22 and 0.26 V vs. RHE, respectively). However generally, all of the frames-based nanocatalysts have lower onset potentials than Pt Tanaka. Nevertheless, it can be noticed that nanoframes-based nanocatalysts without rhodium have a lower onset potential, than the nanoframes with rhodium. This may be attributed to the lower content of platinum, at which adsorption and dehydrogenation of ethanol occurs [15,162]. Also, a decrease of the onset potential was observed for the nanoframes decorated with SnO_2 NPs and nanoframes after galvanic replacement, relative to nanoframes without SnO_2. According to previous studies [163,176,177], the presence of the SnO_2 decreasing the onset potential due to the above mentioned bi-functional effect.

Table 9. Comparison of onset potentials for all tested catalysts.

	Pt Tanaka	Pt_3Ni	SnO_2@Pt_3Ni	$PtNiSnO_2$ GR	PtRhNi	SnO_2@PtRhNi	$PtRhNiSnO_2$ GR
Onset potential vs. RHE [V]	0.56	0.33	0.27	0.22	0.42	0.34	0.26

Furthermore, besides the chemical composition of the tested catalysts, the morphology of the nanoframes also plays a crucial role in the ethanol oxidation reaction. First, the rhombic dodecahedral shape provides 14 corners and 24 edges with low-coordinated atoms which are catalytically more active than face atoms [142]. Second, removing of the non-functional interior, results in a hollow structure with 3-D accessibility for adsorption of ethanol molecules [17]. Third, the nanoframes based catalysts generally have a higher surface-area-to-volume ratio than solid nanoparticles, which provide the improved efficiency of utilizing precious metals like Pt and Rh.

The EOR catalytic performance and catalyst stability of all tested nanocatalysts was further examined by potentiostatic chronoamperometry experiments at a potential of 0.65 V vs. RHE (Figure 78). In all curves, a sharp current decay at short times is observed which is

typical, later the curves persist a stationary value. Moreover, it can be seen that after 1.5 h of EOR the highest current densities per mg of Pt have $PtRhNiSnO_2$ GR catalysts. Analogously like in the EOR measurement (Figure 75) the catalysts with rhodium have a better performance than their counterparts without rhodium. Interestingly, the largest decay of current density values exhibits the $PtNiSnO_2$ GR catalysts, its catalytic performance drops to the level of SnO_2@Pt_3Ni and PtRhNi catalysts. This can be attributed to the degradation of the SnO_2 layer.

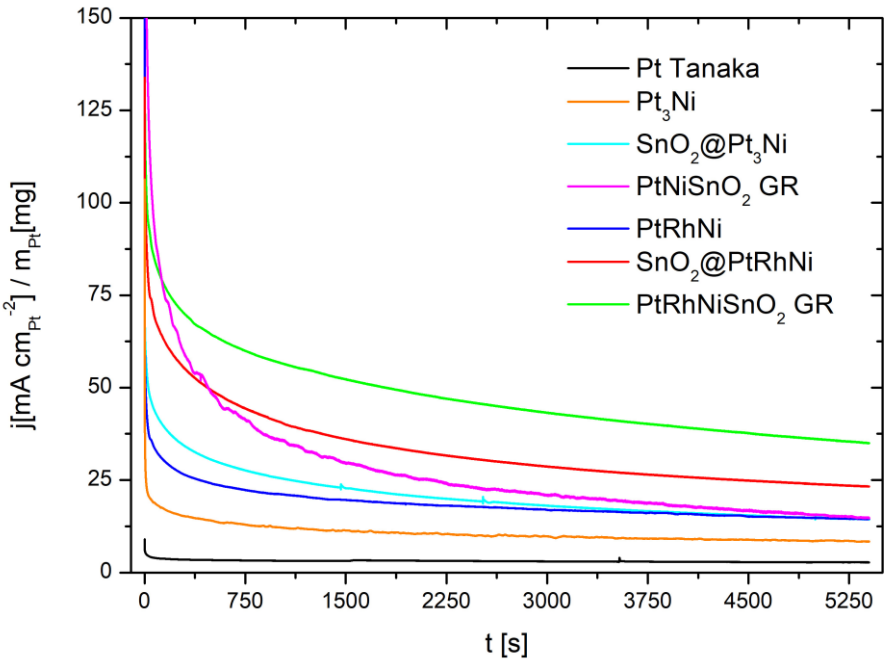

Figure 78. Chronoamperometry curves for all tested catalysts recorded at a potential of 0.65 V vs. RHE for 1.5 h (5400 s).

Chapter 4: Summary and conclusions

In the present study, two types of nanoframes-based nanocatalysts for ethanol oxidation reaction were obtained. The first were Pt_3Ni or PtRhNi nanoframes decorated with small SnO_2 nanoparticles and second were PtNi or PtRhNi nanoframes covered during galvanic replacement reaction by a thin, incomplete layer of SnO_2. Both types of nanoframes-based catalysts were obtained from starting solid, phase segregated $PtNi_3$ and PtRhNi rhombic dodecahedral nanoparticles, synthesized according to the protocol proposed by the Stamenkovic group [17]. Originally, they reported a synthesis of the solid $PtNi_3$ rhombic dodecahedral nanoparticles, however in this study this synthesis was expanded to obtain PtRhNi nanopolyhedra. Moreover, by quenching the reaction at various stages and observing the obtained intermediate products by STEM and EDS methods, it was possible tracking the synthesis mechanisms of PtRhNi nanopolyhedra. It turned out, that initially, small polyhedral PtRhNi seeds were formed, which later grew into phase-segregated PtRhNi rhombic dodecahedrons. During the growth, two processes took place: i) deposition of the reduced Pt, Rh and Ni atoms onto the seeds, which cause their size increase; ii) diffusion of the Pt and Rh atoms from the core to the edges. These observations are consistent with the study of bimetallic PtNi phase-segregated nanoparticles growth by other groups [118,119,178]. However, in this study, except platinum and nickel, rhodium is present. Due to the lack of literature reports about phase segregation during the growth of rhombic dodecahedral PtRhNi nanoparticles enclosed by {110} planes, herein DFT calculations were performed. It turned out, that similarly like in the case of PtNi systems, the Pt and Rh atoms diffuse out from the core of growing crystals to the edges to minimize the total energy caused by lattice strain. This is despite that both, platinum and rhodium have a higher surface energy than nickel, however the exposure of these elements is still more favorable energetically than if they were in the center of the nanoparticle. These results, both from STEM EDS experiments and DFT calculations confirm the first thesis of this dissertation, that indeed the phase segregation of platinum and rhodium at the edges of the solid $PtNi_3$ and PtRhNi rhombic dodecahedral nanoparticles occurs due to the diffusion of these elements. The control experiments performed on PtNi nanoparticles show that by manipulating the synthesis parameters, such as metal precursors addition temperature, reaction atmosphere, heating rate or method of adding the metal precursors, affects the growth kinetic of the nanocrystals. In consequence, it is possible to obtain nanoparticles with different morphology and chemical composition. For example, increasing the heating rate causes obtaining of overgrown nanoparticles due to the

fact that atoms are faster deposited on the growing nanoparticles than could be diffused from the deposition site to the entire surface of nanoparticles ($v_{deposition} > v_{diffusion}$). This leads to accumulation of atoms on the specific sites of the nanoparticles and their overgrowth. Analogously, changing the addition ratio of metal precursors also affects on $v_{deposition}$ and $v_{diffusion}$ and allows to obtain shape controlled dendritic nanoparticles or spherical core-shell nanoparticles. Even changing the atmosphere from inert to air, causes the formation of large pours nanoparticles instead rhombic dodecahedrons. Based on the results from the above experiments it can be concluded that the second thesis is confirmed, and indeed it is possible to synthesize PtNi and PtRhNi nanoparticles with different morphologies by manipulating synthesis parameters affecting the kinetics of the synthesis reaction. In summary, based on all the above results, it can be concluded that phase-segregated $PtNi_3$ and PtRhNi rhombic dodecahedral nanoparticles are thermodynamically favorable products of synthesis, however the synthesis itself is very sensitive on changing its kinetics, which results in obtaining different products.

The next step in obtaining the nanoframes-based catalysts decorated with SnO_2 nanoparticles was etching the Ni-core from the solid $PtNi_3$ and PtRhNi nanoparticles to obtain Pt_3Ni and PtRhNi nanoframes. The etching procedure of the solid nanoparticles to nanoframes was changed from oxidative etching, which was originally applied by Stamenkovic group [17], to the acidic etching, which is a widely used method [118,131,179]. Using this method it was possible to obtain hollow Pt_3Ni and PtRhNi nanoframes. Based on the literature research, it was found out that the etching process depends on the cohesive energy of the etched element [134,142]. Due to the fact that the cohesive energy depends on surface, from which the elements are removed, as well as on the types of the neighboring atoms, DFT simulations were performed to calculate the cohesive energy for: i) a Ni atom removed from the (110) surface of the Ni-cell, which simulates the Ni facets; ii) a Ni atom removed from the (110) surface of the PtRhNi cell, which simulates the PtRhNi edges; iii) a Pt atom removed from the (110) surface of the PtRhNi cell; iv) a Rh atom removed from the (110) surface of the PtRhNi cell. The calculated energies were increasing in the following order: Ni from (110) Ni surface < Ni from (110) PtRhNi surface < Rh from (110) PtRhNi surface < Pt from (110) PtRhNi surface. This results indicate that the easiest to remove are Ni atoms from Ni facets, which is consistent with the experimental results. Indeed, the Ni atoms from the Ni core of the $PtNi_3$ and the PtRhNi solid nanoparticles are removed, while the PtNi and the PtRhNi edges remain stable. However, on the STEM images it can be seen that locally the edges are amorphous, which could suggest that some nickel, or

even rhodium and platinum atoms are also etched away. Generally, the obtained results confirm the third thesis that etching of the solid nanopolyhedra to nanoframes can be described thermodynamically and it is dependent on the cohesive energy.

After etching the solid nanoparticles to nanoframes, small (~ 3 nm) SnO_2 NPs were synthesized and deposited on the obtained nanoframes. It is worth noting, that while the procedure of the synthesis of the solid nanoparticles and etching them to the nanoframes was known before, the idea of decorating the nanoframes with small SnO_2 nanoparticles is new and applied for the first time. The connection between the nanoframes and SnO_2 NPs is possible due to the zeta potential theory [96,97], according to which, the nanoparticles with opposite zeta potentials could forms heteroaggregates. Indeed, at pH 4.5, the Pt_3Ni and PtRhNi nanoframes have positive potential values, while SnO_2 NPs have negative potential value, therefore they combine, which is confirmed by HR STEM images and EDS maps. Also, it can be concluded that the nanoframes are covered with SnO_2 NPs due to the decreasing ECSA value in the sample containing SnO_2 NPs compared to nanoframes without SnO_2 NPs. This results confirm the fourth thesis, that it is possible to decorate the nanoframes with small SnO_2 nanoparticles in a controlled manner based on their opposite zeta potentials.

Another way to obtain nanoframes-based nanocatalysts is to obtain nanoframes from solid nanoparticles and to cover them with a thin and incomplete Sn-layer by galvanic replacement reaction. The GRR occurs between nickel atoms from the core of the nanoparticles and Sn^{4+} ions originating from $SnCl_4$, the platinum and rhodium do not participate in the reaction. This allows to obtain PtNiSn or PtRhNiSn nanoframes, which could be oxidized into the $PtNiSnO_2$ and $PtRhNiSnO_2$ nanoframes during annealing. By sampling the intermediates during GRR, it was possible to observe two mechanisms of galvanic replacement. In the first, nickel oxidation and tin deposition occur simultaneously, in the second, tin deposition occurs after the nickel oxidation. This mechanism results from combining the galvanic replacement reaction with co-reduction of tin by ethylene glycol and from oxidative etching due to the presence of Cl^-/O_2 pair. When co-reduction of tin by EG dominates, then simultaneously nickel oxidation and tin deposition takes place, on the other hand, when oxidative etching dominates, first the nickel oxidation takes place and it is followed by tin deposition. The control experiments reveal that replacing the ethylene glycol with water results in a slower reaction, which suggest that indeed EG plays a crucial role in galvanic replacement between Ni and Sn. Also, decreasing the Sn^{4+} concentration slows down the reaction. The above results confirm the fifth thesis, that the galvanic

replacement reaction strongly depends on the concentration of the reagents as well as on the type of the used solvent.

Despite that the nanoframes are very promising nanocatalysts, in literature there are only a few studies of using nanoframes with different shapes as EOR catalysts [31,32,180]. However most of the research groups focus on the use of nanoframes as catalysts for oxygen reduction reaction [124,131,181], formic acid oxidation reaction [182–184] or methanol oxidation reaction [31,127,185,186]. Therefore, all of the obtained nanoframes-based catalysts were electrochemically tested towards EOR, showing better performance than commercially used Pt Tanaka. However, there are differences in onset potentials and current densities between the nanoframes catalysts. Generally, the lower onset potential have catalysts based on PtNi nanoframes in comparison to their counterparts with rhodium, while the higher current densities per milligram of Pt have the PtRhNi nanoframes-based catalysts. Considering each nanocatalysts group separately (PtNi-based and PtRhNi-based) it can be seen that the lowest onset potential and the highest values of current densities have the catalysts obtained by galvanic replacement reaction. It is worth noticing that the $PtRhNiSnO_2$ GR catalysts have the highest value of the current density and have the second lowest onset potential among all tested catalysts, making them good for potential application as EOR catalysts.

All of the above discussion can be summarized in the following conclusions:

- During growth of solid $PtNi_3$ and PtRhNi rhombic dodecahedral nanoparticles two processes occur: diffusion of Pt and Rh from the core of the growing nanoparticles to the edges and Pt, Rh, Ni atoms deposition on the nanoparticles.
- Phase segregation of solid nanoparticles is caused by the diffusion of Pt and Rh, while the size increase is caused by the deposition of Pt, Rh and Ni atoms.
- The obtained solid nanoparticles are thermodynamically favorable products, however by manipulating the kinetics, it is possible to obtain nanoparticles with different morphology.
- It is possible to obtain hollow Pt_3Ni and PtRhNi nanoframes from solid $PtNi_3$ and PtRhNi nanoparticles due to Ni etching from the core of nanoparticles.
- Both, STEM observations and DFT calculations, confirm that Ni atoms are more stable during etching, while when they are alloyed with Pt and Rh atoms.
- During the thermal annealing of the obtained nanoframes, recrystallization and diffusion of the platinum to the surface occur, which results in obtaining Pt-skin Pt_3Ni and PtRhNi nanoframes.

- It is possible to obtain SnO_2@Pt_3Ni and SnO_2@PtRhNi heteroaggregates in a controlled manner due to opposite zeta potentials of SnO_2 NPs and nanoframes.
- By applying the galvanic replacement reaction between solid $PtNi_3$ or PtRhNi rhombic dodecahedral nanoparticles and $SnCl_4$ it is possible to obtain hollow PtNiSn or PtRhNiSn nanoframes in one step.
- By thermal annealing of PtNiSn and PtRhNiSn nanoframes it is possible to oxidize the Sn-layer to SnO_2-layer.
- The obtained nanoframes-based catalysts have better catalytic performance compared to commercially used Pt Tanaka catalysts.
- The highest current densities per milligram of Pt have PtRhNiSnO_2 GR catalysts, and they also exhibit the second lowest onset potential, which make them good potential catalysts towards EOR.

References

[1] M. Winter, R.J. Brodd, Chem. Rev. 104 (2004) 4245–4270.

[2] J.J. Hwang, Renew. Sustain. Energy Rev. 16 (2012) 3803–3815.

[3] M.Z.F. Kamaruddin, S.K. Kamarudin, W.R.W. Daud, M.S. Masdar, Renew. Sustain. Energy Rev. 24 (2013) 557–565.

[4] J.W. Gosselink, Int. J. Hydrogen Energy 27 (2002) 1125–1129.

[5] R. Ströbel, M. Oszcipok, M. Fasil, B. Rohland, L. Jörissen, J. Garche, J. Power Sources 105 (2002) 208–215.

[6] P. Majidi, R.M. Altarawneh, N.D.W. Ryan, P.G. Pickup, Electrochim. Acta 199 (2016) 210–217.

[7] N. Sarkar, S.K. Ghosh, S. Bannerjee, K. Aikat, Renew. Energy 37 (2012) 19–27.

[8] T.S. Zhao, Y.S. Li, S.Y. Shen, Front. Energy Power Eng. China 4 (2010) 443–458.

[9] P. Barbaro, C. Bianchini, eds., Catalysis for Sustainable Energy Production, Wiley-VCH Verlag GmbH & Co. KGaA, Weinheim, Germany, 2009.

[10] L. An, T.S. Zhao, Y.S. Li, Renew. Sustain. Energy Rev. 50 (2015) 1462–1468.

[11] S.P.S. Badwal, S. Giddey, A. Kulkarni, J. Goel, S. Basu, Appl. Energy 145 (2015) 80–103.

[12] X. Teng, Materials and Processes for Energy: Communicating Current Research and Technological Developments, Formatex Research Center, 2013.

[13] F. Colmati, G. Tremiliosi-Filho, E.R. Gonzalez, A. Berná, E. Herrero, J.M. Feliu, Phys. Chem. Chem. Phys. 11 (2009) 9114.

[14] E. Antolini, J. Power Sources 170 (2007) 1–12.

[15] A. Kowal, M. Li, M. Shao, K. Sasaki, M.B. Vukmirovic, J. Zhang, N.S. Marinkovic, P. Liu, A.I. Frenkel, R.R. Adzic, Nat. Mater. 8 (2009) 325–330.

[16] M. Li, A. Kowal, K. Sasaki, N. Marinkovic, D. Su, E. Korach, P. Liu, R.R. Adzic, Electrochim. Acta 55 (2010) 4331–4338.

[17] C. Chen, Y. Kang, Z. Huo, Z. Zhu, W. Huang, H.L. Xin, J.D. Snyder, D. Li, J.A. Herron, M. Mavrikakis, M. Chi, K.L. More, Y. Li, N.M. Markovic, G.A. Somorjai, P. Yang, V.R. Stamenkovic, Science 343 (2014) 1339–43.

[18] G.A. Camara, T. Iwasita, J. Electroanal. Chem. 578 (2005) 315–321.

[19] W. Du, G. Yang, E. Wong, N.A. Deskins, A.I. Frenkel, D. Su, X. Teng, J. Am. Chem. Soc. 136 (2014) 10862–10865.

[20] R. Rizo, R.M. Arán-Ais, E. Padgett, D.A. Muller, M.J. Lázaro, J. Solla-Gullón, J.M.

Feliu, E. Pastor, H.D. Abruña, J. Am. Chem. Soc. 140 (2018) 3791–3797.

[21] V.M. Schmidt, R. Ianniello, E. Pastor, S. González, J. Phys. Chem. 100 (2002) 17901–17908.

[22] N. Fujiwara, K.A. Friedrich, U. Stimming, J. Electroanal. Chem. 472 (1999) 120–125.

[23] A. Kowal, S.L. Gojković, K.-S. Lee, P. Olszewski, Y.-E. Sung, Electrochem. Commun. 11 (2009) 724–727.

[24] M. Batzill, U. Diebold, Prog. Surf. Sci. 79 (2005) 47–154.

[25] P.J.D. Lindan, Chem. Phys. Lett. 328 (2000) 325–329.

[26] A. Więckowski, Interfacial Electrochemistry : Theory, Experiment, and Applications, Marcel Dekker, 1999.

[27] A. Bach Delpeuch, F. Maillard, M. Chatenet, P. Soudant, C. Cremers, Appl. Catal. B Environ. 181 (2016) 672–680.

[28] V. Comignani, J.M. Sieben, M.E. Brigante, M.M.E. Duarte, J. Power Sources 278 (2015) 119–127.

[29] N. Erini, V. Beermann, M. Gocyla, M. Gliech, M. Heggen, R.E. Dunin-Borkowski, P. Strasser, Angew. Chemie Int. Ed. 56 (2017) 6533–6538.

[30] C. Busó-Rogero, S. Brimaud, J. Solla-Gullon, F.J. Vidal-Iglesias, E. Herrero, R.J. Behm, J.M. Feliu, J. Electroanal. Chem. 763 (2016) 116–124.

[31] J. Ding, L. Bu, S. Guo, Z. Zhao, E. Zhu, Y. Huang, X. Huang, Nano Lett. 16 (2016) 2762–2767.

[32] Y. Wang, Y. Chen, C. Nan, L. Li, D. Wang, Q. Peng, Y. Li, Nano Res. 8 (2015) 140–155.

[33] J. Park, Y.J. Sa, H. Baik, T. Kwon, S.H. Joo, K. Lee, ACS Nano 11 (2017) 5500–5509.

[34] S. Xie, N. Lu, Z. Xie, J. Wang, M.J. Kim, Y. Xia, Angew. Chemie Int. Ed. 51 (2012) 10266–10270.

[35] L.Y. Chang, A.S. Barnard, L.C. Gontard, R.E. Dunin-Borkowski, Nano Lett. 10 (2010) 3073–3076.

[36] J. Gu, Y.-W. Zhang, F. (Feng) Tao, Chem. Soc. Rev. 41 (2012) 8050.

[37] Z. Peng, H. Yang, Nano Today 4 (2009) 143–164.

[38] J. Polte, CrystEngComm 17 (2015) 6809–6830.

[39] N.T.K. Thanh, N. Maclean, S. Mahiddine, Chem. Rev. 114 (2014) 7610–7630.

[40] Y. Xiong, X. Lu, Metallic Nanostructures : From Controlled Synthesis to Applications, Springer, 2015.

[41] G. Cao, Y. Wang, Nanostructures and Nanomaterials, WORLD SCIENTIFIC, 2011.

[42] T. Wen, L.N. Brush, K.M. Krishnan, J. Colloid Interface Sci. 419 (2014) 79–85.

[43] R. Xu, D. Wang, J. Zhang, Y. Li, Chem. – An Asian J. 1 (2006) 888–893.

[44] S. Mostafa, F. Behafarid, J.R. Croy, L.K. Ono, L. Li, J.C. Yang, A.I. Frenkel, B.R. Cuenya, J. Am. Chem. Soc. 132 (2010) 15714–15719.

[45] T.S. Ahmadi, Z.L. Wang, T.C. Green, A. Henglein, M.A. El-Sayed, Science 272 (1996) 1924–6.

[46] J.M. Petroski, Z.L. Wang, T.C. Green, M.A. El-Sayed, J. Phys. Chem. B 102 (1998) 3316–3320.

[47] T. Teranishi, R. Kurita, M. Miyake, J. Inorg. Organomet. Polym. 10 (2000) 145–156.

[48] Y. Xia, X. Xia, H.-C. Peng, J. Am. Chem. Soc. 137 (2015) 7947–7966.

[49] S. Xie, X.Y. Liu, Y. Xia, Nano Res. 8 (2015) 82–96.

[50] A.P. LaGrow, K.R. Knudsen, N.M. AlYami, D.H. Anjum, O.M. Bakr, Chem. Mater. 27 (2015) 4134–4141.

[51] P. Wang, S. Yin, Y. Wen, Z. Tian, N. Wang, J. Key, S. Wang, P.K. Shen, ACS Appl. Mater. Interfaces 9 (2017) 9584–9591.

[52] F. Saleem, B. Ni, Y. Yong, L. Gu, X. Wang, Small 12 (2016) 5261–5268.

[53] R. Ferrando, J. Jellinek, R.L. Johnston, Chem. Rev. 108 (2008) 845–910.

[54] R. Ghosh Chaudhuri, S. Paria, Chem. Rev. 112 (2012) 2373–2433.

[55] X. Wang, S.-I. Choi, L.T. Roling, M. Luo, C. Ma, L. Zhang, M. Chi, J. Liu, Z. Xie, J.A. Herron, M. Mavrikakis, Y. Xia, Nat. Commun. 6 (2015) 7594.

[56] N. Lu, J. Wang, S. Xie, Y. Xia, M.J. Kim, Chem. Commun. 49 (2013) 11806.

[57] K.D. Gilroy, A. Ruditskiy, H.-C. Peng, D. Qin, Y. Xia, Chem. Rev. 116 (2016) 10414–10472.

[58] V. V. Pryadchenko, V. V. Srabionyan, E.B. Mikheykina, L.A. Avakyan, V.Y. Murzin, Y. V. Zubavichus, I. Zizak, V.E. Guterman, L.A. Bugaev, J. Phys. Chem. C 119 (2015) 3217–3227.

[59] C. Wang, H. Yin, R. Chan, S. Peng, S. Dai, S. Sun, Chem. Mater. 21 (2009) 433–435.

[60] B. Wiley, Y. Sun, B. Mayers, Y. Xia, Chem. - A Eur. J. 11 (2005) 454–463.

[61] Y. Xia, K.D. Gilroy, H.-C. Peng, X. Xia, Angew. Chemie Int. Ed. 56 (2017) 60–95.

[62] S.E. Habas, H. Lee, V. Radmilovic, G.A. Somorjai, P. Yang, Nat. Mater. 6 (2007) 692–697.

[63] B.T. Sneed, C.N. Brodsky, C.-H. Kuo, L.K. Lamontagne, Y. Jiang, Y. Wang, F. (Feng) Tao, W. Huang, C.-K. Tsung, J. Am. Chem. Soc. 135 (2013) 14691–14700.

[64] A. Popa, A.C.S. Samia, Chem. Commun. 50 (2014) 7295.

[65] P. Shi, M. Li, J. Ren, X. Qu, Adv. Funct. Mater. 23 (2013) 5412–5419.

[66] M.A. Mahmoud, M.A. El-Sayed, Langmuir 28 (2012) 4051–4059.

[67] F. Nosheen, Z. Zhang, J. Zhuang, X. Wang, Nanoscale 5 (2013) 3660.

[68] H.-J. Jang, S. Hong, S. Park, J. Mater. Chem. 22 (2012) 19792.

[69] M.M. Shahjamali, M. Bosman, S. Cao, X. Huang, X. Cao, H. Zhang, S.S. Pramana, C. Xue, Small 9 (2013) 2880–2886.

[70] M. McEachran, D. Keogh, B. Pietrobon, N. Cathcart, I. Gourevich, N. Coombs, V. Kitaev, J. Am. Chem. Soc. 133 (2011) 8066–8069.

[71] X. Lu, L. Au, J. McLellan, Z.Y. Li, M. Marquez, Y. Xia, Nano Lett. 7 (2007) 1764–1769.

[72] L. Polavarapu, D. Zanaga, T. Altantzis, S. Rodal-Cedeira, I. Pastoriza-Santos, J. Pérez-Juste, S. Bals, L.M. Liz-Marzán, J. Am. Chem. Soc. 138 (2016) 11453–11456.

[73] M. Hajfathalian, K.D. Gilroy, S.D. Golze, A. Yaghoubzade, E. Menumerov, R.A. Hughes, S. Neretina, ACS Nano 10 (2016) 6354–6362.

[74] X. Xia, Y. Wang, A. Ruditskiy, Y. Xia, Adv. Mater. 25 (2013) 6313–6333.

[75] X. Teng, Q. Wang, P. Liu, W. Han, A.I. Frenkel, W. Wen, N. Marinkovic, J.C. Hanson, J.A. Rodriguez, J. Am. Chem. Soc. 130 (2008) 1093–1101.

[76] H.M. Chen, R.-S. Liu, M.-Y. Lo, S.-C. Chang, L.-D. Tsai, Y.-M. Peng, J.-F. Lee, J. Phys. Chem. C 112 (2008) 7522–7526.

[77] N.R. Sieb, N. Wu, E. Majidi, R. Kukreja, N.R. Branda, B.D. Gates, ACS Nano 3 (2009) 1365–1372.

[78] L. Au, Y. Chen, F. Zhou, P.H.C. Camargo, B. Lim, Z.-Y. Li, D.S. Ginger, Y. Xia, Nano Res. 1 (2008) 441–449.

[79] X. Hong, D. Wang, S. Cai, H. Rong, Y. Li, J. Am. Chem. Soc. 134 (2012) 18165–18168.

[80] M. Tsuji, T. Kidera, A. Yajima, M. Hamasaki, M. Hattori, T. Tsuji, H. Kawazumi, CrystEngComm 16 (2014) 2684.

[81] H.J. Fan, U. Gösele, M. Zacharias, Small 3 (2007) 1660–1671.

[82] Y. Yin, R.M. Rioux, C.K. Erdonmez, S. Hughes, G.A. Somorjai, A.P. Alivisatos, Science 304 (2004) 711–4.

[83] E. Gonzalez, J. Arbiol, V.F. Puntes, Science (80-.). 334 (2011) 1377–1380.

[84] L. Han, H. Liu, P. Cui, Z. Peng, S. Zhang, J. Yang, Sci. Rep. 4 (2015) 6414.

[85] J.-J. Zhu, J.-M. Zhu, X.-H. Liao, J.-L. Fang, M.-G. Zhou, H.-Y. Chen, Mater. Lett. 53 (2002) 12–19.

[86] R.F. Egerton, Physical Principles of Electron Microscopy : An Introduction to TEM, SEM, and AEM, Springer Science+Business Media, Inc, 2005.

[87] D.B. Williams, C.B. Carter, in: Transm. Electron Microsc., Springer US, Boston, MA, 2009, pp. 3–22.

[88] F. Hosokawa, H. Sawada, Y. Kondo, K. Takayanagi, K. Suenaga, Microscopy 62 (2013) 23–41.

[89] Https://en.wikipedia.org/wiki/Transmission_electron_microscopy#/media/File:Scheme_TEM_en.svg, (2019).

[90] Z.W. Wang, Z.Y. Li, S.J. Park, A. Abdela, D. Tang, R.E. Palmer, Phys. Rev. B 84 (2011) 073408.

[91] J.W. Edington, Practical Electron Microscopy in Materials Science, N.V. Philips, 1976.

[92] J.J. Friel, R. Terborg, S. Langner, T. Salge, M. Rohde, J. Berlin, X-Ray and Image Analysis in Electron Microscopy, Bruker Nano GmbH Pro Business Digital Printing et Copyservice GmbH (Berlin), 2016.

[93] Y. Waseda, E. Matsubara, K. Shinoda, X-Ray Diffraction Crystallography, Springer Berlin Heidelberg, Berlin, Heidelberg, 2011.

[94] S. Baskaran, Https://Www.Researchgate.Net/Figure/Braggs-Law-A-Two-Dimensional-Crystal-Lattice-and-a-Set-of-Imaginary-Planes-Is_fig10_47418334 (2010).

[95] M. Birkholz, Thin Film Analysis by X-Ray Scattering, Wiley-VCH Verlag GmbH & Co. KGaA, Weinheim, FRG, 2005.

[96] M. Sadowska, Z. Adamczyk, M. Oćwieja, M. Nattich-Rak, Colloids Surfaces A Physicochem. Eng. Asp. 499 (2016) 1–9.

[97] E. Drzymała, G. Gruzeł, A. Pajor-Świerzy, J. Depciuch, R. Socha, A. Kowal, P. Warszyński, M. Parlinska-Wojtan, J. Nanoparticle Res. 20 (2018) 144.

[98] B.J. Kirby, E.F. Hasselbrink, Electrophoresis 25 (2004) 187–202.

[99] R.J. Hunter, Zeta Potential in Colloid Science: Principles and Applications, Elsevier Science, 1981.

[100] Https://En.Wikipedia.Org/Wiki/Zeta_potential#/Media/File:Diagram_of_zeta_potential_and_slipping_planeV2.Svg (2012).

[101] S. Bhattacharjee, J. Control. Release 235 (2016) 337–351.

[102] A.J. Bard, L.R. Faulkner, Electrochemical Methods : Fundamentals and Applications, Wiley, 2001.

[103] J.F. Rusling, S.L. Suib, Adv. Mater. 6 (1994) 922–930.

[104] N. Elgrishi, K.J. Rountree, B.D. McCarthy, E.S. Rountree, T.T. Eisenhart, J.L. Dempsey, J. Chem. Educ. 95 (2018) 197–206.

[105] Timothy M. Paschkewitz, Https://En.Wikipedia.Org/Wiki/Cyclic_voltammetry#/Media/File:Cyclicvoltammetrywaveform.Jpg (2006).

[106] L. Bu, Q. Shao, B. E, J. Guo, J. Yao, X. Huang, J. Am. Chem. Soc. 139 (2017) 9576–9582.

[107] M. Wang, Y. He, R. Li, Z. Ma, Z. Zhang, X. Wang, Electrochim. Acta 178 (2015) 259–269.

[108] E. Kryachko, E. Ludeña, Phys. Rep. 544 (2014) 123–239.

[109] A.J. Cohen, P. Mori-Sánchez, W. Yang, Chem. Rev. 112 (2012) 289–320.

[110] R.O. Jones, Rev. Mod. Phys. 87 (2015) 897–923.

[111] J.P. Perdew, K. Burke, M. Ernzerhof, Phys. Rev. Lett. 77 (1996) 3865–3868.

[112] G. Kresse, J. Furthmüller, Comput. Mater. Sci. 6 (1996) 15–50.

[113] H.J. Monkhorst, J.D. Pack, Phys. Rev. B 13 (1976) 5188–5192.

[114] K. Momma, F. Izumi, J. Appl. Crystallogr. 44 (2011) 1272–1276.

[115] C. de Mello Donegá, P. Liljeroth, D. Vanmaekelbergh, Small 1 (2005) 1152–1162.

[116] Z. Xu, C. Shen, Y. Hou, H. Gao, S. Sun, Chem. Mater. 21 (2009) 1778–1780.

[117] J.O. Bockris, B.E. Conway, Modern Aspects of Electrochemistry : No. 12, Springer US, 1977.

[118] Z. Niu, N. Becknell, Y. Yu, D. Kim, C. Chen, N. Kornienko, G.A. Somorjai, P. Yang, Nat. Mater. 15 (2016) 1188–1194.

[119] A. Oh, H. Baik, D.S. Choi, J.Y. Cheon, B. Kim, H. Kim, S.J. Kwon, S.H. Joo, Y. Jung, K. Lee, ACS Nano 9 (2015) 2856–2867.

[120] Y. Ma, P.B. Balbuena, Surf. Sci. 602 (2008) 107–113.

[121] C. Cui, M. Ahmadi, F. Behafarid, L. Gan, M. Neumann, M. Heggen, B.R. Cuenya, P. Strasser, Faraday Discuss. 162 (2013) 91.

[122] W.M. Haynes, CRC Handbook of Chemistry and Physics : A Ready-Reference Book of Chemical and Physical Data, CRC Press, 2011.

[123] B. Corain, G. Schmid, N. Toshima, Metal Nanoclusters in Catalysis and Materials Science : The Issue of Size Control, Elsevier, 2008.

[124] N. Becknell, Y. Son, D. Kim, D. Li, Y. Yu, Z. Niu, T. Lei, B.T. Sneed, K.L. More, N.M. Markovic, V.R. Stamenkovic, P. Yang, J. Am. Chem. Soc. 139 (2017) 11678–

11681.
[125] J. Chen, B. Lim, E.P. Lee, Y. Xia, Nano Today 4 (2009) 81–95.
[126] B. Ni, X. Wang, Adv. Sci. 2 (2015) 1500085.
[127] S. Luo, P.K. Shen, ACS Nano 11 (2017) 11946–11953.
[128] H. Ye, Q. Wang, M. Catalano, N. Lu, J. Vermeylen, M.J. Kim, Y. Liu, Y. Sun, X. Xia, Nano Lett. 16 (2016) 2812–2817.
[129] G.S. Métraux, Y.C. Cao, R. Jin, C.A. Mirkin, Nano Lett. 6 (2003) 519–522.
[130] M. Gong, G. Fu, Y. Chen, Y. Tang, T. Lu, ACS Appl. Mater. Interfaces 6 (2014) 7301–8.
[131] J. Park, M. Kanti Kabiraz, H. Kwon, S. Park, H. Baik, S.-I. Choi, K. Lee, ACS Nano 11 (2017) 10844–10851.
[132] Q. Chen, J. Zhang, Y. Jia, Z. Jiang, Z. Xie, L. Zheng, Nanoscale 6 (2014) 7019–7024.
[133] D. Li, C. Wang, D. Tripkovic, S. Sun, N.M. Markovic, V.R. Stamenkovic, ACS Catal. 2 (2012) 1358–1362.
[134] Y. Wu, D. Wang, Z. Niu, P. Chen, G. Zhou, Y. Li, Angew. Chemie Int. Ed. 51 (2012) 12524–12528.
[135] D. Brown, P. Quinn, D. Woodruff, T. Noakes, P. Bailey, Surf. Sci. 497 (2002) 1–12.
[136] S. Dai, Y. You, S. Zhang, W. Cai, M. Xu, L. Xie, R. Wu, G.W. Graham, X. Pan, Nat. Commun. 8 (2017) 204.
[137] C. Wang, M. Chi, D. Li, D. Strmcnik, D. van der Vliet, G. Wang, V. Komanicky, K.-C. Chang, A.P. Paulikas, D. Tripkovic, J. Pearson, K.L. More, N.M. Markovic, V.R. Stamenkovic, J. Am. Chem. Soc. 133 (2011) 14396–14403.
[138] C. Cui, L. Gan, M. Heggen, S. Rudi, P. Strasser, Nat. Mater. 12 (2013) 765–771.
[139] E. Zhu, Y. Li, C.-Y. Chiu, X. Huang, M. Li, Z. Zhao, Y. Liu, X. Duan, Y. Huang, Nano Res. 9 (2016) 149–157.
[140] C.D. Taylor, M. Neurock, J.R. Scully, J. Electrochem. Soc. 155 (2008) C407.
[141] C. Kittel, Introduction to Solid State Physics, Wiley, 2005.
[142] Y. Wu, D. Wang, G. Zhou, R. Yu, C. Chen, Y. Li, J. Am. Chem. Soc. 136 (2014) 11594–11597.
[143] H.-P. Zhou, H.-S. Wu, J. Shen, A.-X. Yin, L.-D. Sun, C.-H. Yan, J. Am. Chem. Soc. 132 (2010) 4998–4999.
[144] S.A.B. Ab. Aziz, S.H. Amirnordin, H.A. Rahman, H.Z. Abdullah, H. Taib, Adv. Mater. Res. 795 (2013) 334–337.
[145] J. Liu, C. Dai, Y. Hu, Environ. Res. 161 (2018) 49–60.

[146] H. Sefardjella, B. Boudjema, A. Kabir, G. Schmerber, J. Phys. Chem. Solids 74 (2013) 1686–1689.

[147] H. Sefardjella, B. Boudjema, A. Kabir, G. Schmerber, Curr. Appl. Phys. 13 (2013) 1971–1974.

[148] N. Abdullah, N.M. Ismail, D.M. Nuruzzaman, IOP Conf. Ser. Mater. Sci. Eng. 319 (2018) 012022.

[149] L. Zhang, L.T. Roling, X. Wang, M. Vara, M. Chi, J. Liu, S.-I. Choi, J. Park, J.A. Herron, Z. Xie, M. Mavrikakis, Y. Xia, Science (80-.). 349 (2015) 412–416.

[150] L.M. Moreau, C.A. Schurman, S. Kewalramani, M.M. Shahjamali, C.A. Mirkin, M.J. Bedzyk, J. Am. Chem. Soc. 139 (2017) 12291–12298.

[151] S. Tsuzuki, ChemPhysChem 13 (2012) 1664–1670.

[152] M. Yang, W. Wang, K.D. Gilroy, Y. Xia, Nano Lett. 17 (2017) 5682–5687.

[153] E. Drzymała, G. Gruzeł, J. Depciuch, A. Budziak, A. Kowal, M. Parlinska-Wojtan, J. Phys. Chem. Solids 107 (2017) 100–107.

[154] S. Mourdikoudis, L.M. Liz-Marzán, Chem. Mater. 25 (2013) 1465–1476.

[155] M.H. Oh, T. Yu, S.-H. Yu, B. Lim, K.-T. Ko, M.-G. Willinger, D.-H. Seo, B.H. Kim, M.G. Cho, J.-H. Park, K. Kang, Y.-E. Sung, N. Pinna, T. Hyeon, G.A. Somorjai, P. Yang, V.R. Stamenkovic, Science (80-.). 340 (2013) 964–968.

[156] X. Yang, L.T. Roling, M. Vara, A.O. Elnabawy, M. Zhao, Z.D. Hood, S. Bao, M. Mavrikakis, Y. Xia, Nano Lett. 16 (2016) 6644–6649.

[157] J.A. Bordley, M.A. El-Sayed, J. Phys. Chem. C 120 (2016) 14643–14651.

[158] S.-C. Lin, C.-S. Hsu, S.-Y. Chiu, T.-Y. Liao, H.M. Chen, J. Am. Chem. Soc. 139 (2017) 2224–2233.

[159] D.-H. Lim, D.-H. Choi, W.-D. Lee, H.-I. Lee, Appl. Catal. B Environ. 89 (2009) 484–493.

[160] E. V. Spinacé, M. Linardi, A.O. Neto, Electrochem. Commun. 7 (2005) 365–369.

[161] H. Gharibi, S. Sadeghi, F. Golmohammadi, Electrochim. Acta 190 (2016) 1100–1112.

[162] M. Li, W.-P. Zhou, N.S. Marinkovic, K. Sasaki, R.R. Adzic, Electrochim. Acta 104 (2013) 454–461.

[163] A. Bach Delpeuch, T. Asset, M. Chatenet, C. Cremers, Fuel Cells 15 (2015) 352–360.

[164] M. Watanabe, S. Motoo, J. Electroanal. Chem. Interfacial Electrochem. 60 (1975) 267–273.

[165] K. An, G.A. Somorjai, Catal. Letters 145 (2015) 233–248.

[166] Y. Suchorski, S.M. Kozlov, I. Bespalov, M. Datler, D. Vogel, Z. Budinska, K.M.

Neyman, G. Rupprechter, Nat. Mater. 17 (2018) 519–522.
[167] W.-P. Zhou, W. An, D. Su, R. Palomino, P. Liu, M.G. White, R.R. Adzic, J. Phys. Chem. Lett. 3 (2012) 3286–3290.
[168] B. Hammer, J.K. Nørskov, Adv. Catal. 45 (2000) 71–129.
[169] A. Ruban, B. Hammer, P. Stoltze, H.. Skriver, J.. Nørskov, J. Mol. Catal. A Chem. 115 (1997) 421–429.
[170] T. Bligaard, J.K. Nørskov, Electrochim. Acta 52 (2007) 5512–5516.
[171] J.K. Nørskov, F. Studt, F. Abild-Pedersen, T. Bligaard, Fundamental Concepts in Heterogeneous Catalysis, John Wiley & Sons, Inc, Hoboken, NJ, USA, 2014.
[172] N. Erini, S. Rudi, V. Beermann, P. Krause, R. Yang, Y. Huang, P. Strasser, ChemElectroChem 2 (2015) 903–908.
[173] J.E. Sulaiman, S. Zhu, Z. Xing, Q. Chang, M. Shao, ACS Catal. 7 (2017) 5134–5141.
[174] G. Yang, L.M. Namin, N. Aaron Deskins, X. Teng, J. Catal. 353 (2017) 335–348.
[175] G. Yang, A.I. Frenkel, D. Su, X. Teng, ChemCatChem 8 (2016) 2876–2880.
[176] E. Higuchi, T. Takase, M. Chiku, H. Inoue, J. Power Sources 263 (2014) 280–287.
[177] M. Li, N.S. Marinkovic, K. Sasaki, Electrocatalysis 3 (2012) 376–385.
[178] A. Nagao, K. Higashimine, J.L. Cuya Huaman, T. Iwamoto, T. Matsumoto, Y. Inoue, S. Maenosono, H. Miyamura, B. Jeyadevan, Nanoscale 7 (2015) 9927–9934.
[179] S. Chen, Z. Niu, C. Xie, M. Gao, M. Lai, M. Li, P. Yang, ACS Nano 12 (2018) 8697–8705.
[180] S.-H. Han, H.-M. Liu, P. Chen, J.-X. Jiang, Y. Chen, Adv. Energy Mater. 8 (2018) 1801326.
[181] L.-M. Lyu, Y.-C. Kao, D.A. Cullen, B.T. Sneed, Y.-C. Chuang, C.-H. Kuo, Chem. Mater. 29 (2017) 5681–5692.
[182] Y. Jia, Y. Jiang, J. Zhang, L. Zhang, Q. Chen, Z. Xie, L. Zheng, J. Am. Chem. Soc. 136 (2014) 3748–3751.
[183] C. Wang, L. Zhang, H. Yang, J. Pan, J. Liu, C. Dotse, Y. Luan, R. Gao, C. Lin, J. Zhang, J.P. Kilcrease, X. Wen, S. Zou, J. Fang, Nano Lett. 17 (2017) 2204–2210.
[184] Z. Wang, H. Wang, Z. Zhang, G. Yang, T. He, Y. Yin, M. Jin, ACS Nano 11 (2017) 163–170.
[185] X. Yan, S. Yu, Y. Tang, D. Sun, L. Xu, C. Xue, Nanoscale 10 (2018) 2231–2235.
[186] Y. Xiong, Y. Ma, Z. Lin, Q. Xu, Y. Yan, H. Zhang, J. Wu, D. Yang, CrystEngComm 18 (2016) 7823–7830.

List of figures and tables